The interplanetary hydrogen: a tracer of the heliospheric interface

Frédéric E. Vincent

Thèse de Doctorat de
l'Université Pierre et Marie Curie

Spécialité : Astrophysique

Présentée par
M. Frédéric E. Vincent

Pour obtenir le grade de
Docteur de l'Université Pierre et Marie Curie

L'hydrogène interplanétaire : un traceur de l'interface héliosphérique

Soutenue le 14 octobre 2011, devant le jury composé de

M.	Vladimir	Baranov	(Examinateur)
M.	Lotfi	Ben-Jaffel	(Directeur de thèse)
M.	Walter	Harris	(Co-directeur de thèse)
M.	Jean-Pierre	Maillard	(Examinateur)
M.	Wayne	Pryor	(Rapporteur)
M^{me}	Romana	Ratkiewicz	(Rapporteur)
M.	Fred	Roesler	(Examinateur)
M.	Bruno	Sicardy	(Président du jury)

À mes parents,
à Laurène.

Titre L'hydrogène interplanétaire : un traceur de l'interface héliosphérique

Résumé L'interface héliosphérique résulte de l'interaction entre le vent solaire et le milieu interstellaire (MIS). L'hydrogène interplanétaire (HIP), une population de neutres qui remplit l'espace entre les planètes à l'intérieur de l'héliosphère, porte la signature du MIS et de l'interface héliosphérique : alors que la composante ionisée du MIS est déviée à l'héliopause, des réactions d'échange de charge ralentissent le mouvement d'ensemble des neutres qui pénètrent l'héliosphère. A l'intérieur de l'héliosphère, l'HIP subit l'influence du Soleil et diffuse les photons Lyman-alpha. Le cycle solaire 23 fournit le premier relevé temporel de la vitesse de l'HIP.

Dans une première partie, je présente une mise-à-jour de l'analyse des mesures de vitesse de l'HIP faites par les spectromètres du Hubble Space Telescope (GHRS et STIS) et compare ces résultats avec ceux de l'instrument SOHO/SWAN et deux modèles dépendant du temps. Avec ces mises-à-jour des observations HST, nous trouvons que toutes les données peuvent être ajustées aux modèles existants dans un intervalle d'une barre d'erreur, à l'exception des observations SWAN faites lors d'un minimum solaire (1997/98). Nous interprétons cet écart comme un possible effet dû à l'inclinaison du champ magnétique interstellaire local.

Dans une seconde partie, je décris le développement d'une expérience sur fusée-sonde (HYPE-INSPIRE) qui observera le profil d'émission de la raie Lyman-alpha de l'HIP avec un Spectromètre Hétérodyne Spatial (SHS), un nouveau type d'interféromètre. Ce travail instrumental a révélé une anomalie d'efficacité dans le réseau de diffraction utilisé pour l'expérience. Je conclus par une description de l'état d'avancement du projet avec un vol prévu en 2012.

Mots-clés Milieu interstellaire ; Héliosphère ; Astronomie en ultraviolet ; Instrumentation ; Interférométrie ; Réseaux de diffraction.

Laboratoire Institut d'Astrophysique de Paris — UMR 7095 du CNRS,
Université Pierre & Marie Curie, 98^{bis} boulevard Arago, 75014 Paris.

Title The interplanetary hydrogen: a tracer of the heliospheric interface

Abstract The heliospheric interface results from the interaction between the solar wind and the interstellar medium (ISM). The interplanetary hydrogen (IPH), a population of neutrals that fill the space between planets inside the heliosphere, carries the signature of the ISM and the heliospheric interface: as the incoming ISM ionized component deflects at the heliopause, charge exchange reactions decelerate the bulk motion of the neutrals that penetrate the heliosphere. Inside the heliosphere, the IPH is further affected by the Sun and resonantly scatters the solar Lyman-alpha photons. Solar cycle 23 provided the first partial temporal map of the IPH velocity.

In a first part, I present an updated analysis of IPH velocity measurements from the Hubble Space Telescope spectrometers (GHRS & STIS) and compare these results with those of the SOHO/SWAN instrument and two different time-dependent models. With updates to the HST data points, we now find that all data can be fit by the existing models to within 1σ, with the exception of SWAN observations taken at solar minimum (1997/98). We interpret this discrepancy as a possible effect due to the obliquity of the local interstellar magnetic field.

In a second part, I describe the development of sounding-rocket experiment (HYPE-INSPIRE) which will observe the emission line profile of the IPH Lyman-alpha transition with a Spatial-Heterodyne Spectrometer (SHS), an emerging new class of interferometers. This instrumental work revealed an efficiency anomaly in the diffraction grating used for the payload. I conclude by a description of the current state of advancement of the project with a flight scheduled in 2012.

Key-words Interstellar medium; Heliosphere; Ultraviolet astronomy; Instrumentation; Interferometry; Diffraction gratings.

Laboratory Institut d'Astrophysique de Paris — UMR 7095 du CNRS, Université Pierre & Marie Curie, 98^{bis} boulevard Arago, 75014 Paris.

Acknowledgements

First, I would like to thank Lotfi Ben-Jaffel (Institut d'Astrophysique de Paris) and Walter Harris (UC Davis), my Ph.D. advisers. Without them, none of this adventure would have been possible. Their help was extremely useful during these four years, I learnt a lot thanks to both of them, I really appreciated their availability regarding my questions about science and I hope that will be other opportunities to work together in the future. I also acknowledge financial support from CNES and NASA, which both fund the HYPE-INSPIRE project, including my research work.

Then I would like to thank Romana Ratkiewicz (Space Research Center, Polish Academy of Sciences) and Wayne Pryor (Central Arizona College) for accepting to review this manuscript. I am also thankful to Fred Roesler (University of Wisconsin - Madison), Bruno Sicardy (Observatoire de Meudon), Jean-Pierre Maillard (IAP) and Vladimir Baranov (Institute for Problems in Mechanics, Russian Academy of Sciences) for accepting to be part of my committee.

I am really grateful to Jason Corliss, Edwin Mierkiewicz and Fred Roesler for welcoming and helping me when I arrived at Madison in October 2007. I enjoyed helpful discussions about diffraction gratings with Evgeny Popov (Institut Fresnel). I really appreciated the course of Tony Tyson (UC Davis) on signals and noise, as well as discussions with Jean-Jacques Chattot (UC Davis) about fluid mechanics. Yan Bétrémieux (UC Davis) deserves special thanks for sharing his knowledge about astronomy and instrumentation. I also want to thank the graduate or undergraduate students who have been working with me and brought appreciable help (Sona Hosseini, Oliver Torrealba, Mike Javier, Jake Bobula).

I would like also to thank persons who helped me within the different institutions: at Institut d'Astrophysique de Paris (Jean-Michel Désert, George Debève, Carlos Carvalho, Lysiane Bauby, Geneviève Sakarovitch, Patrick Boissé, Agnès Le Guerer), at the Space Research Center of Warsaw (Jolanta Grygorczuk), at University of Wisconsin (Aimee Lefkow), and at UC Davis (Kathryne Elias, Sally Harmsworth, Felicia Smith, Bob Heyer-Gray). This list is obviously not complete and I have many thanks for colleagues and friends in general.

I am really grateful to my family, especially my parents and my brothers, for their support along the years. Last but not least, I have a special dedication for my wife, Laurène, whose love and support were essential.

Contents

Résumé

Contexte scientifique: l'héliosphère

Avec une vitesse relative d'environ 25 km/s, le système solaire traverse le nuage interstellaire local - un milieu diffus, chaud et partiellement ionisé, principalement composé d'hydrogène atomique. Autour du Soleil, la couronne produit le vent solaire, un flot de particules chargées dont la vitesse varie entre 400 et 2000 km/s. L'interaction entre le vent solaire et la composante ionisée du milieu interstellaire local (MISL) - deux plasmas magnétisés qui ne peuvent se mélanger - donne forme à l'interface héliosphérique, représentée sur la figure 0.1 et dont les dimensions atteignent quelques centaines d'unités astronomiques (e.g. Parker, 1963; Baranov et al., 1971). Suite aux échanges de charge avec les protons du MISL dans l'interface héliosphérique, les atomes d'hydrogène ralentissent avant de pénétrer le système solaire pour y former une nouvelle population: l'hydrogène interplanétaire (HIP) qui diffuse les photons solaires Lyman-alpha (Lyα) et fait l'objet d'observations depuis les années 1970 (e.g. Bertaux and Blamont, 1971; Thomas and Krassa, 1971).

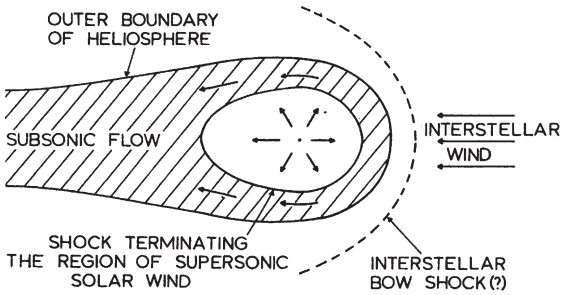

Figure 0.1: Représentation schématique de l'interaction entre le vent solaire et le milieu interstellaire local (adapté de Holzer (1977) par Fahr (2004)).

Contrairement aux particules chargées, les particules neutres traversent l'interface héliosphérique. Parmi les atomes d'hydrogène, une fraction non négligeable (entre 1/3 et 2/3) ne subit aucune interaction et conserve les propriétés physiques du MISL, tandis que l'autre partie ralentit et forme une population plus chaude. A l'intérieur du système solaire, les atomes d'hydrogène subissent principalement deux forces opposées (l'attraction gravitationnelle du Soleil et la pression de rayonnement qui varie avec le cycle solaire) ainsi que différent processus d'ionisation (échange de charges, photo-ionisation, impact d'électrons). Il en résulte des variations de la vitesse de l'HIP avec le cycle solaire, qui ont été observées par l'instrument SWAN (Solar

Wind Anisotropies Quémerais et al., 2006) depuis le satellite *SOHO* (Solar and Heliospheric Observatory), ainsi que les instruments GHRS (Goddard High Resolution Spectrograph Clarke et al., 1998) et STIS (Space Telescope Imaging Spectrometer) sur le satellite *HST* (Hubble Space Telescope).

Durant mon doctorat, mon travail de recherche s'est concentré sur l'étude de l'hydrogène interplanétaire et comportait une partie instrumentale et une partie d'analyse de données.

Instrumentation: spectroscopie UV

Le travail d'instrumentation a porté sur le développement d'un nouveau type de spectromètre: SHS (Spatial Heterodyne Spectrometer) ou SFH (Spectromètre de Fourier Hétérodyne). Cette technique, qui émerge depuis une vingtaine d'années, permet de combiner une haute résolution en longeur d'onde avec un grand champ de vue. L'instrument HYPE (Hydrogen Polarimetric Explorer) est donc un SHS programmé pour faire des observations spectro-polarimétriques de la diffusion du rayonnement solaire Lyα par l'hydrogène interplanétaire lors d'un vol suborbital (Bétrémieux et al., 2010).

J'ai notamment participé aux mesures d'efficacité d'un réseau de diffraction, qui est une pièce essentielle de l'instrument. Cette série de mesures d'efficacité, faite en collaboration avec l'Université du Colorado et le Goddard Space Flight Center (GSFC), a mis en évidence une anomalie d'effiacité pour une incidence normale, anomalie qui a été corrigée par la suite grâce à un revêtement déposé par le GSFC (Fig. 0.2). J'ai contacté un spécialiste des réseaux de diffraction (Evegeni Popov, Institut Fresnel) pour expliquer l'origine de l'anomalie par une modélisation numérique, mais les données expérimentales étaient insuffisantes et cette piste de recherche n'a pas donné de suite.

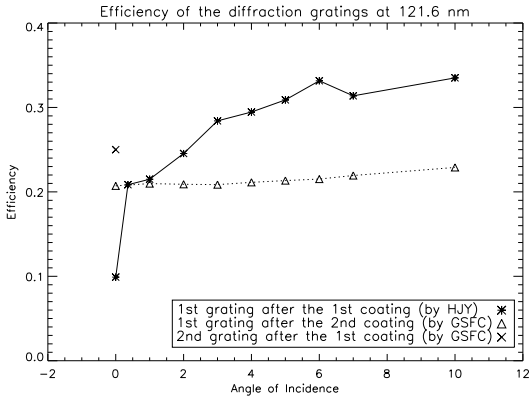

Figure 0.2: Mesures d'efficacité sur les réseaux de diffraction (test et vol) du projet HYPE (Vincent et al., 2011b, JESRP).

Analyse de données: observations HST

Le travail d'analyse de données a porté sur des observations Lyα de l'hydrogène interplanétaire faites par l'instrument STIS sur le satellite *HST*. Ces données avaient la particularité de ne pas être directement analysables par le processus standard, car le mode d'observation utilisé n'est pas supporté par l'équipe du Space Telescope Science Institute (STScI). Il en résulte que la fonction d'appareil n'est pas fournie, il a donc fallu construire une fonction d'appareil à partir de modes supportés proches du mode utilisé.

La plus grande difficulté vint de la superposition de différents ordres du réseau échelle, dûe à l'utilisation d'une grande fente. J'ai ainsi mis en évidence la contamination par un triplet de l'oxygène de la géocouronne, et développé un outil d'ajustement utilisant un algorithme de moindres carrés pour faire l'analyse spectrale de ces données. L'ajustement des raies de l'hydrogène interplanétaire et géocoronal, par des profils de Voigt (figure 0.3), permet d'obtenir la vitesse de l'hydrogène interplanétaire, après soustraction de la vitesse de la Terre projetée sur la ligne de visée.

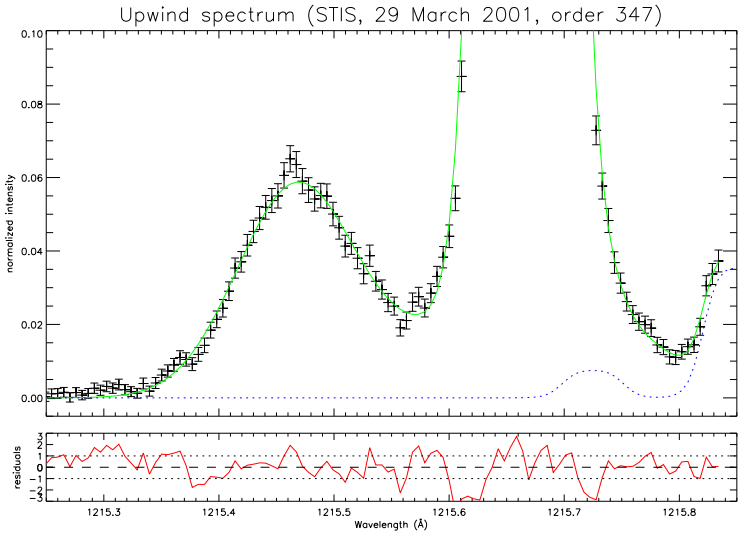

Figure 0.3: Ajustement des données par HST/STIS en 2001. Les deux plus grandes raies sont, en partant de la gauche, l'hydrogène interplanétaire et l'hydrogène géocoronal qui diffusent le rayonnement solaire Lyman-alpha. En bleu, des contaminations dues à l'oxygène géocoronal dont le triplet à 130.4 nm est transmis par d'autres ordres du réseau échelle (Vincent et al., 2011a, ApJ).

Cette analyse a ainsi permis de corriger une divergence entre une précédente analyse de ces données STIS et les observations de l'instrument SWAN. J'ai aussi travaillé sur l'analyse de données GHRS, le prédécesseur de STIS. L'ensemble des données HST/GHRS et HST/STIS permettent de compléter les données SOHO/SWAN et

l'illustration de la variation de la vitesse de l'hydrogène interplanétaire avec le cycle solaire (Fig. 0.4).

L'écart observé entre les données SWAN et le modèle de Quémerais et al. (2008) durant le minimum solaire (1997-1998) pourrait s'expliquer par l'absence du champ magnétique interstellaire dans le modèle. La présence du champ magnétique interstellaire et de son oblicité dans le modéle entraînerait une plus grande variation de vitesse de l'hydrogène interplanétaire à cause d'une plus grande pondération de la vitesse à l'intérieur de l'héliosphère.

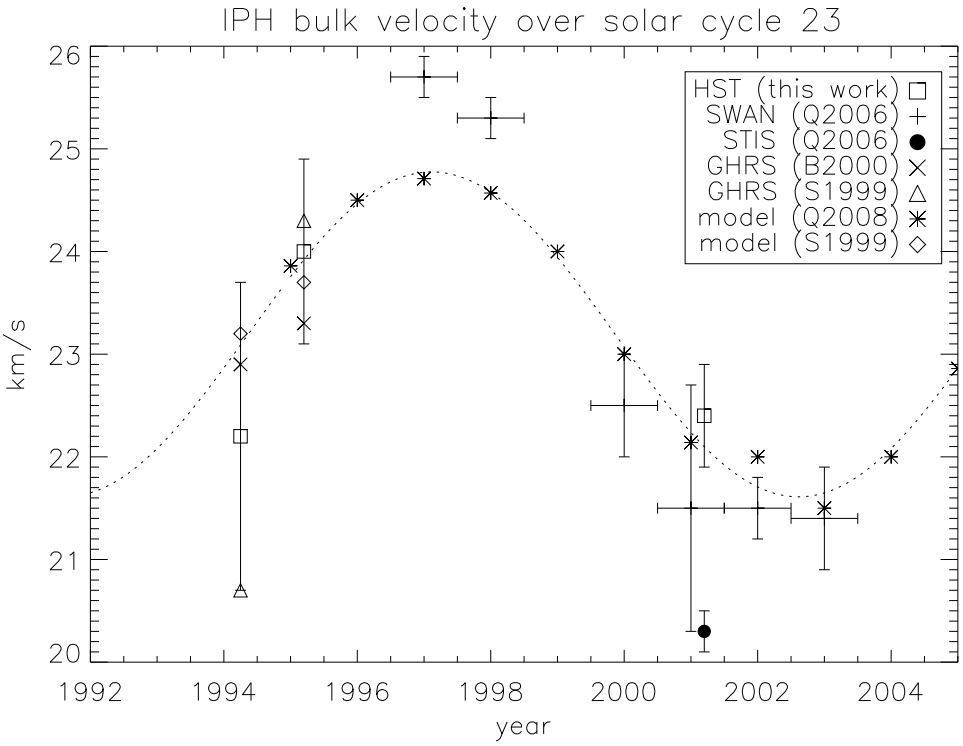

Figure 0.4: IPH bulk velocity in the upwind direction over solar cycle 23 (Vincent et al., 2011a), with values reported by this work (squares for GHRS and STIS), by Quémerais et al. (2006) (plus signs for SWAN data, triangle for STIS observations), by Ben-Jaffel et al. (2000) (crosses) and Scherer et al. (1999) (triangles). The dotted curve is a Fourier interpolation of the model proposed by Quémerais et al. (2008) (asterisks). The values predicted by the model of Scherer et al. (1999) are represented with diamonds.

Introduction

Exploring the interstellar medium

More than a century ago, the discovery of absorption lines in the spectrum of the binary star Delta Orionis by Johannes Hartmann in 1904 opened a new field for astrophysicists. The origin of these absorption lines triggered a scientific debate which lasted more than twenty years. The assumption made by Arthur Edddington who suggested the presence of matter between the stars (Eddington, 1926), was confirmed by independent observations (Struve, 1928; Plaskett & Pearce, 1930). By 1935, a layer of dust as well as of gas extending throughout the Galaxy was generally accepted among the scientific community.

From then, the scientific exploration of the interstellar medium was developed by both theorists and observers. In a seminal paper published in 1939, Bengt Strömgren suggested that young stars (spectral classes O and B) could be surrounded by spheres of ionized hydrogen (H II). Meanwhile some astronomers were mapping the velocity distribution of hydrogen gas within our Galaxy and discovered strong concentrations toward the plane of the Milky Way (e.g. Adams, 1948). In some locations, the interstellar gas can be condensed under the form of so-called interstellar clouds. Assuming the presence of an interstellar magnetic field which can be dragged by interstellar matter through Alfven waves, Enrico Fermi proposed in 1949 a mechanism to describe the acceleration of cosmic rays which had been observed since the begin of the twentieth century.

Fifty years after the discovery of Hartmann, Lyman Spitzer wrote in a review on the interstellar medium that "Study of the stars is one of man's oldest intellectual activities. Study of the matter between stars is one of the youngest" (Spitzer, 1954). Since then, this statement appeared to be true with a consequent number of animated scientific debates and discoveries, especially thanks to the space exploration.

Rocket experiments revealed the presence of a soft X-ray background (Bowyer et al., 1968; Sanders et al., 1977) and suggested the existence of large cavity over dozens of parsecs around the Sun and filled with hot plasma (millions of degrees): the Local (Hot) Bubble. The presence of this hot and ionized gas gave birth to a new class of astrophysical models which take into account the explosions of supernovae (Cox & Smith, 1974; McKee & Ostriker, 1977) as well as stellar winds from massive stars (Castor, McCray, & Weaver, 1975; Weaver et al., 1977) as sources of hot plasma for the interstellar medium .

On the scale of the Galaxy, the massive stars and the supernovae tend to concen-

trate in the spiral arms where the star-forming regions are located. These associations produce superbubbles and supershells which expand and break out of the disk of the Galaxy, expelling clouds of interstellar matter. This mechanism, so-called Galactic fountain or chimney model, has been described by different groups of researchers (Shapiro & Field, 1976; Bregman, 1980; Norman & Ikeuchi, 1989). Near the Sun, the interaction between the Local Bubble and the adjacent Loop I superbubble also expels interstellar clouds, including the Local Interstellar Cloud (LIC) into which the Sun is embedded (Breitschwerdt et al., 2000). The combination of absorption measurements and Doppler triangulation revealed that the Sun has a relative velocity of about 26 km/s by respect to the Local Interstellar Cloud (e.g. Bertin et al., 1993).

Interaction with the solar wind

On a smaller spatial scale, another pioneering work was in development from the 1950's: the existence of the solar wind was suggested by Ludwig Biermann from comets observations (e.g. Biermann, 1957), modelled by Eugene Parker (Parker, 1958) and finally detected in 1962 by the spacecraft Mariner II (Neugebauer & Snyder, 1962). The solar wind results from the expansion of the extremely hot solar corona and reaches supersonic velocities (between 400 and 800 km/s, with peaks up to 2000 km/s during solar flares). Parker (1961) also predicted the existence of a termination shock due to the deceleration of the solar wind.

In the early days of space exploration, sounding-rocket flights started to detect an excess of hydrogen Ly-α emission at 121.6 nm (e.g. Kupperian et al., 1959; Morton & Purcell, 1962), suggesting the presence of hydrogen between the planets within the Solar system: the interplanetary hydrogen (IPH). At the frontier between space physics and astrophysics, the interaction of the solar wind with the interstellar medium was first studied in the early 1960's by different groups of pioneering theorists who also developed the first models describing the interplanetary hydrogen (Patterson et al., 1963; Axford et al., 1963).

Blum & Fahr (1969, 1970) developed a model which was assuming a relative motion of the interstellar gas relative to the solar system and describing the velocity distribution of neutral hydrogen atoms within the heliosphere. Their theoretical work received an experimental confirmation at the same time: launched in 1969, the OGO-5 satellite revealed the presence of an anisotropy in the IPH Ly-α emission pattern (Bertaux and Blamont, 1971; Thomas and Krassa, 1971). This pattern is due to the relative motion of the Sun by respect to the Local Interstellar Cloud into which it is embedded. This flow of gas penetrates the heliosphere and is called the interstellar wind. The presence of the interstellar matter inside the interplanetary environment represents an unique opportunity for the observer to study the ISM on small scales. As stated by Gary Thomas in 1978, "It is as if a geologist were suddenly given the magnifying power to examine an individual atom of a rock sample, where before he was able to view only the individual grains".

The description of the heliosphre and its surroundings is complicated by the fact that the interstellar medium contains charged particles (mainly protons and

electrons) which interact with the solar wind through electro-magnetic forces. The Moscow group (Baranov et al., 1971, 1976, 1979) developed a hydrodynamical model to describe the interaction between two counter-flowing plasmas and predicted the presence of an additional shock: the bow shock which is due to the deceleration of the ISM (assumed to be supersonic).

The Lyman-alpha radiation: a tracer of the heliospheric interface

Since the mid-1970s, different spectroscopic observations of the Ly-α line profile (Mars 7, Copernicus, PROGNOZ, *International Ultraviolet Explorer* (IUE), *Hubbe Space Telescope (HST)* and *Solar and Heliospheric Observatory (SOHO)*) revealed the deceleration of the IPH bulk velocity by respect to the interstellar wind (Bertaux et al., 1976; Adams and Frisch, 1977; Clarke et al., 1984, 1995, 1998; Scherer et al., 1999; Ben-Jaffel et al., 2000; Quémerais et al., 2006). This deceleration is due to charge exchange with protons in the heliospheric interface (Wallis, 1975; Baranov and Malama, 1993), so the IPH carries the signature of the interaction between the ISM and the solar wind. By contrast, the helium atoms are barely affected by the heliospheric interface because of a lower charge-exchange cross-section and their observations by different experiments (e.g. Ulysses, Extreme Ultraviolet Explorer (EUVE)) brought direct information on the local interstellar medium.

Inside the heliosphere, the IPH bulk velocity is further affected by solar gravity, radiation pressure, and ionization processes, with the latter two processes dependent on solar activity (e.g. Quémerais et al., 2006, 2008). During the last two decades, spectroscopic observations by different instruments (the Goddard High Resolution Spectrograph (GHRS) and Space Telescope Imaging Spectrograph (STIS) on *HST*, as well as *SOHO*/SWAN) revealed a variation of the IPH bulk velocity during the solar cycle. This velocity variation is due to the Ly-α radiation pressure which can be smaller or greater than the solar gravitational force on a hydrogen atom. The variations of the IPH bulk velocity have been modelled by different groups (Bzowski et al., 1997; Scherer et al., 1999; Quémerais et al., 2008) and none of these succeeded in reproducing the observed trend within one error bar.

The problem is complicated by the obliquity of the local interstellar magnetic field (LIMF) which tilts the heliosphere relative to the upwind direction. The orientation and the strength of the LIMF have been constrained by a multi-observational approach (*Voyager*, *HST*, *SOHO* and *Interstellar Boundary EXplorer* (IBEX)) which results from the work of different research groups (e.g. Lallement et al., 2005; Ratkiewicz & Grygorczuk, 2008; Heerikhuisen et al., 2010). The obliquity of the LIMF may explain the discrepancy between observations and time-dependent models of the IPH velocity but there is currently no direct proof. On the other side, the current database cover several decades but only the last solar cycle (23) is entirely spanned. Moreover, these observations have been obtained by different instruments which have their own biases and uncertainties. The best future approach is to do a decadal survey with a single instrument that has the sensitivity to get the required measurements.

In this context, the emerging of such new instruments as the spatial heterodyne spectrometer (SHS) represents an opportunity to obtain high-resolution observations of the Ly-α line and can be combined with one-dimensional imaging and polarimetry measurements, which will be definitively helpful to better constrain the problem of the heliospheric interface.

Plan of this dissertation

The first chapter introduces the problem of the heliospheric interface with more details. The second chapter provided an updated analysis of the upwind IPH velocity as observed by GHRS and STIS on board the *Hubble Space Telescope* during solar cycle 23.

The third chapter explains the physical principles of the SHS technique and the optical design of the HYPE-INSPIRE payload which will observe at high-resolution the emission line profile and the polarization of the IPH Lyman-alpha transition. The fourth chapter presents the different challenges that are met in the development of instruments in the vacuum-ultraviolet range, including an efficiency anomaly on the diffraction grating used for the payload.

Publications

The work presented in this dissertation generated two publications as a first author in peer-review journals:

- Vincent, F.E., Ben-Jaffel, L., Harris, W.M.: *Updated analysis of the upwind interplanetary hydrogen velocity as observed by the Hubble Space Telescope during solar cycle 23*, Astrophys. J., 738, 135 (2011)
- Vincent, F.E., Harris, W.M., Beasley, M., Corliss, J., Bétrémieux, Y., Ben-Jaffel, L., Roesler, F.L.: *Identification and treatment of an efficiency anomaly in asymmetrically ruled grating illuminated at normal incidence*, J. Electron. Spectrosc., doi:10.1016/j.elspec.2010.12.033 (2011)

Chapter 1

Interaction between the solar wind and the interstellar medium

1.1 Exploring the interstellar medium

1.1.1 Perspectives: the Milky Way and beyond

A flat layer of stars

Astronomy is a science based on the observation of stars, which can be done with naked eye, so first discoveries belong to antiquity. For instance, Anaxagoras (500-428 BC) and Democritus (450-370 BC) were among the first astronomers to stipulate that the Milky Way should be made of stars.

The Arabian astronomer Alhazen (965-1037 AD) made the first measurement of the Milky Way's parallax. These observations showed no parallax and demonstrated that the Milky Way does not belong to the atmosphere, contrarily to a suggestion made by Aristotle. Other astronomers, for instance in Persia and Andalusia, also suggested that the Milky Way was a collection of stars.

This was confirmed way later by Galileo Galilei (1564-1642) who discovered a huge number of faint stars with the assistance of a telescope providing a 3x magnification. During his observations, Galileo also discovered satellites around Jupiter and deduced that the Earth was in rotation around the Sun.

One century later, Thomas Wright (1711-1786) explained the appearance of the Milky Way as "an optical effect due to our immersion in what locally approximates to a flat layer of stars." in his publication *An original theory or new hypothesis of the Universe* (1750). This idea was taken up and elaborated by Immanuel Kant in his *Universal Natural History and Theory of Heaven*.

The solar apex

Although apparently static, the stars have their own dynamic and their apparent motion in the sky has been studied for centuries. Herschel (1783) made an early

attempt to measure the relative motion of the Sun with respect to the neighbour stars.

By monitoring the parallax of several close stars, he was able to deduce the direction of the Sun (the solar apex) as shown in Fig 1.1. This early estimation ($\alpha = 245°, \delta = 40°$ in celestial coordinates) was not very far from the values determined by more precise instruments nowadays ($\alpha = 270°, \delta = 27°$).

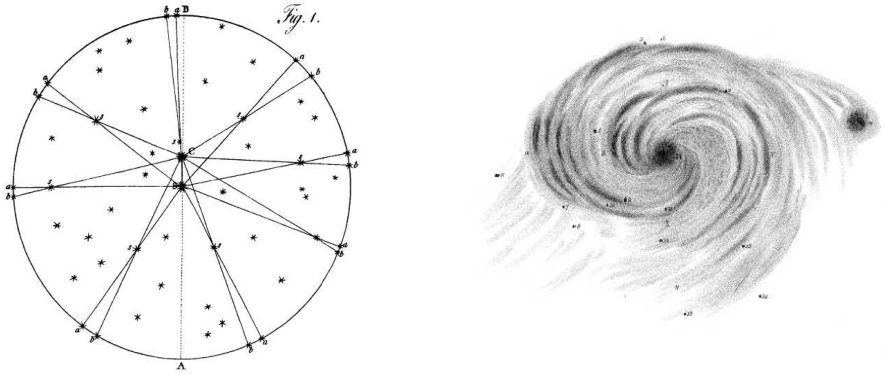

Figure 1.1: *Left:* determination of the solar apex by Herschel (1783). *Right:* Messier 51 sketched by Rosse (1850).

The spiral galaxies and the Universe

Half a century later, Rosse (1850) identified spiral structures in objects identified as nebulae. Using these observations, Alexander (1852) suggested that our Galaxy (the Milky Way) could also have this spiral structure with up to four branches and a central cluster.

Hubble (1925) measured the distance of a spiral nebulae (NGC 6822) by observing of Cepheid variables and found that it was too far away to belong to our Galaxy, showing that the Universe was not limited to the Milky Way. Indeed it appeared that these spiral nebulae are spiral galaxies, similar to but distinct from our Galaxy. Later, Hubble showed that the galaxies are moving away from each other, bringing evidence for the fact that the Universe is in expansion.

1.1.2 Detection of the interstellar matter

Mysterious absorption lines

For a long time, the common conception was that the space between the stars was completely void of any matter. This vision was challenged by the development of the spectroscopy. The first detection of the interstellar medium (ISM) happened in the beginning of the 20th century : while studying the spectrum of the binary star Delta Orionis, Hartmann (1904) observed absorption lines (K line at 3933.7 Å) showing the presence of singly ionized calcium (Ca^+ or Ca II). He noticed that this

line was weaker but more sharply defined, moreover it did not share the periodic displacement of the lines caused by the orbital motion of the star. He then suggested the presence of vast diffuse clouds standing in front of the stars and at rest with the galactic system.

As described by Thorndike (1930), the discovery of these absorption lines gave birth to a debate with two rival hypotheses about their origin. On one hand, Plaskett (1923) supposed that the absorption takes place only in the neighbourhood of hot stars, where the calcium atoms would be ionized, so the intensity should depend on spectral type. On the other hand, Eddington (1926) proposed that the absorption occurs throughout space and its strength should depend only on distance. Struve (1928) made absorption measurements in O/B stars (hot and luminous stars) that showed no dependence of intensity on type, while the distance seemed to be the principal factor determining the amount of absorption, supporting Eddington's explanation.

Plaskett & Pearce (1930) brought an independent confirmation: by subtracting the solar motion from radial velocities of the observed lines, they determined the rotational term that depends on galactic rotation and is proportional to the distance of the line source. The distances of the observed stars were found to be significantly larger than the distances of absorption sources, bringing definitive evidence for the existence of interstellar matter under the form of clouds.

The interstellar medium: a complex blending of dust and gas

As described in a seminal book by Spitzer (1968), it was also in the 1930s that the concept of a general absorbing medium in the Galaxy, composed of dust grains, began to gain general acceptance.

The presence of such an absorbing layer had already been deduced in the previous century from the star counts by Struve (1847), whose mean extinction coefficient of 1 mag/kpc is not far below present estimates, but reliable evidence for general extinction required objects of known brightness at a distance determined geometrically rather than photometrically.

There were provided by measures of the diameters of galactic clusters (Trumpler, 1930), investigation of the distribution of Cepheids perpendicular to the galactic plane (Bottlinger & Schneller, 1930), and analysis of the concentration of external galaxies to the poles of our own Galaxy (van de Kamp, 1932). By 1935, a layer of dust as well as of gas extending throughout the Galaxy was generally accepted.

Beals (1936) found double and asymmetric profiles in absorption measurements, suggesting the presence of distinct interstellar clouds on the line of sight. Adams (1948) retrieved kinematic information from absorption lines, and demonstrated that the velocities differed within the Galaxy and the distribution of gas is not uniform with strong concentrations toward the plane of the Milky Way. First interstellar hydrogen maps arrived with 21 cm observations, after the prediction of the hyperfine structure transition of HI by van de Hulst in 1945.

1.1.3 Early-type stars, cosmic rays and magnetic fields

Embedded stars were clearly a source of energy: Strömgren (1939) showed that early-type stars will form ionization fronts, expanding because of overpressure and driving a shock wave into the interstellar medium but only a tiny fraction of this energy is converted into kinetic energy, so other sources had to be searched.

Acceleration of cosmic rays

Cosmic rays are energetic charged particles, mostly protons, originating from outer space. The term ray is historical as cosmic rays were thought to be electromagnetic radiation. Fermi (1949) suggested that the cosmic rays were accelerated primarily in the interstellar space of the galaxy by collisions against moving magnetic fields. Relative dense clouds with a root-mean square motion of about 30 km/sec create streaming motions in the tenuous and ionized intercloud medium (0.1 atom/cc). Magneto-elastic waves will convert the kinetic energy into magnetic energy (Alfven, 1942) and build up a magnetic field (about 5 μG, or 0.5 nT). The lines of force will form a crooked pattern since they will be dragged in all directions by the interstellar matter.

Fast particles (a few GeV, so close to the velocity of light) will spiral around these lines of forces until it collides against an irregularity in the cosmic field (region of high intensity field or curved line of force) and so are reflected. If the magnetic field is slowly variable, the particle will gain or lose energy after the reflection. The net result will be an average gain, because head-on collisions (energy gain) are more frequent than overtaking collisions (energy loss). This relatively simple model yields an inverse power law for the spectral distribution of the cosmic rays. A comparison with data then available gives a mean distance between collisions of the order of a light-year.

The interstellar magnetic field

The existence of a magnetic field in the interstellar medium was confirmed by polarization observations in the direction of distant arms. The polarization is due to a magnetic orientation of the interstellar dust particles, leading to different amounts of absorptions of light polarized parallel and perpendicular to the magnetic field. The first maps of the polarization effect showed that the galactic magnetic field was roughly parallel to the direction of the local arm.

By considering the velocity of magneto-hydrodynamic waves, Chandrasekhar & Fermi (1953) demonstrated that the magnetic field is inversely proportional to the angular deviation between the plane of polarization and the direction of the spiral arm, deducing an estimate of 7.2μG for the field intensity. With an independent method, they derived an estimate of 6μG, using the requirement of equilibrium of the spiral arm with respect to lateral expansion and contraction.

The 2-phases medium

Pikel'Ner (1967) and Field et al. (1969) proposed an ISM model based on these cosmic rays. They envisaged the ionization of the ISM by low energy cosmic rays, and energy losses by collisional excitation, giving birth to two-phase medium: a cold neutral phase (300 K, 100 cm^{-3}) coexisting with a warm and weakly ionized phase (10^4 K, 0.3 cm^{-3}).

1.1.4 Supernovae and stellar winds

Hot plasma in the Galaxy

This two-phase model was challenged by early space missions. A pioneering rocket experiment, made by Bowyer et al. (1968), revealed the existence of diffuse soft X-ray emission in the 44-70 Å band, which corresponds to an energy range below 1 keV. This emission could be decomposed into an extragalactic component and an anomalous component, whose origin might be Galactic.

Launched in 1972, the satellite COPERNICUS observed the O VI line (Ultraviolet doublet at 1032 Å and 1038 Å) and detected absorbing regions well separated from the circumstellar medium, leading to the establishment of a widespread hot interstellar medium (Jenkins & Meloy, 1974; York, 1974) with $5.4 < \log(T) < 6.3$. These discoveries confirmed the suggestion, made by Spitzer (1956), for a hot Galactic corona (10^6 K) which provides a pressure confining medium for high velocity clouds.

Another rocket experiment (Sanders et al., 1977) confirmed the presence of the soft X-ray background. They showed an inverse correlation between the soft X-ray background intensity and the column densities of the neutral hydrogen. As the correlation is the same for different wavelengths range, absorption was discarded and it was interpreted as a displacement effect: X-ray emission regions seem to be where the cool gas is not. The Sun seemed to be surrounded by a hot X-ray emitting region : the Local Hot Bubble. However, we will see later in this section that recent observations showed that the Local Hot Bubble may not be as hot as previously thought.

The 3-phases models: supernovae explosions

To explain the presence of this hot plasma suggested by observations, Cox & Smith (1974) proposed a model where the prime energy sources in the ISM are the type II supernovae (SNe). With Monte-Carlo techniques, they simulated the filling of a uniform disk by randomly occurring explosions of SNe, creating a tunnel network of hot bubbles (10^6 K, $n < 10^{-2}$ cm^{-3}) in an ambient medium of higher density (1 cm^{-3}). Shapiro & Field (1976) examined the consequences of this proposal within the context of a time-dependent model, and proposed a *galactic fountain* model in which the hot gas rises about 1 kpc before cooling and condensing to form clouds which fall to the plane at ∼100 km s^{-1}.

McKee & Ostriker (1977) developed another ISM model, also dominated by SNe explosions in the Galactic disk, but they described a general picture with three dis-

tinct phases (Fig. 1.2). It consists of cold dense cores (80 K, 40 cm^{-3}), surrounded by a warm (8000 K, 0.4-0.04 cm^{-3}), partially ionized envelope, and embedded in a hot, ionized, tenuous and soft X-ray emitting medium (10^6 K, 5×10^{-3} cm^{-3}). Models from Cox & Smith (1974) and McKee & Ostriker (1977) use the same fundamental concept: the supernovae are the main energy source of the ISM, producing hot and X-ray emitting plasma all over the disk and halo, by interaction with an inhomogeneous substrate. However they have very different point of views about the fraction of hot gas (filling factor) in the disk of the Galaxy.

Maíz-Apellániz (2001) made an interesting analogy to explain how different are these interpretations of the interstellar medium. McKee & Ostriker (1977) proposed a high filling factor (f∼0.8) with hot bubbles occupying most of the available volume, suggesting that the general morphology of the interstellar medium is that of a "bubble bath". On the contrary, Cox & Smith (1974) advanced a relatively low filling factor (f∼0.2) with hot bubbles occupying a smaller fraction of the volume, envisioning the ISM as a "Swiss cheese".

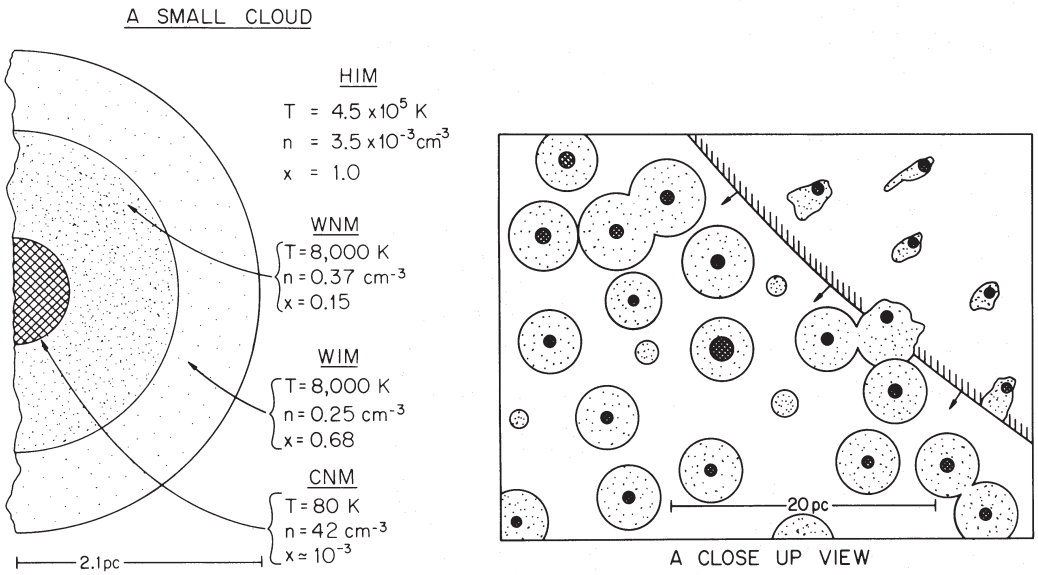

Figure 1.2: *Left*: Cross section of a characteristic cloud.*Right*: small-scale structure of the interstellar medium. A supernova blast wave is expanding from the upper right. Figures from McKee & Ostriker (1977).

Stellar winds

Another mechanism based on stellar winds was suggested to explain the creation of bubbles of hot plasma (Castor, McCray, & Weaver, 1975; Weaver et al., 1977). Massive stars (such as Wolf-Rayet or OB stars) blow bubbles in the interstellar medium with radii about 30 pc, T≈ 10^6K and n≈0.001 cm^{-3} as typical conditions in the interiors. The column density of O VI in the interior could explain previous observations by the *Copernicus* telescope.

1.1.5 The chimney model

The pervasiveness of the intercloud medium

The high filling factor for the hot gas in the model of McKee & Ostriker (1977) was challenged by H I observations: Heiles (1980) showed the pervasiveness of the warm neutral "not strongly absorbing" gas (intercloud medium) with the existence of large HI holes in the Milky Way.

These observations converged with the possibility that the Type II supernovae should be highly correlated in space and time: indeed massive stars tend to be found in OB associations, which in turn concentrate in gas-rich spiral arms (Scott, Jensen, & Roberts, 1977; Shu, 1978). This could produce a generally pervasive intercloud medium except in large, isolated volumes that have been recently affected by a large numbers of supernovae.

OB associations

Norman & Ikeuchi (1989) proposed that evolving OB associations produce superbubbles and supershells fed by tens or hundreds of supernovae per bubble: these objects expand quickly and break out of the disk of the Galaxy. The collimated structure formed in this process are called chimneys. The cycle is completed by the downward flow, from the halo to the disk, of gas that has cooled and formed clouds.

This is similar to the galactic fountain model proposed by Shapiro & Field (1976) and Bregman (1980) but with a highly concentrated upward energy flows in chimneys rather than over the entire disk (Fig. 1.3).

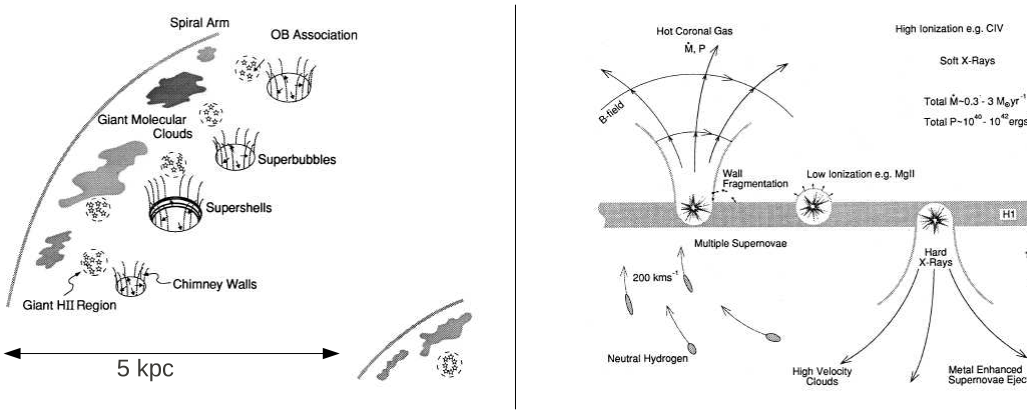

Figure 1.3: *Left*: Schematic diagram of superbubbles formation in the disk powered by massive OB associations formed from giant molecular clouds associated with spiral arms. *Right*: A sketch of some qualitative aspects of the halo structure in the chimney model. The length scale is about several kpc. Figures adapted from Norman & Ikeuchi (1989).

The galactic wind

As explained in the following section with more details, the discovery of the soft X-rays background by Bowyer et al. (1968) has been first interpreted by the emission of a hot plasma (about 10^6 K) around the Sun. However more distant contributions require another explanation, as their origin are unclear.

Breitschwerdt & Schmutzler (1994) proposed that the delayed recombination of ions and electrons is a source of X-rays. This would be the result of the rapid adiabatic expansion of hot gas driven by the explosions of massive stars: this hot gas cools quickly, 'freezing in' highly ionized atomic states before the recombination which takes place in a large-scale cosmic-ray and thermally driven wind.

Everett et al. (2008) applied a wind model, driven by combined cosmic-ray and thermal pressure, to the Milky Way, and showed that the observed Galactic diffuse soft X-ray emission can be better explained by a wind than by previous static gas models.

1.1.6 The Local Cavity

The model of the Local (Hot) Bubble

Since the discovery of the soft X-rays background by Bowyer et al. (1968), the so-called Local Bubble has been the subject of multi-wavelength studies, including UV measurements. Although there is a contribution from the galactic halo and extra-galactic sources, the soft X-ray background (SXRB) seemed to be mostly emitted by highly ionized atoms inside the Local Bubble. Thus it was possible to probe the dimensions of this cavity, by measuring the intensity of the emission.

Cox & Snowden (1986) summed up observations to give the three dimensional structure of the SXRB region : the Local Bubble is more extended in the direction of the galactic poles (200 pc) than in the galactic plane (30 pc), and its volume is roughly equivalent to a sphere with a radius of 100 pc. More detailed observations were provided with X-ray measurements by the satellite ROSAT Snowden et al. (1995).

On the other hand, 21-cm observations indicate that the neutral hydrogen is confined to the galactic plane (Dickey & Lockman, 1990), as shown in Figure 1.4. As previously said, this anti-correlation can be interpreted as a displacement effect and pleads for the existence of the Local Hot Bubble, where the Sun is surrounded by a tenuous and hot plasma.

Scenarios of formation

To explain the origin of the Local Bubble, Maíz-Apellániz (2001) proposed a scenario of formation with the explosions of several nearby supernovae within the last 10 millions years. He showed that part of the Scorpius-Centaurus (Sco-Cen) OB association was located closer to the present position of the Sun 5-7 millions years ago than today.

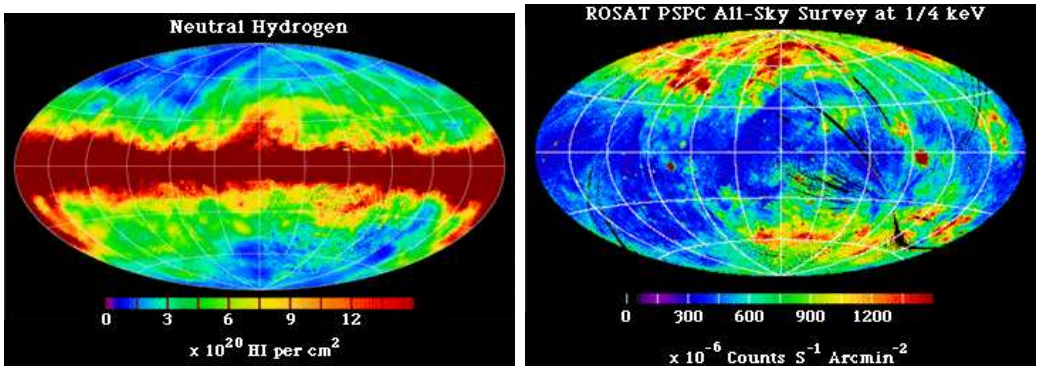

Figure 1.4: *Left*: map of the column density of Galactic neutral hydrogen. Figure from Dickey & Lockman (1990). *Right*: map of the soft X-ray diffuse background, from the ROSAT all-sky survey. Figure from Snowden et al. (1995).

Berghöfer & Breitschwerdt (2002) analyzed the trajectories of moving stellar groups in the solar neighbourhood during the past 20 million years. They showed that the subgroup B1 of the Pleiades, consisting of early type B stars, passed through the Local Bubble. The most massive members should have already ended as supernovae, but the later-type stars should be still present. Applying an initial mass function appropriate for OB stars, they inferred the number of members that may have exploded within the region that now forms the local cavity, and concluded that the Local Bubble could have been created by about 10-20 supernovae about 13 millions years ago.

The trouble with the Local Bubble model

Very recently, the model of the Local Bubble has been seriously challenged. Observations of the Comet Hyakutake unveiled a then-unknown X-ray production mechanism, caused by the de-excitation of solar wind ions following charge exchange with neutral material. This mechanism could also happen in the interaction of solar wind ions with interstellar neutrals (Cravens, 2000), and it then appeared that most of the soft X-rays background (SXRB) would be due to this local emission.

The Local Bubble would not need to be as hot as required to explain the SXRB. Moreover re-examination of UV absorption measurements made by FUSE showed that O VI was less present than expected and may exist only for high galactic latitudes, bringing new evidence for the absence of hot plasma in the solar neighbourhood in the galactic disk.

A new model: the Local Cavity

Welsh & Shelton (2009) proposed an alternative model where the Local Cavity is filled by a warm and diffuse gas (T∼20,000 K) that is in rough pressure equilibrium with numerous partially ionized and warm (T∼7,000 K) small cloudlets.

The Local Cavity was mapped by interstellar Na I absorption measurements (e.g., Welsh et al., 2010), as shown in Figure 1.5. One possible explanation for the origin of the Local Cavity would be the remnant of a supernova that exploded more than a million years ago and has been cooling since.

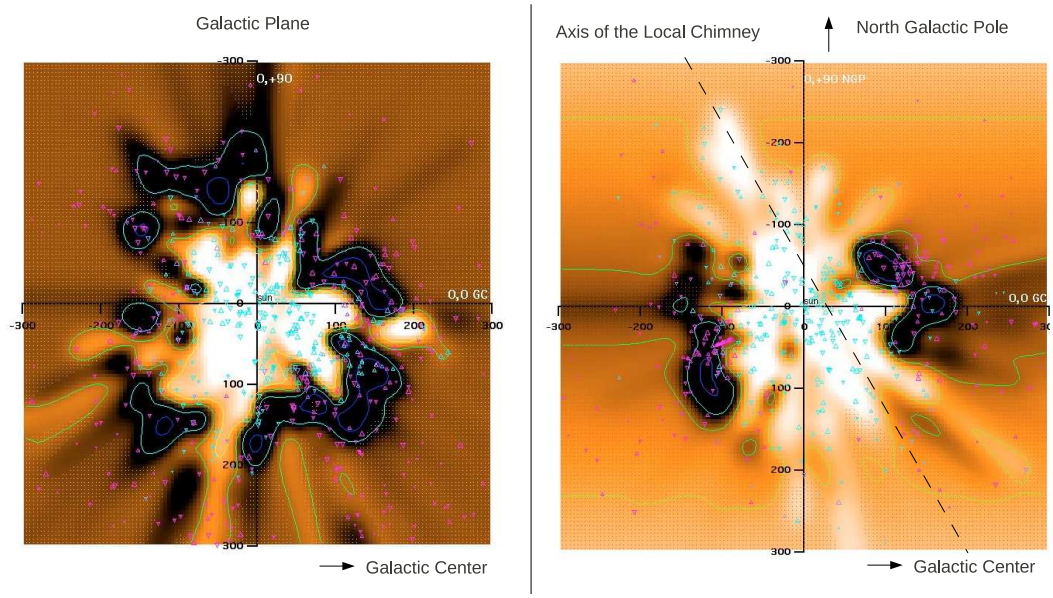

Figure 1.5: Plots of 3D spatial distribution of interstellar NaI absorption within 300 pc of the Sun as viewed in the Galactic plane projection (left) and in the meridian plane projection (right). White-to-dark shadings represents low-to-high values of the Na I volume density, which outline the edge of the Local Cavity. Figures adapted from Welsh et al. (2010).

1.1.7 The Local Interstellar Cloud

Detection of the Lyman-alpha glow

In November 1955 and March 1957, rocket measurements of the night sky from an altitude of about 120 km revealed the presence of a diffuse Lyman-α glow with a radiance of 3.2×10^{-3} erg cm^{-2} s^{-1} sr^{-1}, so about 200 R (Kupperian et al., 1959). A broad band of the sky allowed a mapping of the directional intensity contours with a minimum near the anti-solar direction, as shown in Figure 1.6. The existence of this minimum implies that the mean free path of a solar Lyman-α photon before scattering is larger than 1 AU, otherwise the multiple scattering would destroy the directionality of the radiation seen from Earth.

In April 1961, the Lyman-alpha (Ly-α) glow was also detected by Morton & Purcell (1962) with a sounding rocket flying a hydrogen absorption cell in front of a Ly-α detector. An excess emission was detected but it was first interpreted as solar

Ly-α radiation, resonantly scattered by hydrogen atoms either in the Earth's upper atmosphere (geocorona) or in interplanetary space.

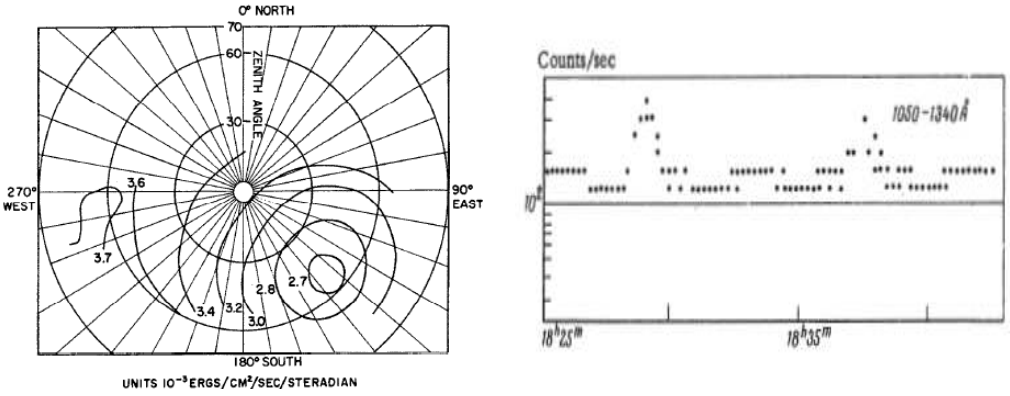

Figure 1.6: *Left:* Ly-α directional intensity contours obtained during a rocket flight above 120 km on 28 March 1957 by Kupperian et al. (1959). *Right:* Measurements of the ultraviolet background radiation in the range 1050-1340 Å by the photon counters on board the spacecraft Venera-2 at a distance of 164,000 km from the Earth. The field of view described a cone around the anti-solar direction (Kurt & Syunyaev, 1967).

Early models and new observations of the interstellar hydrogen atoms

At the same time, Parker (1958) modelled the formation of the solar wind that was detected by Neugebauer & Snyder (1962). Parker (1961) also studied the interaction of the solar wind with the interstellar medium, predicted the existence of a termination shock and, among other theoretical cases, considered the possibility of an interstellar wind.

First models of interstellar neutral hydrogen described the charge exchange between solar protons and interstellar hydrogen beyond the termination of the solar wind (Axford et al., 1963; Patterson et al., 1963). The termination shock was assumed to be due to the galactic magnetic field and located at about 50 AU. However these models did not include any relative motion between the Sun and the interstellar medium, assuming an isotropic transition region for charge exchange.

Interplanetary stations (Zond-1, Venera-2/3/4 [1]) provided new data with partial scans of the night sky and revealed an emission in the direction of the Milky Way (Kurt & Syunyaev, 1967; Kurt & Dostovalov, 1968), as shown in Figure 1.6.

Finally Blum & Fahr (1969) suggested that interstellar hydrogen in the vicinity of the Sun has a macroscopic motion relative to the solar system, resulting into an anisotropy of the interstellar influx of hydrogen atoms.

[1]Venera is the Russian name for Venus. Both names are used to designate the spacecraft in the English-speaking literature, which may be a source of confusion for the unaware reader.

Evidence for the interstellar flow of hydrogen

The idea of a macroscopic motion of the interstellar hydrogen relative to the solar system received different experimental confirmations during that period. The spacecraft OGO 3, Vela 4 and Mariner 6 (Mange & Meier, 1970; Chambers et al., 1970; Barth, 1970) revealed an anisotropy in the Ly-α interplanetary radiation.

A definitive confirmation came from the OGO-5 satellite which completed three spin-up manoeuvres at an altitude of 90,000 km (outside the geocorona) between September 1969 and April 1970. This experiment obtained the first all-sky maps of the intensity of the 1216 Å Lyman-alpha emission with two different photometers (Bertaux and Blamont, 1971; Thomas and Krassa, 1971). The spatial distribution of this emission showed a maximum of 530-570 Rayleighs near the ecliptic plane and a minimum of 200-240 Rayleighs which is diametrically opposed to the emission maximum. These emission maximum and minimum correspond respectively to the upwind and downwind directions of the interstellar flow of hydrogen by respect to the solar system.

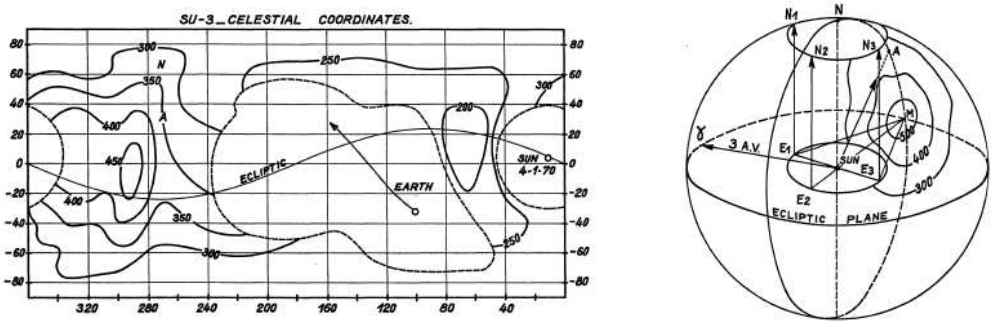

Figure 1.7: *Left:* Contour map of the Ly-α intensity in Rayleighs obtained during the third spin-up (SU) of the satellite OGO-5 at an altitude of 90,000 km on 1-3 April 1970. *Right:* Contours map of the maximum region is projected on the inside surface of a sphere of 3 AU. E1, E2, E3 are the positions of the Earth on its orbit around the Sun respectively for SU-1, SU-2, SU-3. Figures from Bertaux and Blamont (1971).

The maximum region was characterized by an apparent displacement of about 50° between the September 1969 and April 1970 observations. This apparent displacement was interpreted as the parallax effect of the Earth's motion on its orbit, bringing evidence that the emission of this maximum originates from a distance of about 3 AU from the Sun.

Doppler triangulation

The Local Interstellar Medium has a complex structure within scales of dozens of parsecs, with many other clouds in addition of the LIC. Each cloud has its own

physical properties, including number density, velocity and temperature. Column densities can be estimated by measuring absorption of the star light by the interstellar medium, for instance in the visible range with elements as calcium or magnesium. If the line-of-sight crosses several clouds, each cloud will have its own signature: the absorption intensity depends on the cloud column density, the absorption feature is Doppler-shifted because of the cloud motion, and the width of the absorption feature is related to the cloud temperature.

The Aurelie spectrometer at the 1.52-m telescope of the Observatoire de Haute-Provence (France) was used to measure interstellar Ca II absorption lines on the path to 6 nearby stars from the antigalactic center hemisphere (Lallement & Bertin, 1992). These high-resolution spectroscopic observations were used to identify and characterize the Local Interstellar Cloud in which the Sun is embedded.

Thus it is possible to reconstruct by triangulation the velocity vector of this cloud (see figure 1.8), which is 26±1 km/s in the direction given by l_{II}=186±3° and b_{II}=-16±3° (galactic coordinates).

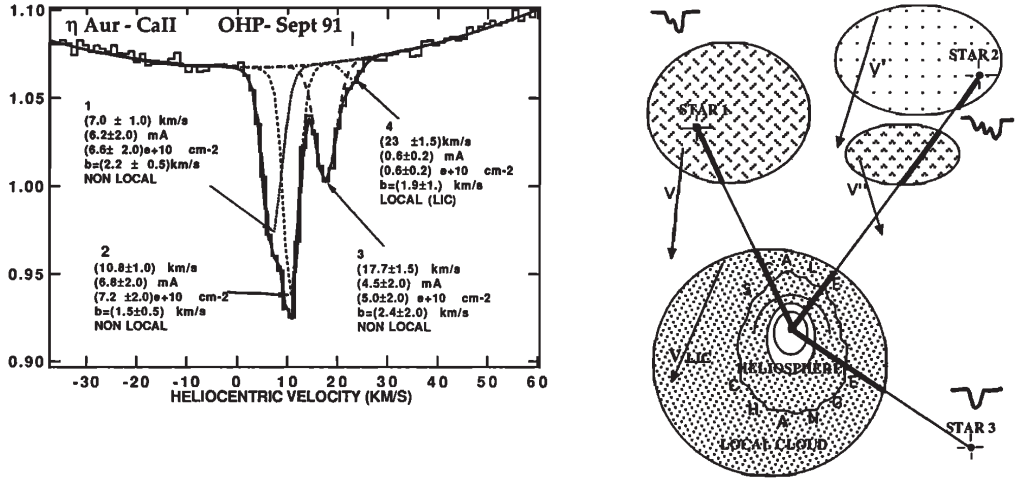

Figure 1.8: *Left*: a complex line of sight. Four absorbing clouds are detected, the fourth is found to correspond to the Local Interstellar Cloud (Lallement & Bertin, 1992). *Right*: a schematic view of our interstellar environment. The Sun is embedded within one of the diffuse clouds, which are themselves embedded within a hot and tenuous medium. The number of absorption lines imprinted in the spectra depends on the number of diffuse clouds along the line of sight (LOS). Each line is shifted because of the motion of the cloud along the LOS, so the velocity vector of the LIC can be deduced by Doppler triangulation (Bertin et al., 1993).

Interstellar helium atoms

Because of a small cross-section for charge-exchange with protons, helium atoms cross the heliospheric interface without any interaction and provide a good tracer of the interstellar flow. Using measures made by the spacecraft Ulysses near the

Earth, Witte et al. (1993) computed the velocity vector of the interstellar neutral helium and found ($\lambda = 252 \pm 2.4°, \beta = 2.5 \pm 2.7°$) in ecliptic coordinates, so a value very close to the results of Bertin et al. (1993). The upwind direction of the interstellar flow is relatively close to the direction of the galactic center (about 17° away) and almost coincides with the direction of the Scorpius-Centaurus (Sco-Cen) OB association.

Origin of interstellar clouds in the Local Bubble

Breitschwerdt et al. (2000) proposed a model to explain the origin of interstellar clouds, including the LIC also called the Local Fluff, surrounding the solar evidence. They described a mechanism of producing neutral hydrogen clouds by a hydromagnetic Rayleigh-Taylor instability, which would happen between our local bubble and the adjacent Loop I superbubble, provided there exists a pressure imbalance between two interacting bubbles.

This scenario of small compact cloudlets expelled from the bubble interaction zone could also happen in several other places in the Galaxy, because of the tendency of bubbles to cluster and concentrate in spiral arms as the star forming regions.

1.2 The solar wind

The solar wind is the supersonic outflow of completely-ionized gas from the solar corona. It consists of protons and electrons with an admixture of a few percent of alpha particles (helium nuclei) and heavy, much-less-abundant, ions in different ionization stages. The solar magnetic field lines are dragged away by the wind, because of its high conductivity, and transform into heliospheric field lines, which attain the form of spirals due to solar rotation.

1.2.1 History of the discovery

The solar wind has a direct and visible impact on Earth: aurorae have been reported in the ancient literature from both East and West. In 1731, the French philosopher de Mairan proposed that the aurora was connected to the solar atmosphere, he suspected a connection between the return of sunspots and the aurora. In 1859, Carrington and Hodgson observed independently a solar flare that was followed by a geomagnetic storm the day after. Carrington suspected a connection between both events and suggested the existence of a continuous stream of particles flowing outward from the Sun.

Around 1916, Birkeland showed with geomagnetic surveys that auroral activity was nearly uninterrupted, he concluded that the Earth was continually bombarded by charged particles emitted by the Sun. Chapman proposed that the geomagnetic storm is the result of a coherent cloud ejected from the sun with a thousand km/s velocity at the time of a solar flare. In the early 1950s, Biermann pointed out that the observed motions of comet tails would seem to require gas streaming outward

from the Sun. He suggested that gas is often flowing radially outward in all directions from the Sun with velocities ranging from 500 to 1500 km/s.

Eugene N. Parker showed that the solar wind originates from the hot corona (about 2 MK) that expands radially into interplanetary space (Parker, 1958). This flow becomes supersonic at a few solar radii. The spacecraft Luna 2 and Mariner II brought experimental confirmation with measurements of the plasma parameters (Neugebauer & Snyder, 1962).

1.2.2 The Sun

As described by Parker (1963) in a seminal book about the interplanetary processes, the Sun can be modelled as a steady emission of black-body radiation and corpuscles with some particular events for the Earth (e.g. aurora and geomagnetic storms). Obviously the reality is more complex than this global picture.

Overview

The Sun is a G2V star with a mass $M_\odot \simeq 2 \times 10^{30}$ kg and a radius $R_\odot \simeq 7 \times 10^5$ km. Its energy comes from nuclear fusion within its core. This core is enveloped by two successive layers: the radiative zone and the convective zone.

The photosphere is the visual surface and emits a black-body radiation with a temperature of 5,800 K. The escape velocity from this surface is equal to $v_{esc} = \sqrt{2GM_\odot/R_\odot}$, where G is the gravitational constant ($G \simeq 6.67 \times 10^{-11}$ N m kg^{-2}), so a numerical application gives: $v_{esc} \simeq 620$ km s^{-1}.

The Sun's atmosphere contains two other layers: the chromosphere and the corona. While the chromosphere is relatively thin (about 2,000 km), the corona is considerably larger and extends over millions of kilometres.

Early observations of the corona

Walter Grotrian in 1939 and Bengt Edlen in 1941 identified coronal emission with highly ionized elements, indicating that the Sun's outer atmosphere has a temperature of millions of degrees. The conspicuous green line was identified with Fe XIV, an iron atom missing 13 electrons. Other ions like Ca XV were identified and confirmed the hot temperature of the corona (e.g., Billings, 1959).

Observation showed that the visible light of the solar corona is due to scattering of light by free electrons and dust particles surrounding the Sun (e.g., Blackwell, 1956). Polarization measurements allowed to separate the components and it was established that the electron density in the corona was of the order of 10^8 cm^{-3} in the low corona.

These different observations show that the solar corona is a very-hot highly-ionized medium. Using these orders of magnitude, Parker (1958) demonstrated how the solar corona has to expand into the interplanetary space.

1.2.3 Models of solar wind

The model of a hydrostatic atmosphere

The heating of the solar corona and the acceleration of the solar wind are among the important unsolved problems of space plasma and solar physics. Indeed the expansion of the corona can not be demonstrated directly and one has to use a demonstration by contradiction. For this purpose we assume that atmosphere is static and non-expanding. Based on this assumption, we are going to show the impossibility of a static atmosphere.

One models the hydrostatic atmosphere by the balance between the pressure gradient and the gravitational force. Taking G as the gravitational constant, $M_\odot$ as the Sun's mass, and ρ as the corona's mass density, we obtain:

$$\frac{dp}{dr} = -\frac{GM_\odot \rho}{r^2} \tag{1.1}$$

Let us consider that the atmosphere is fully ionized but electrically neutral, so the density of protons is locally equal to the density of electrons ($n = n_p \simeq n_e$). Then we assume the coronal protons and electrons to have the same temperature ($T = T_p \simeq T_e$) and to follow the ideal gas law. So we easily get:

$$p = n_p\, k_B\, T_p + n_e\, k_B\, T_e \simeq 2\, n\, k_B\, T \tag{1.2}$$

where k_B is Boltzmann's constant. From equation (1.2), we obtain the following expression for the coronal mass density: $\rho = n\, m \simeq (m_p + m_e)\, p \,/\, 2\, k_B\, T$, where m_p and m_e denote the masses of the proton and the electron, respectively. The electron mass is negligible by respect to the proton mass ($m_e \ll m_p$), so one can write $\rho \simeq m_p\, p \,/\, 2\, k_B\, T$. By substituting this expression of ρ in the equation (1.1), we deduce an equation that describes the hydrostatic atmosphere:

$$\frac{1}{p}\frac{dp}{dr} = -\frac{GM_\odot m_p}{2k_B T}\frac{1}{r^2} \tag{1.3}$$

Temperature profile for the corona

To solve this differential equation, we need to know the temperature profile. In the outer corona, radiation losses are negligible compared to conductive transport, so the temperature is described by the stationary heat flow equation:

$$\nabla \cdot (\kappa \nabla T) = 0$$

With spherical coordinates, we obtain an integral equation :

$$4\pi r^2 \kappa(T) \frac{dT}{dr} = const \tag{1.4}$$

where $\kappa(T)$ is the thermal conductivity of the gas. Spitzer (1956) showed that the thermal conductivity of a fully ionized gas can be written as $\kappa(T) = \kappa_0 T^{5/2}$.

By substituting this expression in equation (1.4), the integral equation becomes $r^2 T^{5/2} dT/dr = const.$ With the realistic assumption that the temperature is null for any point located at the infinity, one can resolve this equation and find that the temperature profile follows a power law:

$$T(r) = T_0 \left(\frac{r_0}{r}\right)^{2/7} \tag{1.5}$$

where T_0 is the temperature in the low corona. The distance r_0 represents the inner radius of the low corona and can be assumed to be equal to the radius of the Sun ($r_0 \simeq R_\odot$) because the chromosphere is relatively thin. A corona with a moderate temperature (10^6 K) yields a temperature of about 2×10^5 K at the orbit of the Earth, and about 6×10^4 K at 100 AU.

The coronal expansion

By substituting this temperature profile in the equation 1.3 and using $p_0 = 2 n_0 k_B T_0$, we obtain:

$$\frac{1}{p}\frac{dp}{dr} = -\frac{G\, M_\odot\, m_p\, n_0}{p_0\, R_\odot^{2/7}} \frac{1}{r^{12/7}}$$

This differential equation can be directly integrated and gives the pressure as a function of the distance r:

$$p = p_0\, exp\left\{\frac{7\, G\, M_\odot\, m_p\, n_0}{5\, p_0 R_\odot}\left(\left(\frac{R_\odot}{r}\right)^{5/7} - 1\right)\right\} \tag{1.6}$$

As one would expect, the pressure decreases with increasing distance r, but it does not decrease fast enough and one obtains a non-null pressure at the infinity. In order to compute the pressure at the infinity (for comparison with the pressure of the local interstellar medium), one needs first to estimate the pressure at the base of the corona. Based on observations, one can consider a density of about 10^{14} electrons per cubic meter and a temperature of 10^6 K in the low corona, so a numerical application of the ideal gas law yields $p_0 = 0.003$ Pa. From the equation (1.6), one can derive the pressure of the solar corona at the infinite: $p(\infty) \simeq 1.5 \times 10^{-7}$ Pa.

On the other hand, one can estimate the pressure of the local interstellar medium (LISM) by assuming an ideal gas, a density of 1 atom per cubic centimetre and a temperature of 10,000 K (slightly above the real values). One obtains a pressure of 1.4×10^{-13} Pa. Despite of this overestimation, the pressure in the local interstellar medium is largely below the pressure of the corona at infinite: $p_{LISM} \ll p(\infty)$. One can deduce that the static corona can not be in equilibrium with the local interstellar medium and that the hydrostatic model is not valid[2].

[2]For the general case where the temperature profile is not known, one can show that the pressure at great distances will be null ($p(\infty) = 0$) only if the temperature decreases faster than 1/r (Parker, 1963).

The Parker model

Based on this conclusion, Parker (1958) developed a model to describe the plasma motion. We will consider the stationary case with a spherical geometry where the plasma is only subject to the pressure gradient and the solar gravity (the Lorentz force is neglected). First we will assume that the Sun does not have any rotation. So we can write the conservation of mass and momentum as:

$$\frac{1}{r^2}\frac{d}{dr}(\rho v) = 0 \tag{1.7}$$

$$\rho v \frac{dv}{dr} = -\frac{dp}{dr} - \frac{GM_\odot \rho}{r^2} \tag{1.8}$$

where v is the radial velocity. With $\rho \simeq m_p\, n$ and the equation 1.7, we deduce that $r^2 n v = const$, and after taking the logarithmic derivative:

$$2\frac{dr}{r} + \frac{dn}{n} + \frac{dv}{v} = 0 \tag{1.9}$$

As previously shown, the total pressure is $p = 2\, n\, k_B\, T \simeq 2\, \rho\, k_B\, T\, /\, m_p$. We assume a isothermal corona ($T = T_0$) and we will justify later this assumption. In these conditions, the sound speed in the corona is equal to:

$$c_s = \sqrt{\frac{dp}{d\rho}} \simeq \sqrt{\frac{2\, k_B\, T_0}{m_p}} \tag{1.10}$$

With $T_0 = 3 \times 10^6$ K, the numerical application gives $c_s \simeq 260$ km/s. So the escape velocity ($v_\infty \simeq 620$ km/s) is greater than the sound speed which is itself greater than the thermal speed. These orders of magnitude suggest that the acceleration of the solar wind can not happen near the surface of the Sun. By substituting the relations (1.9) and (1.10) into the momentum equation (1.8), we obtain:

$$v\frac{dv}{dr} = c_s^2 \left(\frac{2}{r} + \frac{1}{v}\frac{dv}{dr}\right) - \frac{G\, M_\odot}{r^2}$$

which can be re-arranged into:

$$\left(\left(\frac{v}{c_s}\right)^2 - 1\right)\frac{dv}{v} = 2\left(1 - \frac{G\, M_\odot}{2\, c_s^2\, r}\right)\frac{dr}{r}$$

We introduce the Mach number, $M = v/c_s$, and the critical point $r_c = GM_\odot/2c_s^2$. This differential equation can be written as:

$$\frac{dv}{dr} = \frac{2\, v}{r}\,\frac{1 - r_c/r}{M^2 - 1} \tag{1.11}$$

In order to obtain a continuous acceleration ($dv/dr > 0$), the flow must be subsonic ($M < 1$) for $r < r_c$, and it must be supersonic ($M > 1$) for $r > r_c$. A

numerical application gives $r_c \simeq 2 \times 10^6$ km, which is located in the corona and well above the photosphere. Moreover the temperature profile previously obtained by the equation 1.5 gives: $T(r_c) = (R_\odot/r_c)^{2/7}\, T_0 \simeq 0.5\, T_0$, so the assumption of isothermal conditions seems a posteriori pretty reasonable. This differential equation can be integrated and yields the following profile for the velocity:

$$\left(\frac{v}{c_s}\right)^2 - ln\left(\frac{v}{c_s}\right)^2 = 4\left(ln\left(\frac{r}{r_c}\right) + \frac{r_c}{r}\right) + C$$

Figure 1.2.3 shows this profile derived by Parker (1958) for varying coronal temperatures. For $r \gg r_c$, the flow is supersonic ($v > c_s$). Moreover we can easily show that $x^2 - ln(x)^2 \simeq x^2$ for $x \geq 1$. Then we can deduce that, for great distances (at the orbit of the Earth and beyond), the velocity profile has an asymptotic branch ($v \propto \sqrt{ln\, r}$). At 100 AU, we have $v \simeq 1.24\, v_E$, where v_E is the velocity of the solar wind near the Earth. So the Parker model yields a solar wind that can be considered to have a uniform velocity in the Solar system.

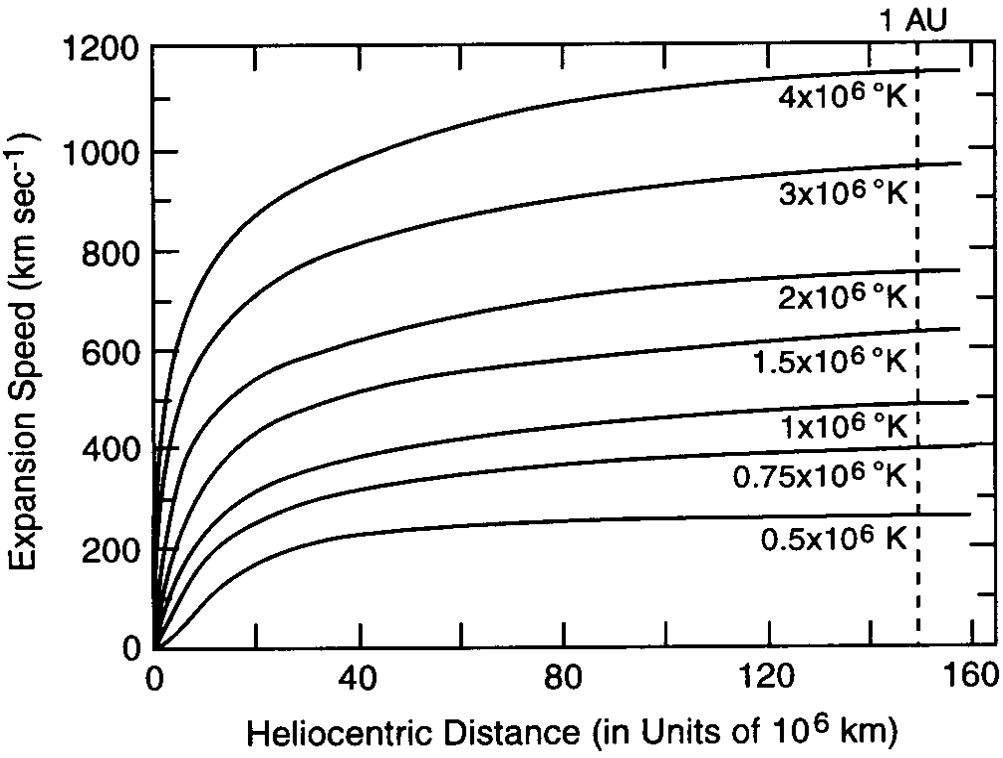

Figure 1.9: Theoretically derived speed of the solar wind from an isothermal model for varying coronal temperatures. Results from Parker (1958) adapted by Russell (2001).

Limitations of the Parker model

The Parker model is an *ad hoc* model that describes relatively well the velocity profile of the solar wind. However it does not explain the heating mechanism in the corona, neither can it explain the disparities of the solar wind.

Observations showed that the ecliptic is dominated by the slow wind with a speed of 400 km/s and a density of about 5 electrons and ions per cube centimetre near the Earth (Russell, 2001). But the situation is different for higher ecliptic latitudes, the Sun emits a fast wind (about 750 km/s). One has to deposit additional momentum in the flow to get these greater velocities. This can be achieved with Alfvén waves, which are observed to come from the corona (Marsch, 1998), or solar microflares. However this explanation is not satisfying either because it is not yet understood how these perturbations could provide the right energy in the right place to accelerate the wind.

Considering the energies involved in the low corona (Meyer-Vernet, 1999), one realizes that the gravitational binding energy (about 2×10^{11} J kg^{-1}) is barely compensated by the heat flux with a coronal temperature of 2×10^6 K, so the kinetic energy of the flow must come from the enthalpy. Indeed the model is very sensitive to the temperature, because the thermal conductivity varies as $T^{5/2}$, so a decrease of 15% in temperature prevents the creation of the solar wind.

The model of fast solar wind

Another flaw of the Parker model lies in use of the hydrodynamic equations that require a closure equation to introduce an *ad hoc* addition of heat and/or momentum. While it can be justified in the low corona, this approximation is not true everywhere. In the exobase (where the particles are about to escape, at several solar radii), the mean-free path is greater than the scale height, so the plasma is collision-less and the classical expression for the heat flux ($Q = -\kappa \nabla T$) is not longer valid.

Meyer-Vernet (1999) proposed a kinetic approach to explain the solar wind ejection, emphasizing the role of the electrostatic field which is implicit in the fluid point of view. In a static ionized atmosphere, the electrons tend to be displaced outwards with respect to the protons, because of their lower mass. The corresponding space charge induced a radial electrostatic field directed outwards. In an expanding collision-less medium as the exobase of the corona, this electrostatic field is much larger to compensate the larger thermal velocity of the electrons. Therefore the corresponding electric field pushes the protons outwards, producing a wind.

With a Maxwell distribution, such a model yields a velocity of about 250 km s^{-1} with an exobase located at 6 $R_\odot$ and a moderate temperature of 10^6 K. So this approach is clearly less sensitive to the temperature. However the Maxwell distribution is not adequate because the medium is collision-less and the non-equilibrium processes (e.g. turbulent waves in the solar atmosphere) create energetic electrons. A more rigorous approach requires the use of the kappa distribution, which is a generalization of the Maxwell distribution with a supra-thermal tail. A small supra-thermal tail can drastically increase the electrostatic potential, yielding a velocity of

about 700 km s^{-1}. From this point of view, the fast solar wind becomes the normal and stable wind, while the slow component is transient.

Somehow this model seems to fit better the observations, however the kinetic collision-less description is not fully satisfying because the mean-free path in the solar wind is of the same order of magnitude as the scale height, so not large enough to neglect collisions. A complete solution require a kinetic model taking collisions into account. Moreover the heating mechanisms of the corona still remains a full mystery for space scientists.

1.2.4 The heliosphere

The word heliosphere had been initially coined by Dessler (1967). It is defined as the region of interplanetary space where the solar wind is flowing supersonically. At some heliocentric distance, the solar wind pressure is balanced by the pressure of the interstellar medium, and the solar wind will undergo a shock transition to subsonic flow. This section reviews the different physical processes that operate inside the heliosphere.

Rotation of the Sun

As shown previously, one can consider that the solar wind has a uniform radial velocity almost everywhere in the Solar system ($v_r = v_0$). The pattern of the velocity is complicated by the rotation of the Sun. The Sun has an average rotation of 25.4 days, so an angular rate $\omega = 2.7 \times 10^{-6}$ rad/s. The axis of rotation is nearly aligned with the ecliptic north, so we will consider that the solar equator belongs to the ecliptic plane.

The effect of this rotation is analogous to the streams of water spiralling out from a rotating water sprinkler. As successive parcels of fluid move outward, the source moves because of rotation and the actual trace of fluid parcels takes the shape of a spiral (Fig. 1.2.4).

The shapes of these spiral lines can be expressed mathematically: in the frame of reference rotating with the sun, the plasma still moves outward in the radial direction. In the true stationary frame, there is an apparent component in the direction of solar longitude φ, because of the transformation between coordinates:

$$v_\varphi = \omega \, (r - R_\odot) \, sin \, \theta$$

where θ is the inclination (or polar angle) of the spherical coordinate system. We will then restrict ourselves to the ecliptic plane, which brings a simplification with $sin \, \pi/2 = 1$. One can show that the velocity field lines are described by a differential equation (Parker, 1958), whose solution is the spiral of Archimedes:

$$r = \frac{u}{\omega} \varphi + const$$

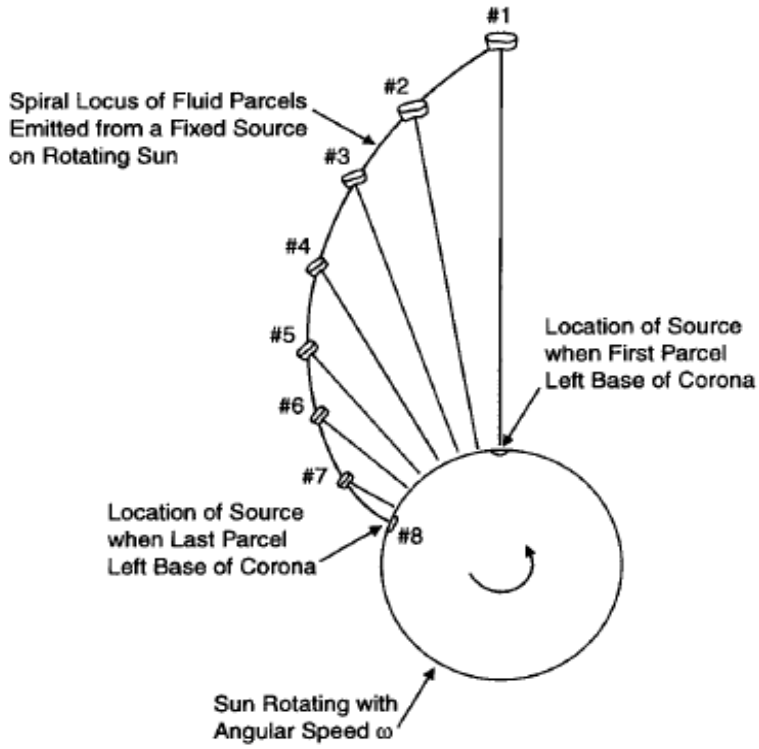

Figure 1.10: The creation of a spiral pattern because of the rotation of the Sun. Figure from Russell (2001).

The interplanetary magnetic field

According the Gauss's law for magnetism, the magnetic field is divergence-free ($\nabla \cdot \mathbf{B} = 0$). If we assume that all components of the magnetic field depend only on the distance r, the divergence in spherical coordinates gets relatively simple:

$$\nabla \cdot \mathbf{B} = \frac{1}{r^2}\frac{\partial(r^2 B_r)}{\partial r} = 0$$

So one finds the radial component of the magnetic field decreases with the square of the distance:

$$B_r = B_0 \left(\frac{R_\odot}{r}\right)^2$$

where B_0 is the magnetic field at the surface of the Sun. Observations show that the corona is a highly-ionized medium, so extremely conductive. This is why we can assume that the conductivity is infinite ($\sigma = \infty$). Therefore we can use the results explained in the section A.4.3 and consider that the magnetic field is frozen in the solar wind. At the first order, we can consider that the magnetic field lines near the Sun are perpendicular to the surface, as the streamlines. The magnetic field being

frozen in the plasma, one can conclude that they are parallel everywhere and deduce the longitudinal component of the magnetic field:

$$B_\varphi = \frac{v_\varphi}{v_r} B_r = B_0 \frac{\omega(r - R_\odot) R_\odot^2}{v_0 r^2}$$

So the longitudinal component of the magnetic field decreases as the inverse of the distance, but slower than the radial component that decreases as the inverse of the square of the distance. Near the Earth, $v_r \simeq v_\varphi \simeq 400$ km/s, and $B_r \simeq B_\varphi \simeq 5$ nT, so that the average radial and longitudinal components of both fields are nearly equal, and the field lines form an angle of about 45^o with the Sun-Earth axis.

Radiation pressure in the heliosphere

One should also take into account the radiation pressure from the Sun. Because the light emitted by the Sun is mainly due to black-body radiation, one can estimate the total flux of energy with Stefan's law ($F = \sigma T^4$ with $\sigma = 5.67 \times 10^{-8}$ J m^{-2} K^{-4} s^{-1}), so one obtains: $F \simeq 6 \times 10^7$ J s^{-1} m^{-2}, which yields a luminosity $L \simeq 3 \times 10^{25}$ J s^{-1} after integration over the whole surface of the Sun. Dividing the flux by the light speed, one gets an estimation of the radiation pressure at the surface of the Sun: $p_{rad} \simeq 0.2$ Pa. Because of the conservation of the flux, the radiation pressure decreases as $1/\mathrm{r}^2$ and is significantly lower at the orbit of the Earth: about 5×10^{-6} Pa.

Integrated over the disk of the Earth, the radiation pressure represents a force of about 10^9 N, which is thirteen orders of magnitude lower than the gravitational force exerted by the Sun on the Earth (about 4×10^{22} N). As one could have suspected, the radiation pressure is not going to push the Earth out of the Solar system, however it is still greater than the dynamical pressure of the solar wind by three orders of magnitude (see table 1.2).

As explained by Meyer-Vernet (1999), the charged particles interact much more strongly with each other than with light. Indeed their cross section for light scattering is the Thomson cross section, about the square of the classical electron radius ($r_e = e^2/4\pi\epsilon_0 m_e c^2$). In contrast, the mutual interaction of charged particles is governed by the Coulomb potential, so that two particles of charge e interact strongly when they are closer than the distance r_C for which the Coulomb energy $e^2/4\pi\epsilon_0 r_C$ is of the order of their kinetic energy $k_B T$. This approximation yields $r_C \simeq e^2/4\pi\epsilon_0 k_B T$. Therefore the cross section for Coulomb interaction is greater than the Thomson cross section by about $(r_C/r_e)^2 \simeq (m_e c^2/k_B T)^2$, so more than nine orders of magnitude within the heliosphere.

The pressure radiation does not have any significant impact on the charged particles of the solar wind, but we will see later in this chapter that the Ly-α resonance line has some consequences for the hydrogen atoms inside the heliosphere.

The cosmic rays

Indeed the concept of heliosphere has been previously introduced by Davis (1955) who considered the idea of a cavity produced by the solar corpuscular emission (i.e. the solar wind). He showed that such a cavity could trap cosmic rays of energy less than 100 GeV for a period long compared to a sunspot cycle.

Inside the heliosphere, two forms of cosmic rays are distinguished: the galactic cosmic rays (AGR) and the anomalous (ACR).

Cosmic rays are coupled to background flow via scattering by plasma waves. The net effect is that the cosmic rays tend to be convected along with the background plasma as they diffuse through the magnetic irregularities carried by the background plasma. Both galactic and anomalous cosmic rays can be treated as populations with negligible mass density but non-negligible energy density (Izmodenov, 2004).

1.3 Plasma models and structure of the heliospheric interface

1.3.1 Orders of magnitude

Plasma parameters

We can easily estimate the orders of magnitude of the different pressures that oppose to each other. The interstellar medium has an ionized component that forms a magnetized plasma like the solar wind, so both mediums contains some magnetic pressure in addition of the thermal and dynamic pressures. Moreover the local interstellar medium carry neutral atoms, mainly hydrogen, that will bring their own contribution to the dynamic and thermal pressures. Gas parameters of both mediums (Kivelson & Russell, 1995) are summed up in table 1.1.

Region	Particles	n	v	T	B
SW at 1 AU	protons	6.6 cm^{-3}	450 km/s	1.2×10^5 K	7 nT
	electrons	7.1 cm^{-3}		1.4×10^5 K	
	He^{2+}	0.25 cm^{-3}		N/A	
LISM	H atoms	0.195 cm^{-3}	26.4 km/s	6,300 K	0.27 nT
	He atoms	0.015 cm^{-3}			
	protons	0.06 cm^{-3}			
	electrons	0.07 cm^{-3}			
	He^{+}	0.01 cm^{-3}			

Table 1.1: Plasma parameters of the solar wind (SW) at the orbit of the Earth (Kivelson & Russell, 1995, p.92), and of the local interstellar medium (LISM) near the heliosphere (Frisch et al., 2009).

Pressures

We know that, for great distances, the interplanetary magnetic field is dominated by its longitudinal component (B_φ) that decreases as the inverse of the distance, so the magnetic pressure ($p_{mag} = B^2/2\mu_0$) will decrease as the inverse of the square of the distance. Moreover the velocity can be considered as constant. The dynamic pressure ($p_{dyn} = \rho v^2$) will be then proportional to the density. Finally the thermal pressure can be estimated with the law of ideal gas, so $p = 2\,n\,k_B\,T$, to take into account both protons and electrons. The temperature is slowly decreasing, so almost constant. The thermal pressure can be also considered to be proportional to the density. Because of the conservation of the mass, the quantity r^2nv remains constant, so both thermal and dynamic pressure will decrease as the inverse of the square of the distance. All sources of pressure have a similar profile, so measurements near the Earth will give an estimation at greater distances.

The Mach number and the Alfven number are other proxies to evaluate the state of the plasma and give an equivalent information. They are defined by the ratio of the velocity over the thermal speed of sound ($c_s = \sqrt{dp/d\rho}$) and the Alfven speed ($v_A = B/\sqrt{\mu_0\rho}$), respectively. For an ideal and isothermal gas, we have $dp/d\rho = p/\rho$, so:

$$M^2 = \frac{v^2}{c_s^2} = \frac{p_{dyn}}{p}$$
$$M_A^2 = \frac{v^2}{v_A^2} = \frac{1}{2}\frac{p_{dyn}}{p_{mag}}$$

Table 1.2 gives the order of magnitudes for the different pressures [3] at the Earth orbit and in the local interstellar medium, as well as the Mach and Alfven numbers in both cases.

	p_{dyn} (nPa)	p_{mag} (nPa)	p_{th} (nPa)	M	M_A
Earth orbit	2.2	0.019	0.025	9.4	7.1
LISM	0.28×10^{-3}	0.03×10^{-3}	0.04×10^{-3}	2.6	3.1

Table 1.2: Pressures at the orbit of the Earth and in the local interstellar medium.

Obviously, the solar wind is dominated by its dynamical pressure that is greater by at least two orders of magnitude compared to the magnetic and thermal pressure. While the magnetic and thermal pressures are comparable at the orbit of the Earth, the thermal pressure decreases more rapidly and becomes even weaker further away: in addition of the decrease of the density as $1/r^2$, the temperature has its own decrease as $1/r^{2/7}$, resulting into a total decrease of the thermal pressure as about $1/r^{2.3}$.

The situation in the local interstellar medium is more complex: the dynamic pressure is dominating in the upwind direction but the thermal and magnetic pressures have relatively comparable values.

[3] The pascal is the unit of pressure in the International System of units: 1 Pa = 1 N m^{-2}.

Estimation of the shock location

Based on these values, we can estimate the location of the shock in the upwind direction, by calculating the distance for which the pressures of the solar wind and the interstellar medium are equal:

$$r_{shock} = r_{Earth} \times \sqrt{\frac{2.2 \times 10^{-3}}{0.35}} \simeq 80\, AU$$

This kind of estimation has been initially made by Axford et al. (1963) developed a model where the solar wind interacts with the galactic magnetic field, resulting into the formation of shock wave at a heliocentric distance of the order of 50 AU. This underestimation was due to the lack of accurate measurements on the solar wind and the interstellar medium. However the order of magnitude was correct and has been recently confirmed by the spacecraft *Voyager* 1 and 2 that crossed the terminal shock at a distance of 94 AU in 2004 and 84 AU in 2007, respectively.

1.3.2 The two-shock model

The termination shock

Parker (1961, 1963) derived the geometry of a shock transition for a steady supersonic stellar wind that meets the subsonic interstellar medium. This situation does not strictly apply to the Sun and its vicinity because the local interstellar medium (LISM) appears to be supersonic. However one can use the model to understand the formation of the termination shock.

Considering the orders of magnitude that have been previously estimated, one can legitimately assume that the thermal pressure of the LISM is well larger than the thermal pressure of the solar wind ($p_2 \gg p_1$), so the Rankine-Hugoniot relations are reduced and we obtain simple relations for the density and the velocity. From them, we can also deduce the pressure:

$$v_2 = v_1 \frac{\gamma_{SW} - 1}{\gamma_{SW} + 1} \qquad \rho_2 = \rho_1 \frac{\gamma_{SW} + 1}{\gamma_{SW} - 1} \qquad p_2 = \frac{2}{\gamma_{SW} + 1} \rho_1\, v_1^2$$

Where the subscripts 1 and 2 denote the value just inside (ahead) and outside (beyond) the shock transition. One can apply the Bernoulli relation to relate the pressure just beyond the shock transition (p_2) with the pressure of the local interstellar medium (π_i). Combining with the state equation of the gas ($p/\rho^\gamma = const$) and the Rankine-Hugoniot relations, Parker (1961, 1963) derived the following analytical expression:

$$p_2 = \pi_i \left[1 + \frac{(\Delta - 1)(\beta - 1)}{4\,\beta} \right]^{\frac{\beta - 1}{\beta}}$$

Where Δ and β are the ratios of specific heats for the transition and beyond the shock, respectively. Assuming a value of 5/3, this expression yields $p_2 = 0.85\,\pi_i$,

which justifies the assumption $p_2 \gg p_1$. Using the fact that the density decreases as $1/r^2$, one obtains an estimation of the shock radius:

$$R \simeq 0.93 \sqrt{\frac{\rho_E \, v_{SW}^2}{\pi_i}} \, r_E \simeq 74\text{AU}$$

which is an order of magnitude comparable to the previous estimation. Assuming that both the solar wind and the interstellar flow are incompressible, Parker (1961, 1963) derived a differential equation describing the streamlines which are represented in figure 1.3.2.

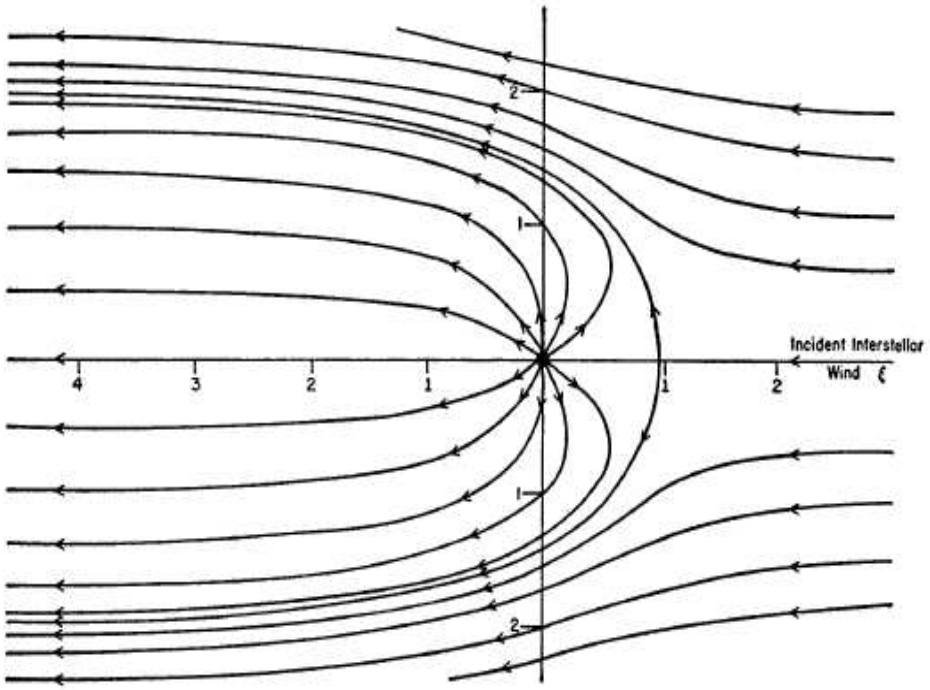

Figure 1.11: The streamlines of the subsonic, nearly incompressible, hydrodynamic flow of a stellar wind beyond the termination shock in the presence of a subsonic interstellar wind carrying no significant magnetic field. Distance is measured in units of the stagnation distance. From Parker (1961).

The bow shock

Led by Baranov et al. (1971, 1976, 1979, 1981), the Moscow group developed a model where the interstellar medium is supersonic, leading to the creation of another shock located outside the heliosphere: *the bow shock*.

Baranov et al. (1971) built a model using the hydrodynamic equations, based on several assumptions. First, Coulomb collision predominate in the interstellar gas that can be considered as collisional fluid. Secondly, the ions of the solar wind may be considered as probe ions moving in the field of charged particles of the interstellar medium: they almost completely lose directed momentum and transfer it to the electrons of the interstellar plasma over distances of the order of 1 AU. The electrons, in turn, exert a drag on the ions of the interstellar medium. Moreover stream instability may appear and result into a scattering of the charged particles. These processes provide effective collision mechanisms and justify the hydrodynamic description.

In this early model, Baranov et al. (1971) considered a simple geometry and assumed that the distance between two shocks is small compared with the distance from the Sun, as shown in Figure 1.12. They computed the form of the discontinuity from the impulse conservation law in directions normal and tangent to the gas layer (Busemann's method).

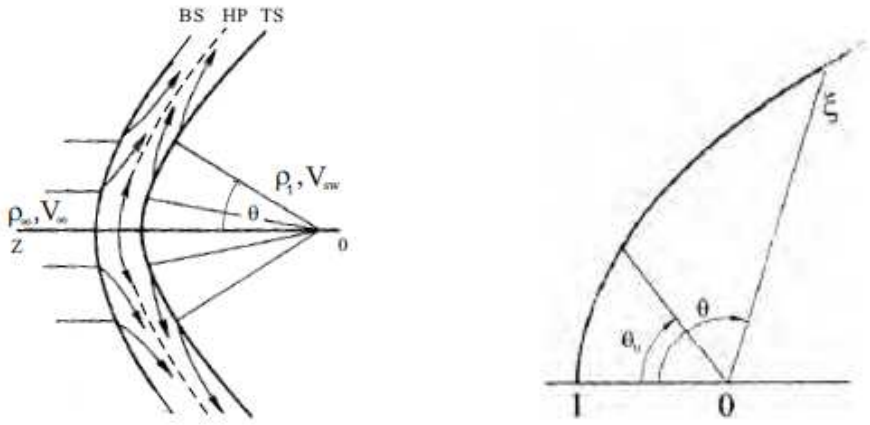

Figure 1.12: *Left:* Qualitative figure of the solar wind interaction with the supersonic fully ionized interstellar wind. The Sun is at the point O, and ρ_1 is the solar wind mass density at the termination shock (TS). *Right:* The form and location of the heliosheath (the region between BS and TS) calculated numerically by Baranov et al. (1971) in the approximation of the infinitesimal thickness. Here θ is the polar angle, $\theta_0 \approx 53°$ is the angle between the apex direction ($\theta = 0$) and the ecliptic plane, $\xi = r/r_0$ is the dimensionless heliocentric distance. Figures from Baranov et al. (1971) adapted by Baranov (2006b).

Baranov et al. (1976) extended this method and took into account the thickness of the region between the bow shock and the terminal shock. Based on these approximations, Baranov et al. (1979) developed a time-dependent finite-difference method to resolve Euler's hydrodynamic equations and calculate the flow structure

between shocks. Baranov et al. (1981) showed that the Mach number in the LISM strongly affects the interstellar flow pattern around the heliosphere and the position of the bow shock, but barely influences the position of the terminal shock within the heliosphere.

The heliopause

The heliopause is considered to be a free boundary surface that separates the solar wind plasma from the ionized component of the local interstellar medium (LISM). The boundary is geometrically determined by a pressure equilibrium across the surface.

1.3.3 Distortion by the interstellar magnetic field

The Newtonian approximation

Fahr et al. (1986, 1988) developed the first MHD model of the heliopause (HP) taking into account the interstellar magnetic field for any orientation. Pressures on both sides of the HP can be described by the Newtonian approximation (NA). For this purpose, the unperturbed full MHD stress tensors of the two plasma flows are projected onto the normal to the surface, and yield a quadratic partial differential equation in the general 3-dimensional case.

The effects of the interplanetary magnetic field are neglected since the magnetic pressure is negligible. If solar wind asymmetries are neglected too, the plane containing the LISM velocity vector and the interstellar magnetic field vector ($\{\overrightarrow{V}_{IS}, \overrightarrow{B}_{IS}\}$) becomes a main symmetry plane of the heliopause. Deriving the point of the maximal total pressure, Fahr et al. (1988) found a symmetry axis contained in the plane $\{\overrightarrow{V}_{IS}, \overrightarrow{B}_{IS}\}$ and deviating from the upwind direction by an angle:

$$\theta_0 = \frac{1}{2} atan\left(\frac{-sin(2\psi_0)}{M_A^2 - cos(2\psi_0)}\right)$$

where M_A is the Alfven number in the interstellar medium and ψ_0 the angle between the LISM velocity vector and the interstellar magnetic field vector. The presence of a magnetic field in the interstellar medium induces a tilt in the orientation of the heliopause.

MHD computational analysis

Ratkiewicz et al. (1998) made a fully three-dimensional MHD computational analysis of this problem. They calculated the shape and structure of the heliospheric boundary region for different interstellar Alfvénic Mach numbers and various angles between the interstellar wind and magnetic field vectors.

As shown in Figure 1.13,their results show the asymmetry of the heliospheric interface for inclination angles $0° < \alpha < 90°$, confirming the results of Fahr et al. (1986, 1988). MHD models can also include the hydrogen neutral as explained in the following section.

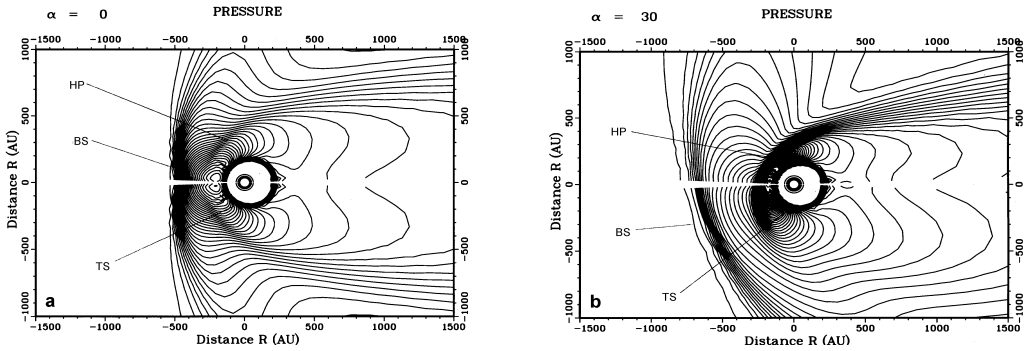

Figure 1.13: Shape of the heliospheric boundary region as shown by thermal pressure contour plots for inclination angle α equal to 0° (left) and 30° (right). Position of termination (TS), heliopause (HP) and bow shock (BS) are displayed. Figures from Ratkiewicz et al. (1998).

Crossing of the termination shock by Voyager

On 16 December 2004, Voyager 1 crossed the termination shock (TS) in the northern hemisphere at a distance of 94.01 AU from the Sun, becoming the first spacecraft to begin exploring the heliosheath. On 30 August 2007, it was the turn of Voyager 2 to cross the TS, but in the southern hemisphere and a a distance of 83.7 AU from the Sun, so about 10 AU closer to the Sun than Voyager 1 (Stone et al., 2005, 2008).

From this asymmetry, Ratkiewicz & Grygorczuk (2008) deduced that the local interstellar magnetic field has an inclination of about 30° from interstellar flow and a strength about 3.8 μG (0.38 nT). The next section describes the interplanetary hydrogen, including other detections of the local interstellar magnetic field.

1.4 The interplanetary hydrogen

1.4.1 Cold and hot models

Penetration of interstellar hydrogen atoms in the heliosphere

Considering the mean free path of solar protons, Blum & Fahr (1970) estimated the extent of the transition region to be about 50 AU and suggested that 90% of the interstellar hydrogen atoms coming from the upwind direction should penetrate the shock front and enter the heliosphere. Assuming a cold population of interstellar hydrogen atoms ($T \simeq 100$ K), these authors described the interaction processes of interstellar neutrals and modelled the interplanetary hydrogen distribution .

The primary cold interstellar neutrals enter the solar system along Kepler-hyperbolas and have loss processes: charge exchange with solar wind protons and photo-ionization by extreme ultra-violet (EUV) radiation. The probability dE that a particle becomes ionized or lost by charge exchange or photo-ionization is given by:

$$dE = \frac{ds}{v}(q_{ex}\, v_{rel}\, n_p + q_{EUV}\, f)$$

where v is the velocity of the particle, v_{rel} is the relative velocity between solar wins protons and incoming neutrals, n_p is the proton density, f is the EUV-flux, q_{ex} and q_{EUV} are the charge-exchange and ionization cross-sections, respectively. In this model, the solar wind is assumed to have a velocity of 400 km/s and a proton density of 5 cm^{-3} at Earth's orbit. The numerical values for q_{ex} and q_{EUV} are 10^{15} cm^{-2} and 8×10^{-18} cm^{-2}, respectively.

The ionization probability depends strongly on the solar EUV-flux: the depth of penetration shows a variation between 1 and 6 AU for a variation of the EUV-flux between 0.9 and 3.5 erg/cm^2/s. This model shows that the density of interstellar neutrals in the surroundings of the Sun is very sensitive to the solar parameters.

The presence of an interstellar wind was confirmed shortly after this prediction (e.g. Bertaux and Blamont, 1971). However this model overestimates the amount of interstellar hydrogen atoms penetrating the heliosphere because it does not take into account the plasma-gas interactions in the heliospheric interface.

A simplified model: the maximum emissivity region

As explained previously, OGO-R observations showed the existence of a maximum emissivity region Bertaux and Blamont (1971). One can explain the location of the maximum emissivity region (MER) with a simple model of hydrogen distribution. On one hand, we have an interstellar flow of hydrogen that can be considered to come from an infinite distance with a density n_∞ and a velocity v_∞. On the other hand some hydrogen atoms are lost because of ionization processes (EUV solar fluxes, electron impact or charge exchange with solar wind protons), that can be modelled as spherically symmetric with respect to the Sun:

$$\beta = \beta_E \left(\frac{r_E}{r}\right)^2$$

where β_E is the ionization rate at the location of the Earth($r_E = 1$ AU). Considering the steady state, one can assume the equilibrium between gain and loss processes. Being at the distance r from the Sun, if we note $n(r)$ the density of particles, then a volume element $d\tau$ contains $n(r)\, d\tau$ particles. During the interval $dt = dr/v_\infty$, this volume element receives $n(r + dr)\, d\tau$ atoms from the adjacent volume element located upstream, but gives $n(r)\, d\tau$ atoms to the adjacent volume element located downstream, so a net gain of $dn \times d\tau$ where $dn = n(r + dr) - n(r)$. Meanwhile there is a loss of $\beta\, dt \times n\, d\tau$ atoms due to ionization. At the equilibrium, the gain term is equal to the loss term:

$$dn = \frac{\beta_E\, r_E^2}{v_\infty}\, \frac{n}{r^2}\, dr$$

Where β_E and r_E are the ionization rate and the radial distance at Earth's orbit, respectively. This relation brings a differential equation that can be easily solved and yields:

$$n = n_\infty \exp\left(-\frac{L}{r}\right)$$

Where $L = \beta_E r_E^2 / v_\infty$. Considering that the intensity backscattered by the interplanetary hydrogen atoms depends on the hydrogen density and the solar flux (which decreases as $1/r^2$), one can assume that the local emission intensity is proportional to n/r^2. Hence we deduce that the maximum of emission is located at the distance:

$$r_{max} = \frac{L}{2} = \frac{\beta_E \, r_E^2}{2 \, v_\infty}$$

With an ionization rate of 6×10^{-7} s^{-1} at the Earth's orbit and interstellar velocity of 25 km s^{-1}, the numerical application yields $r_{max} = 2$ AU, so the same order of magnitude as the distance found by observations. The profiles of hydrogen density and backscattered intensity are plotted in figure 1.14.

Anisotropy and inhomogeneity of the temperature tensor

Considering the case where the action of solar gravity on hydrogen atoms is overcompensated by solar Lyman-alpha radiation pressure ($\mu > 1$), Fahr (1979) derived the temperature distribution of interstellar hydrogen and deuterium. As the hydrogen atoms coming from the upwind direction approach the Sun, the radial temperature increases but there is a decrease for the temperature components perpendicular to the bulk velocity. However, deuterium atoms show the opposite behaviour: the more the deuterium atoms are closer, the lower is the radial temperature but the higher is the perpendicular component of the temperature. Due to a larger mass, the deuterium atoms are subject to a net attractive solar field, despite the intensity of the Lyman-alpha radiation pressure.

By including a loss function to take into account the destructive effects of charge exchange and photoionization, Wu & Judge (1979) applied the Danby-Camm distribution formula [4] to the interplanetary gas moving through the solar system. Considering the case of a low radiation pressure ($\mu < 1$), they calculated the velocity distribution along solar radii for interplanetary hydrogen, and found that the radial temperature in the upwind direction decreases for the hydrogen atoms approach the Sun. This model converges with the work of Fahr for the deuterium atoms. Bzowski et al. (1997) confirmed these theoretical results by studying a more general case: for a low radiation pressure ($\mu < 1$), the anisotropy of the temperature tensor increases for smaller heliocentric distances.

[4] Danby & Camm (1957) studied the motion of a cloud of gas particles in the gravitational field of a point mass and found an analytical formula for the distribution function in terms of the phase space volume element.

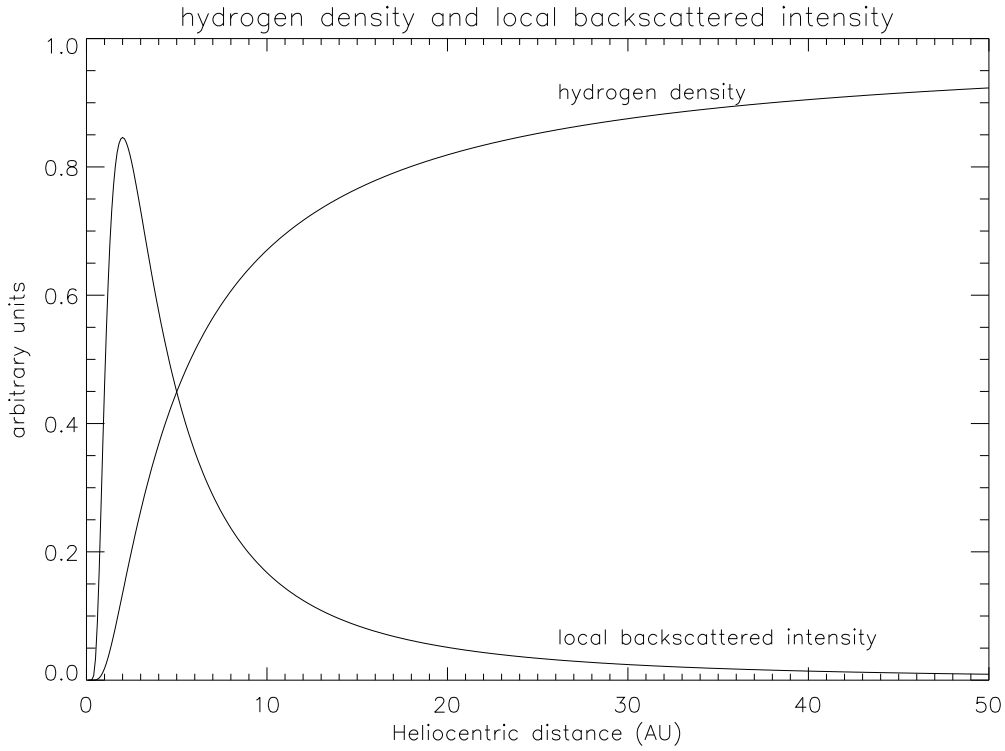

Figure 1.14: Simplified model of hydrogen distribution and backscattered intensity in the upwind direction, for an uniform interstellar flow. The local backscattered intensity is assumed to be proportional to both the density and the illumination flux.

There is also an asymmetry for the line of sight: the temperature of the velocity distribution integrated along the line of sight increases as the angle from the upwind increases. The apparent temperature is greater in the downwind direction, and this heating effect was confirmed by Prognoz 5/6 observations (Bertaux et al., 1985).

Atoms which survive best against ionization are those which go faster. This selection of faster atoms, as pointed out by Wu & Judge (1980), results into a narrowing of the velocity distribution (apparent cooling effect) and a displacement of the bulk velocity (apparent acceleration effect).

Hydrogen plateau

The Voyager (V1 and V2) and Pioneer 10 (P10) spacecraft are moving upstream and downstream into the local interstellar flow, monitoring Ly-α radiation resonantly scattered from heliospheric hydrogen with the Ultra-Violet Spectrometer (UVS).

Shemansky et al. (1984) developed a method independent of instrument calibration, by comparing the daily average variation of the 1216 Å line as measured by P10 and V2 with the directly measured solar emission line from the Solar Mesospheric Explorer (SME) satellite. They estimated the hydrogen density in the unperturbed

LISM and reported a difference between upstream and downstream densities.

Hall et al. (1993) showed that upstream intensities fall as $r^{-0.75\pm0.05}$ between 15 and 35 AU, so more slowly than downstream intensities that fall as $r^{-1.07\pm0.1}$. Between 15 and 20 AU, Voyager intensities fall as r^{-1}, whereas between 30 and 35 AU they fall as $r^{-0.35}$. This flattening trend implies that the upstream H density is increasingly rapidly with heliocentric distance beyond 25 AU. The model of Baranov and Malama (1993) predicted the existence of these hydrogen density gradients at a third to half the distance to the upstream termination shock.

Puyoo et al. (1997) developed a self-consistent method to simultaneously derive the abundance of interplanetary hydrogen and its rate of ionization by the solar environment. Using the principle of invariance and solar Ly-α activity, they showed that some properties of the interplanetary radiation field in the inner heliosphere depend uniquely on the ionization rate and the local density, so these properties can therefore be derived by a self-consistent technique. This approach allows to derive the hydrogen density within 30 AU from the Sun.

Quémerais et al. (2003) analysed the UVS/Voyager 1 Ly-α data obtained between 1993 and 2003. Their work showed that the radial variation of the intensities measured close to the upwind direction has changed abruptly at the end of 1997 when the spacecraft was at a distance larger than 70 AU from the Sun: the coefficient α of the power law describing the intensity as a function of solar distance has changed from a value of -1.58 ± 0.02 between 1993 and 1997 to a value of -0.22 ± 0.07 after 1998. The value of α found here between 50 and 65 AU shows a much steeper gradient than the one reported by Hall et al. (1993). The discrepancy may be due the use of a different database to correct the Ly-α solar flux (SME in the early 1990s and UARS/Solstice in the late 1990s).

1.4.2 Charge exchange in the heliospheric interface

Depletion of the interstellar hydrogen atoms

The main plasma-gas interaction is the resonant charge exchange process between protons and hydrogen atoms, with a cross section of $\sigma = 6 \times 10^{-15}$ cm^{-2} for a relative velocity of 15-30 km s^{-1}. Considering this process over the stagnation region between the heliosphere and the bow shock (the outer heliosheath), Wallis (1975) showed that the incoming population of hydrogen atoms could be depleted by a factor exceeding three.

While earlier work had suggested that the charge exchange region could contribute to the density of interplanetary hydrogen (Patterson et al., 1963), Wallis reached an opposite conclusion: that charge exchange processes impede the penetration of hydrogen atoms through the interstellar plasma into the solar system and reduce the local density of hydrogen.

Deceleration and heating of the interstellar hydrogen atoms

Ripken & Fahr (1983) used the kinetic theory to describe quantitatively the perturbing effects of the heliospheric interface on the interstellar neutrals. The Boltzmann integro-differential equation for the velocity distribution of hydrogen is integrated along the trajectories of hydrogen atoms approaching the inner solar system.

In the stationary case, the differential operator d/dt can be transformed into one which is differentiating the velocity distribution f with respect to the line element s measured on the specific dynamical trajectory of an H atom moving locally with the velocity v. This brings the following form of the Boltzmann equation:

$$\frac{\partial f}{\partial s}(\mathbf{r}, \mathbf{v}) = \frac{1}{v}[P(\mathbf{r}, \mathbf{v}) - L(\mathbf{r}, \mathbf{v})]$$

where the functions P and L describe the rates by which H-atoms at $\mathbf{r}$ are produced or removed, respectively, by charge exchange reactions. With assumptions to simplify the expression of the function P and L, Ripken & Fahr (1983) considered a subsonic or supersonic interface. An effect of this model consists of a density decrease by 50% in either case, confirming the previous results of Wallis (1975). Moreover it shows that hydrogen streaming suffers a heating of about 1,500 K and a deceleration of about 1 km s^{-1}.

Osterbart & Fahr (1992) proposed a more generalized approach to estimate a solution. They counted the particles appearing at $\mathbf{r}$ according to their collision hierarchies of orders j by introduction of the distribution f_j for particles that have resonantly exchanged their charge j-times somewhere in the interstellar or solar part of the interface region prior to arriving at the place $\mathbf{r}$. Then the Boltzmann equation splits into a hierarchical system of differential equations given in the following form:

$$\frac{\partial f_j}{\partial s} = \frac{1}{v}[P_{j-1} - f_j \cdot \nu_{ex}^{-}]$$

where the production term P_{j-1} is given by velocity-space-integral over the distribution function f_{j-1}, which is thus independent of f_j. Osterbart & Fahr (1992) derived a deceleration of about 2 km/s for the bulk velocity of the hydrogen distribution function.

The Hydrogen Wall

Baranov and Malama (1993) developed a self-consistent gas-dynamic model, combining a hydrodynamical treatment of the plasma-plasma interaction with a kinetic description of the neutrals. Indeed the mean free path of a hydrogen atom is comparable to the characteristic length of the problem, i.e. the size of the heliosphere in the present case. These authors used an iterative method, where the trajectories of hydrogen atoms are calculated by a Monte-Carlo scheme with splitting of the trajectories in the field of plasma gas-dynamics parameters.

The results of this model show an accumulation of hydrogen atoms between the bow shock and the heliopause. This effect is due to the creation of secondary hydrogen atoms with decreased velocity corresponding to that of the interstellar plasma compressed in the bow shock. This increase vanished for large deviations

of the line-of-sight relative to the upwind direction, and is completely absent in the wake region of the heliosphere (downwind direction). This prediction of a "Hydrogen Wall" was then confirmed with absorption measurements in the direction of Alpha-Centauri (Linsky and Wood, 1996).

1.4.3 Effects of solar activity

Oscillations of the heliospheric interface

Magnetohydrodynamical models showed that variations of the solar wind momentum influence the heliosheath structure. As for the stationary models, the hydrogen component requires a kinetic description (e.g., Izmodenov & Malama, 2004).

As shown in Figure 1.15, numerical simulations suggest the existence of an oscillation of the locations of the termination shock (TS), the heliopause (HP) and the bow shock (BS), with the solar cycle.

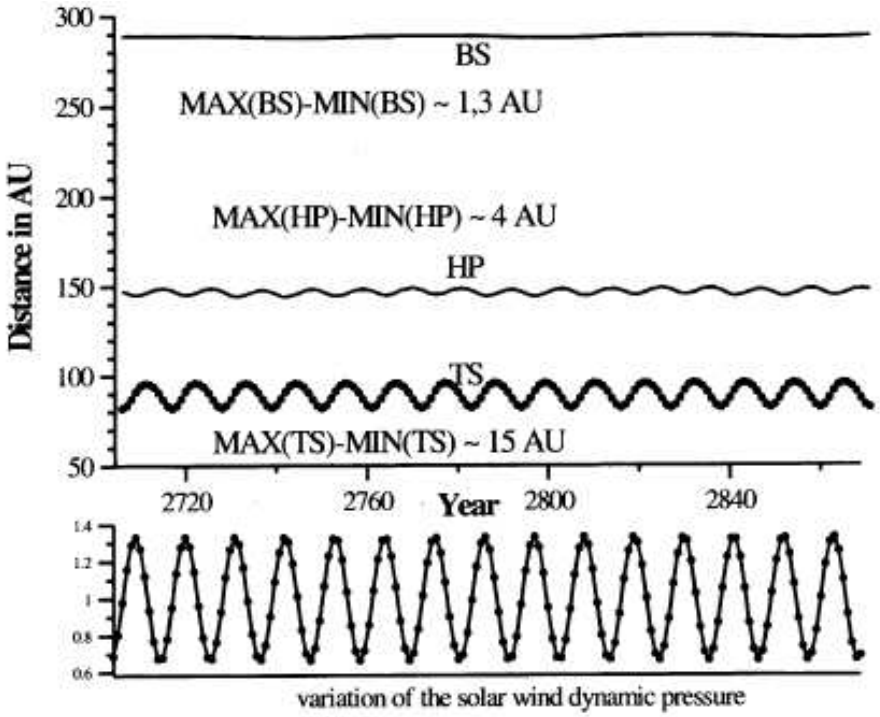

Figure 1.15: Upper panel: time variations of the locations of the termination shock, bow shock and the heliopause in the upwind direction. Low panel: variations of the solar wind momentum flux with time. Figures from Izmodenov & Malama (2004).

Experiment	Year of obs.	Reference	v_{IPH} (km s^{-1})
Mars 7	1973-74	Bertaux et al. (1976)	19.5 ± 1.5
Copernicus/U1	1975	Adams and Frisch (1977)	22.1 ± 2.8
PROGNOZ 5 & 6	1976-77	Bertaux et al. (1985)	20 ± 1
IUE/SWP	1983	Clarke et al. (1984, 1995)	18 ± 5
HST/GHRS	1994	Clarke et al. (1998)	18 ± 2
		Scherer et al. (1999)	20.7
		Ben-Jaffel et al. (2000)	22.9
	1995	Clarke et al. (1998)	21 ± 2
		Scherer et al. (1999)	24.3
		Ben-Jaffel et al. (2000)	23.3
SOHO/SWAN	1997	Quémerais et al. (2006)	25.7 ± 0.2
	1998		25.3 ± 0.2
	2000		22.5 ± 0.5
	2001		21.5 ± 1.2
	2002		21.5 ± 0.3
	2003		21.4 ± 0.5
HST/STIS	2001	Quémerais et al. (2006)	20.3 ± 0.2

Table 1.3: Measured values of the incoming IPH velocity from backscattered solar Ly-α emission.

Variations of the IPH bulk velocity

During the last two decades, SOHO/SWAN and the echelle modes of the Goddard High Resolution Spectrograph (GHRS) and Space Telescope Imaging Spectrograph (STIS) on the Hubble Space Telescope (HST) have been used to measure the Ly-α Doppler shift with respect to the heliospheric referential and line profile with greater precision than previous observations (Clarke et al., 1998; Scherer et al., 1999; Ben-Jaffel et al., 2000; Quémerais et al., 2006).

As shown in Table 2.1, IPH spectroscopic observations cover several decades, and while not uniformly spaced in time, they roughly span the entirety of solar cycle 23. Taken over time, the bulk velocity of IPH atoms (IPH velocity) displays variability with origins that could be either internal or external to the heliosphere.

Fahr et al. (1993) studied the consequences induced by changes in the LISM approaching the heliosphere, showing that periods of between 20 and 100 years may give noticeable imprints on the upwind/downwind velocity distribution. Unfortunately, the existing database of IPH velocity measurements lacks the precision to detect changes in time scales longer than 20-25 years.

The Warsaw group (Rucinski and Bzowski, 1995; Bzowski et al., 1997) developed a time-dependent hot model of the inner heliosphere that predicts a $\sim$ 5 km/s modulation in IPH bulk velocity due to solar cycle changes in radiation pressure and ionization rates. More recently, fluid-kinetic models included the effects of non-stationary solar wind ram pressure on the heliospheric interface (Izmodenov, 2004; Izmodenov et al., 2008; Pogorelov et al., 2010).

The use of a radiative transfer model allows more precise predictions of the interplanetary background line-shifts (Scherer et al., 1999; Quémerais et al., 2008). These models all converge toward a general finding that the IPH velocity should

vary by 3-4 km/s over the solar cycle, but they reach different conclusions about the rate of this change and its precise magnitude. Based on previously published values, none of them have been able to match the data consistently across the entire solar cycle (Quémerais et al., 2008).

Active regions of ultraviolet emission and wave damping within the helioshere

The solar ultraviolet emission is not spherically symmetric and contains localized active regions generally at low solar latitude, so the Sun's rotation induces 27-day intensity modulations in the scattering of solar Lyman-alpha radiation by heliospheric neutral hydrogen. A study of Cassini and Voyager data sets by Pryor et al. (2008) showed that these modulations are increasingly damped in amplitude at larger distances from the Sun due to multiple scattering in the heliosphere.

This work provides a diagnostic of the interplanetary neutral hydrogen density, independent of instrument calibration. Coupled with Baranov-Malama models of the heliospheric, it yields a hydrogen density of 0.085 or 0.095 cm^{-3} at the termination shock, depending on the interstellar value (0.15 or 0.18 cm^{-3}, respectively).

Solar wind anisotropies

The solar wind is also subject to anisotropies, that moreover vary with the solar cycle. Pryor et al. (2003) analysed data from the Ulysses spacecraft (plasma parameters with SWOOPS and Ly-α maps with GAS), providing hydrogen atom lifetimes in the three-dimensional heliosphere over the solar cycle.

At solar minimum, charge exchange is higher in the ecliptic, while high latitudes are dominated by less dense fast wind. Solar minima also caused the apparition of a groove of reduced Ly-α emission near the ecliptic plane, as a result of hydrogen depletion by the heliospheric current sheet. Charge exchange is more isotropic during solar maximum, when there is less fast wind and the heliospheric current sheet is tilted so there is slow wind at all latitudes.

1.4.4 Influence of the interstellar magnetic field

A possible Fermi effect in the interface

In this context, a first-order Fermi acceleration of Lyα photons should occur at the heliospheric interface (Ben-Jaffel et al., 2000). In this process, photons are Doppler-shifted toward shorter wavelengths each time they are scattered by hydrogen neutrals that have been decelerated by charge exchange with protons in the transition region wrapping the heliopause.

This additional Fermi emission appears in the data analysis of GHRS observations made by Ben-Jaffel et al. (2000) and could explain the excess in the Lyα sky brightness that was detected by *Voyager* deep in the inner heliosphere.

Deflection of the hydrogen

By contrast to the hydrogen neutrals, interstellar helium atoms are barely affected by the heliospheric interface because of a smaller cross-section for charge-exchange reactions, and carry the signature of the LISM inside the heliosphere (Moebius et al., 2004).

Observations with the Solar Wind ANisotropies (SWAN) instrument on the Solar Wind Heliospheric Observatory (SOHO) show that the hydrogen flow is slightly deflected by respect to the helium flow, confirming the obliquity of the interstellar magnetic field (Lallement et al., 2005, 2010).

Energetic neutral atoms

The Interstellar Boundary (IBEX) completed a full scan of the sky, creating maps of energetic neutral atoms (ENA) for energies between 100 eV and 6 keV. The data shows a striking ribbon feature of enhanced ENA emission, 2 or 3 times greater than the adjacent regions of the sky.

Heerikhuisen et al. (2010) proposed a scenario and made numerical simulations to explain the ribbon. Primary ENA created in the inner heliosheath (IHS) region between the TS and the HP move into the outer heliosheath (OHS) whereupon they charge-exchange and create pick-up ions (PUIs). These PUIs will initially form a ring-beam distribution, with a velocity component along the magnetic field.

Over time, this distribution will be isotropized by wave-particle interactions. However Heerikhuisen et al. (2010) showed that it is possible that the charge-exchange timescale to be shorter than the time for PUIs to diffuse from a ring-beam to a shell distribution. Hence the PUIs re-neutralize to form secondary ENAs with a ring-beam distribution, yielding a ribbon whose line-of-sight is perpendicular to the magnetic field.

1.4.5 Radiative transfer of Lyman-α photons

Radiative transfer is a general problem in astrophysics and it has been addressed in classical papers or textbooks (e.g., Hummer, 1962; Ivanov, 1973; Mihalas, 1978; Rybicki & Lightman, 1979). The specific problem of the interplanetary Ly-α background has been addressed by different authors (e.g., Hall, 1992; Quémerais , 2006).

Absorption profile, cross-section and mean free path

Considering the scattering of photons by a gas, the absorption profile of a resonance line is obtained by the convolution of the velocity distribution of the gas and a Lorentzian profile. The velocity distribution represents the Doppler broadening of the line due to the motion of atoms and depends mainly on the gas temperature. The Lorentzian profile results from the natural broadening which is due to Heisenberg's uncertainty principle and depends mainly on the transition probability.

In the particular case of a Maxwellian gas, the velocity distribution is a Gaussian profile and the absorption profile $\phi(\nu)$ can be written as a Voigt profile:

$$\phi(\nu) = \frac{1}{\Delta\nu_D \sqrt{\pi}} \frac{a}{\pi} \int_{-\infty}^{\infty} \frac{a^2}{a^2 + (u-y)^2} e^{-y^2} dy = \frac{H(a,u)}{\Delta\nu_D \sqrt{\pi}}$$

where $\Delta\nu_D$ is the Doppler width, u the normalized frequency and a the ratio of the natural width over the Doppler width:

$$\begin{aligned} \Delta\nu_D &= \frac{\nu_0}{c}\sqrt{\frac{2\,k_B\,T}{m}} \\ u &= \frac{\nu - \nu_0}{\Delta\nu_D} \\ a &= \frac{\Delta\nu_n}{\Delta\nu_D} = \frac{\Gamma}{4\pi\,\Delta\nu_D} \end{aligned}$$

where ν_0 is the transition frequency, c the light velocity, k_B the Boltzmann constant, T the gas temperature and m the hydrogen mass, and Γ the transition probability. For the Ly-α transition, $\Gamma = 6.265\times10^8\,\mathrm{s}^{-1}$, which yields $a = 5.27\times10^{-4}$ for a hydrogen gas at 8,000 K, so the absorption profile can be assumed to be Gaussian. Indeed a Voigt profile yields a Gaussian profile in the limit $a \to 0$:

$$\phi(\nu) = \frac{H(a,u)}{\Delta\nu_D\sqrt{\pi}} \to \frac{e^{-u^2}}{\Delta\nu_D\sqrt{\pi}} \qquad \text{when } a \to 0$$

The cross-section for absorption or scattering is proportional to the absorption profile:

$$\sigma(\nu) = \frac{1}{4\pi\varepsilon_0}\frac{\pi\,e^2}{m\,c}\,f_{12}\,\phi(\nu)$$

where f_{12} is the absorption oscillator strength and is equal to 0.4162 for the Ly-α transition. The cross-section at the line centre (ν_0) for a gas at temperature T is then given by:

$$\sigma_0 = 5.96 \times 10^{-12} \times \frac{1}{\sqrt{T}}\ \mathrm{cm}^2$$

One can deduce the mean free path of a Ly-α photon in the solar neighbourhood:

$$l = \frac{1}{n\,\sigma_0}$$

which is of the order of 10 AU for n=0.1 cm^{-3} and T=8,000 K.

Radiation pressure

Assuming an optically thin medium and a constant solar line profile, the force exerted by the radiation pressure on an hydrogen atom at 1 AU can be estimated by:

$$F_{rad} \approx \frac{h\,\nu_0}{c} \times (\pi F_{\lambda_0}) \times \sigma_0 \times \Delta\lambda_D$$

where (πF_{λ_0}) is the differential solar flux (photons per cm^2 per second per nm) at 1 AU and $\Delta\lambda_D \approx \Delta\nu_D \times \lambda_0^2/c \approx 0.005$ nm at T=8,000 K.

Hall (1992) made a more accurate calculation and showed that the radiation pressure compensates the gravitational force exerted by the Sun on a hydrogen atom for a differential flux $\pi F_{\lambda_0} = 3.37 \times 10^{12}$ photons per cm^2 per second per nm.

Scattering phase function

The scattering phase function expresses the relation between the direction of propagation of the photon before and after scattering. If we call θ the angle between the two directions, the phase function $\phi(\theta)$ gives the probability of having a scattering at angle θ. An isotropic scattering has a constant phase function equal to $1/4\pi$.

Brandt & Chamberlain (1959) have given the expression of the scattering phase function at Lyman-α, normalized over 4π steradians:

$$\phi(\theta) = \frac{11/12 + (1/4)\,cos^2\,\theta}{4\pi}$$

Frequency redistribution

The frequency redistribution function expresses the change in frequency of the photon during the scattering process. In the interplanetary medium, the time between two collisions is of the order of 10^{10} seconds, which is much larger than the lifetime of the electron in the excited state. So the velocity of the scattering atom does not change.

The *Angle Dependent Partial Frequency Redistribution* (ADPFR) expresses the conditional probability of frequency of the outgoing photon for a given frequency of incoming photon and a given scattering angle. The assumption of *coherent scattering* considers that the frequency of the photon is conserved during the scattering process.

The opposite assumption of *Complete Frequency Redistribution* (CFR) postulates that there is no correlation between the frequencies of the incoming and outgoing photon. The CFR applies if the time between two collisions is short before the Lyman-α de-excitation time, which is not the case in the interplanetary medium. However it has been used in the past to shorten the length of computing.

Quémerais et al. (2010) compared results of ADPFR and CFR models of the interplanetary hydrogen Lyman-α intensity background in the outer heliosphere with the scans performed by the *Voyager 1/2* UV spectrometer (UVS) instruments between 1993 and 2003. Both data and ADPFR model show an excess over the CFR

model in the upwind direction. This is due to the backscattering of solar photons by the slowed down hydrogen population trapped in the hydrogen wall. Because these photons are Doppler-shifted outside the absorption profile of the main flow, they are visible at a much larger distance than the usual 10 AU.

1.5 Summary

The interaction between the solar wind and the local interstellar medium (LISM) is a complex problem, which requires a time-dependent and three-dimensional treatment. The solar wind and the plasma component of the LISM can be described with a magneto-hydrodynamic approach, but the modelling of the hydrogen atoms needs the framework of kinetic theory because their mean free path is comparable with the size of the problem.

While the ionized components are deflected, the hydrogen neutrals can cross the heliopause and carry the signature of the interface because of charge-exchange reactions. In the inner heliosphere, the interplanetary hydrogen (IPH) is strongly affected by the Sun and backscatters the solar Ly-α photons that bring precious information to the observer. Observations over the last two decades showed that the IPH velocity has variations which are correlated to the solar activity.

Chapter 2

Analysis of the bulk velocity of the interplanetary hydrogen

2.1 Introduction

This chapter is an extended version of a work published by Vincent et al. (2011a). To make it self-contained, the introduction contains some redundancies with the previous chapter.

2.1.1 The heliospheric interface in a nutshell

The two-shock model

The Solar system is moving through the Local Interstellar Cloud, a diffuse warm and partially ionized medium, mainly composed of atomic hydrogen (Frisch, 2009). The fundamental aspect of the interaction between the solar wind (SW) and the local interstellar medium (LISM) is the dynamic equilibrium between two counter-flowing magnetized plasmas that meet and are separated along a tangential discontinuity, the heliopause (Parker, 1961; Baranov et al., 1971; Axford, 1972).

The overall shape and location of the heliopause is determined by the relative velocity of the solar wind and LISM and the plasma densities on either side of the barrier. In the generalized model of the interaction, the SW and the ionized LISM are decelerated to subsonic speeds through shocks that are respectively located inside (the termination shock) and outside (the bow shock) the heliopause, as shown in figure 2.1.

Penetration of the interstellar hydrogen

Because of a large mean free path, a fraction of interstellar hydrogen atoms penetrates inside the heliosphere without any interaction with the interface (Blum & Fahr, 1970), forming the primary population of the interplanetary hydrogen (IPH). Early space based studies of the sky background confirmed the presence of the incoming hydrogen flow and produced the first all-sky maps of backscattered solar

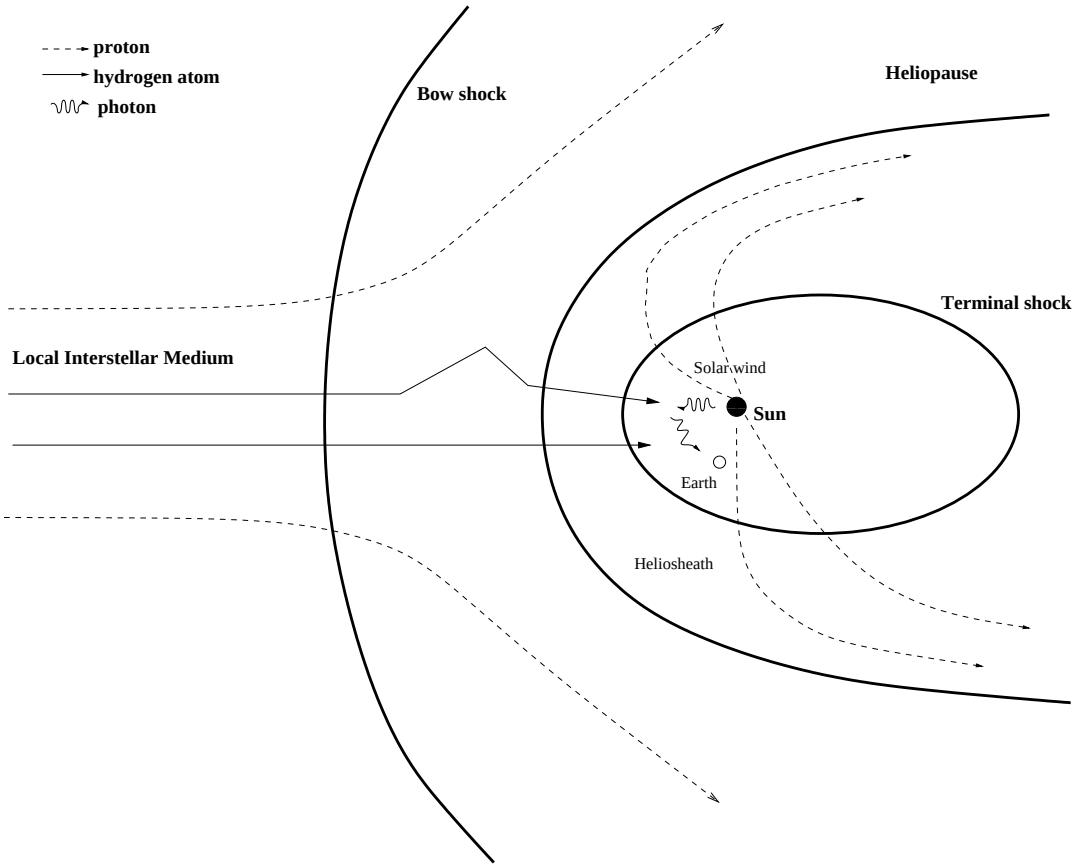

Figure 2.1: Schematic of the interaction between the solar wind and the local interstellar medium. The Earth position is not to scale.

Ly-α emission from the IPH (Bertaux and Blamont, 1971; Thomas and Krassa, 1971).

However these experiments did not resolve velocities in the Ly-α line. Subsequent UV spectroscopic and imaging experiments provided limited access to the IPH velocity distribution (Bertaux et al., 1976, 1985; Adams and Frisch, 1977; Clarke et al., 1984, 1995) and revealed a deceleration of the hydrogen flow relative to the LISM (Bertin et al., 1993; Clarke et al., 1998; Scherer et al., 1999; Ben-Jaffel et al., 2000; Quémerais et al., 2006).

2.1.2 Modification of the interstellar hydrogen flow

Deceleration of the hydrogen neutrals

The observed neutral LISM deceleration is believed to be traceable to the fraction of interstellar hydrogen atoms that interact with the slowing LISM protons through resonance charge exchange reactions (Wallis, 1975; Ripken & Fahr, 1983). These reactions result in the formation of a secondary population with a slower bulk motion, leading to the formation of a "Hydrogen Wall" between the bow shock and the

heliopause, that was predicted by Baranov and Malama (1993) with Monte-Carlo simulations to describe the trajectories of hydrogen atoms, and then observed by Linsky and Wood (1996) with observations of absorption lines in the direction of α Centauri.

The Baranov-Malama model also predicts hydrogen density gradients in the upstream termination shock. Monitoring of upstream and downstream Ly-α intensities by the Voyager and Pioneer 10 spacecraft confirmed the presence of these gradients and the influence of the heliospheric interface on the IPH distribution (Hall et al., 1993).

Asymmetry of the spatial distribution of hydrogen neutrals

Observations of the Ly-α glow pattern by the Ultraviolet Spectrometers (UVS) aboard both *Voyager* 1 and 2 revealed an systematic excess of the intensity around the upwind direction (Quémerais et al., 1995).

The maximum of the brightness distribution shows an about 20° deviation from upwind and suggests the existence of the bow shock outside the heliosphere and the obliquity of the local interstellar magnetic field (LIMF; Ben-Jaffel et al., 2000).

Three-dimensional time-dependent magnetohydrodynamic model of the heliospheric interface with neutral particles confirmed that the inclination of the LIMF induced an asymmetry in the spatial distribution of hydrogen neutrals (Ratkiewicz and Ben-Jaffel, 2002; Ratkiewicz et al., 2007).

Deflection of the hydrogen flow

By contrast to the hydrogen neutrals, interstellar helium atoms are barely affected by the heliospheric interface because of a smaller cross-section for charge-exchange reactions, and carry the signature of the LISM inside the heliosphere (Moebius et al., 2004).

Observations with the Solar Wind ANisotropies (SWAN) instrument on the Solar Wind Heliospheric Observatory (SOHO) show that the hydrogen flow is slightly deflected with respect to the helium flow, confirming the obliquity of the interstellar magnetic field (Lallement et al., 2005, 2010).

2.1.3 Velocity variations of the interplanetary hydrogen

Survey of the Ly-α observations in the upwind direction

During the last two decades, SOHO/SWAN and the echelle modes of the Goddard High Resolution Spectrograph (GHRS) and Space Telescope Imaging Spectrograph (STIS) on the Hubble Space Telescope (HST) have been used to measure the Ly-α Doppler shift with respect to the heliospheric referential and line profile with greater precision than previous observations (Clarke et al., 1998; Scherer et al., 1999; Ben-Jaffel et al., 2000; Quémerais et al., 2006).

As shown in Table 2.1, IPH spectroscopic observations cover several decades, and while not uniformly spaced in time, they roughly span the entirety of solar cycle 23.

Experiment	Year of obs.	Reference	v_{IPH} (km s^{-1})
Mars 7	1973-74	Bertaux et al. (1976)	19.5 ± 1.5
Copernicus/U1	1975	Adams and Frisch (1977)	22.1 ± 2.8
PROGNOZ 5 & 6	1976-77	Bertaux et al. (1985)	20 ± 1
IUE/SWP	1983	Clarke et al. (1984, 1995)	18 ± 5
HST/GHRS	1994	Clarke et al. (1998)	18 ± 2
		Scherer et al. (1999)	20.7
		Ben-Jaffel et al. (2000)	22.9
	1995	Clarke et al. (1998)	21 ± 2
		Scherer et al. (1999)	24.3
		Ben-Jaffel et al. (2000)	23.3
SOHO/SWAN	1997	Quémerais et al. (2006)	25.7 ± 0.2
	1998		25.3 ± 0.2
	2000		22.5 ± 0.5
	2001		21.5 ± 1.2
	2002		21.5 ± 0.3
	2003		21.4 ± 0.5
HST/STIS	2001	Quémerais et al. (2006)	20.3 ± 0.2

Table 2.1: Measured values of the incoming IPH velocity from backscattered solar Ly-α emission.

Taken over time, the bulk velocity of IPH atoms (IPH velocity) displays variability with origins could be either internal or external to the heliosphere.

Fahr et al. (1993) studied the consequences induced by changes in the LISM approaching the heliosphere, showing that periods of between 20 and 100 years may give noticeable imprints on the upwind/downwind velocity distribution. Unfortunately, the existing database of IPH velocity measurements lacks the precision to detect changes in time scales longer than 20-25 years.

Numerical simulations: state of the art

Within the heliosphere, the IPH velocity is affected by several temporally dependent processes related to the solar wind and solar Ly-α intensity. Ionization and radiation pressure anisotropies, emphasized by Pryor et al. (2003, 2008), should also have an impact on the velocity distribution.

The Warsaw group (Rucinski and Bzowski, 1995; Bzowski et al., 1997) developed a time-dependent hot model of the inner heliosphere that predicts a $\sim$ 5 km/s modulation in IPH bulk velocity due to solar cycle changes in radiation pressure and ionization rates. More recently, fluid-kinetic models included the effects of non-stationary solar wind ram pressure on the heliospheric interface (Izmodenov, 2004; Izmodenov et al., 2008; Pogorelov et al., 2010).

The use of a radiative transfer model allows more precise predictions of the interplanetary background line-shifts (Scherer et al., 1999; Quémerais et al., 2008). These models all converge toward a general finding that the IPH velocity should vary by 3-4 km/s over the solar cycle, but they reach different conclusions about the rate of this change and its precise magnitude. Based on previously published values,

none of them have been able to match the data consistently across the entire solar cycle (Quémerais et al., 2008).

Outline of this study

This chapter provides an updated analysis of the IPH velocity measurements obtained over solar cycle 23. In particular we re-analyze high resolution HST archival data from GHRS and STIS to obtain results that differ from previous analyses.

We then compare the broader data set, including previously reported measurements from SOHO/SWAN, with model predictions of IPH velocity variations over a solar cycle to identify points of convergence or divergence, and suggest where additional data is required.

2.2 Observations with HST

2.2.1 Instruments: GHRS and STIS

The Goddard High Resolution Spectrograph (GHRS) was the initial ultraviolet spectrograph on the Hubble Space Telescope (HST) launched in 1990. It was replaced by the Space Telescope Imaging Spectrograph (STIS) during the second servicing mission in 1997.

Both instruments have an echelle mode where the collimated light is dispersed by an echelle grating, relayed by a cross-disperser grating and focused on a detector (Brandt et al., 1994; Woodgate et al., 1998). A more detailed description is also provided in appendix. Comparison of instruments showed that STIS is two times more sensitive than GHRS at Ly-α.

2.2.2 Description of the signal

GHRS and STIS have been used to detect the backscattering of solar Ly-α photons by the interplanetary hydrogen (IPH).

Source location

Bertaux and Blamont (1971) showed that the source function of the IPH photons reaches a maximum around 3 astronomical units (AU). The inner heliosphere (inside 40 AU) is dominated by solar EUV photo-ionization and charge exchange with solar wind protons, while the outer heliosphere is more affected by the heliospheric interface.

Because of an increasing neutral hydrogen density with distance from the Sun, the medium can be considered as optically thin until 10 AU, but not beyond. Full attenuation of the line occurs over a large range of heliocentric distances beyond this point, with backscatter at all points contributing to the observed line-shape and brightness distribution (Quémerais, 2000).

Line of sight

Observations made with GHRS and STIS used the same line-of-sight (LOS): ($\lambda = 253.3°$, $\beta = 7.0°$) in ecliptic coordinates. Table 2.2 shows different coordinates, including the upwind directions of the interstellar hydrogen and helium flows, respectively measured by the SOHO/SWAN instrument (Lallement et al., 2005, 2010) and the Ulysses/GAS-instrument (Witte, 2004).

The line-of-sight is about 2.1° and 2.8° away from the upwind directions of the interstellar hydrogen and helium flows, respectively. All observations have been made during the same period of the year (March-April) when the Earth's and IPH velocity vectors are most directly opposite each other, which provides a maximal Doppler shift with respect to the geocorona.

	HST observations	Hydrogen flow	Helium flow
Instrument(s)	GHRS & STIS	SOHO/SWAN	Ulysses/GAS
reference	STScI	Lallement et al. (2010)	Frisch et al. (2009)
λ	253.3°	252.5°	255.4°
β	7.0°	8.9°	5.1°
angular distance	-	2.1°	2.8°

Table 2.2: References, ecliptic coordinates and angular distances between the different directions. Regarding the measurement of the upwind direction of the interstellar helium flow, the results were initially given in B1950 coordinates by Witte (2004) and have been corrected to J2000 coordinates by Frisch et al. (2009). The angular distance between the hydrogen and helium flows is about 4.8°.

Exposures

GHRS data were obtained on 7 April 1994 and 25 March 1995 using the 1.74″ x 1.74″ large science aperture, the echelle A grating and the side 1 CsI Digicon detector. The spectra were co-added, giving total exposure times of 1496 s in 1994 and 3808 s in 1995. The Earth's velocity along the line of sight was 24.72 km/s and 27.78 km/s respectively.

STIS data were obtained on 29 March 2001 with an exposure time of 2450 s, using the E140H echelle mode with a large aperture (52″ x 0.5″) and the FUV-MAMA detectors. The Earth's velocity along the line of sight was 26.98 km/s. This instrument mode was not supported by the existing HST data reduction pipeline, because, while the large aperture greatly increases signal from an extended source like the IPH, it results in blending of emission in different orders of the echelle spectrum.

Preprocessing of STIS data

STIS observations were processed to perform dark subtraction and flat field correction. The geometric distortion, which affects the vertical alignment of spectral

features, was corrected using the procedure developed by Walsh et al. (2001). The fluxes were calibrated with sensitivity curves that vary along the dispersion direction and depend on the grating order (Proffitt et al., 2010).

2.2.3 Contamination in STIS observations

Cross-dispersed echelle mode

In the cross-dispersed echelle mode of STIS, Ly-α photons appear in two different orders (346,347). The long slits used in the observation are not confined to single order, but are vertically extended such that they intersect all other orders on the detector, hence disrupting the order separation provided by the cross disperser.

As shown by Vincent et al. (2009), the result of this cross-order penetration is that the geocoronal hydrogen and IPH Ly-α lines in both the 346th and 347th orders are contaminated by overlapping light from the 1304 Å triplet line of the geocoronal oxygen (O I) in lower orders (322, 323, 324). This geocoronal O I line, previously detected by Baum et al. (2005) in another STIS spectrum, affects any structure that can be seen, as shown in figure 2.2.

Location of the contaminations

Two echelle orders (322, 323) transmit the central line of the O I triplet (1304.858 Å) that appears as a vertical feature crossing the entire detector in Figure 2.2. This line does not contaminate the geocorona or IPH Ly-α features and can be used as a reference for the other lines in the triplet.

The 1306.029 Å line is also transmitted by the same echelle orders, and it overlaps with the IPH line in the 346th order and with the red wing of the geocorona line in the 347th order.

The third line of the triplet (1302.168 Å) is transmitted by two different echelle orders (323, 324): it intersects the blended region between the IPH line and the blue wing of the geocorona line (346th order), and the extended red wing of the geocorona line (347th order) without intersecting the core of this line.

2.3 Data Analysis

2.3.1 Fitting procedure

GHRS and STIS spectra contain Ly-α line profiles from the geocorona and the IPH, with some contamination from a geocoronal oxygen triplet line in STIS observations. Each line profile was fitted using the convolution of a Voigt profile with a measured or simulated Line Spread Function (LSF).

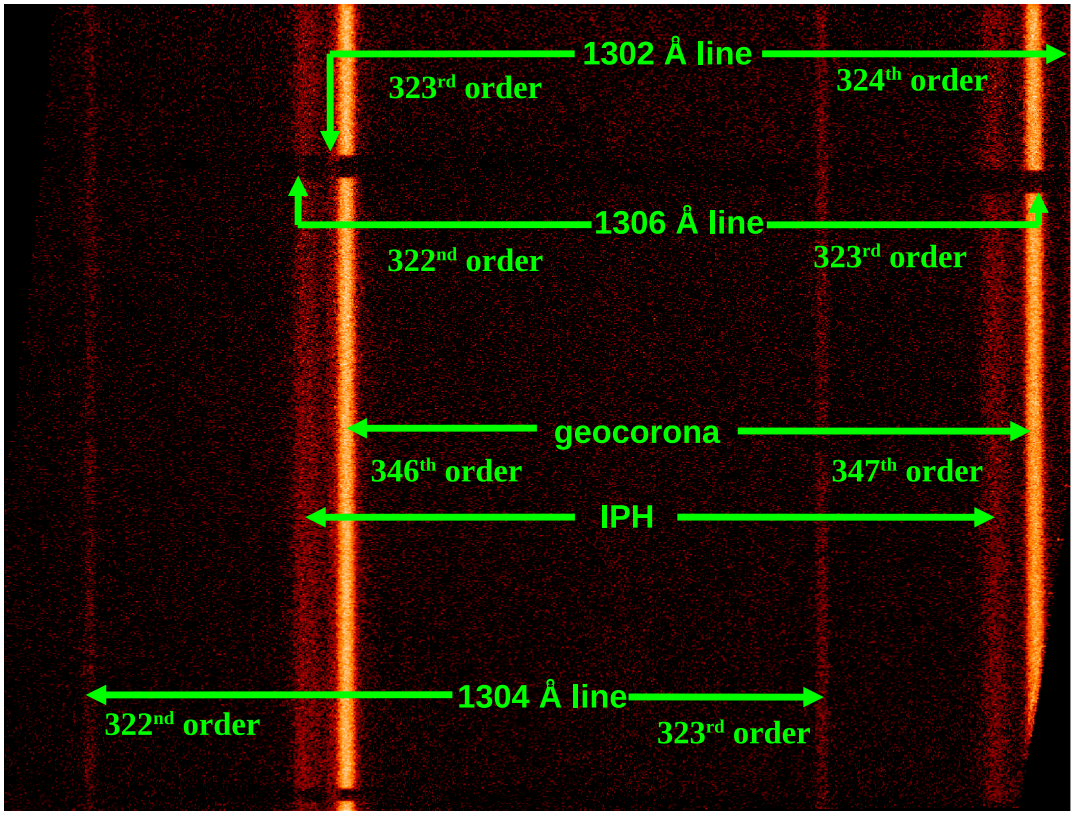

Figure 2.2: STIS spectro-image from observations made on 29 March 2001, after correction of the geometric distortion. The Ly-α lines from IPH and geocorona are transmitted by two orders (346 and 347) but suffer from contamination by geocoronal oxygen lines. The central line of the O I triplet (1304.858 Å) is isolated and clearly visible. Both other lines (1302.168 and 1306.029 Å) overlap with the Ly-α line but appear at the location of the occulting bars where the Ly-α line is blocked.

Line Spread Functions

STIS observations were done in an unsupported mode (E140H with 52″ x 0.5″), which means that a calibration lamp measurement of the LSF has not been obtained. The plate-scale for E140H being 0.047″/pixel, we constructed a LSF from the convolution of a 10 pixel ($\sim$ 0.5″) wide function with a previously measured LSF from two supported modes (E140H with 6″ x 0.2″ or 0.2″ x 0.09″), as shown in Fig. 2.3.

Fitting of the geocorona

Unfortunately, the convolution of the simulated LSF and a Voigt profile for STIS did not fit the blue and red sides of the geocorona. To match these, we used a composite profile consisting of the red side of the geocorona line in the 346th order, which did not contain IPH or O I contamination, and the blue side of another geocoronal

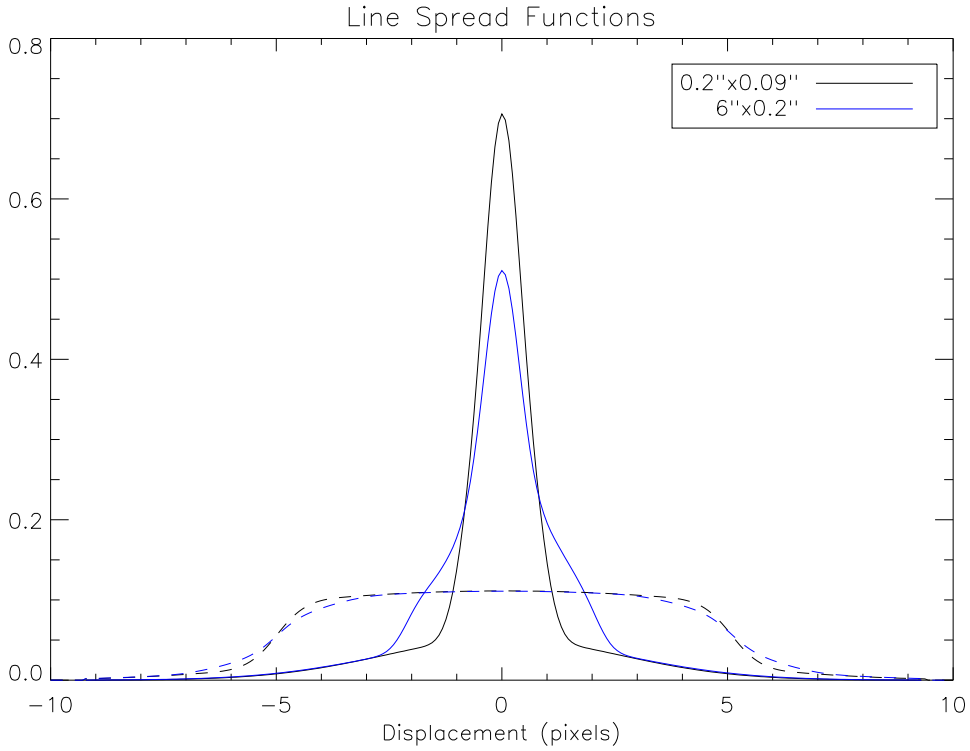

Figure 2.3: Line Spread Functions of the EA140 grating on STIS for different apertures: 0.2″ x 0.09″ (black), 6″ x 0.2″ (blue). The solid lines represent the original LSFs, the dashed lines are the results of a convolution with a 10 pixel ($\sim 0.5''$) wide function.

measurement (made in June 2000 in the crosswind direction) where the IPH line was Doppler shifted to the other side of the geocorona line (Fig. 2.4).

Each side was fit by combining two Voigt functions (convolved with the LSF) that fit the core and the wing of that side. Self-absorption by the geocorona has been taken into account but did not show any significant impact. The observations made in June 2000 were also used to fit the 1306 Å O I line that is transmitted by the 322th order without overlapping with any Ly-α feature.

Algorithm

The line-shift of the IPH along the line of sight is derived from the Doppler shift between the line centers of the geocorona and the IPH, after subtraction of the velocity of the Earth along the line of sight. An absolute wavelength calibration is not needed as we require only a measurement of the difference between two features.

To determine the Doppler separation, the IPH and geocorona lines were fit simultaneously with both the shape of the IPH line and the separation of the two features as free parameters in the MPFIT package (Markwardt, 2008), an IDL library which implements the Levenberg-Marquardt technique to solve the least-squares problem

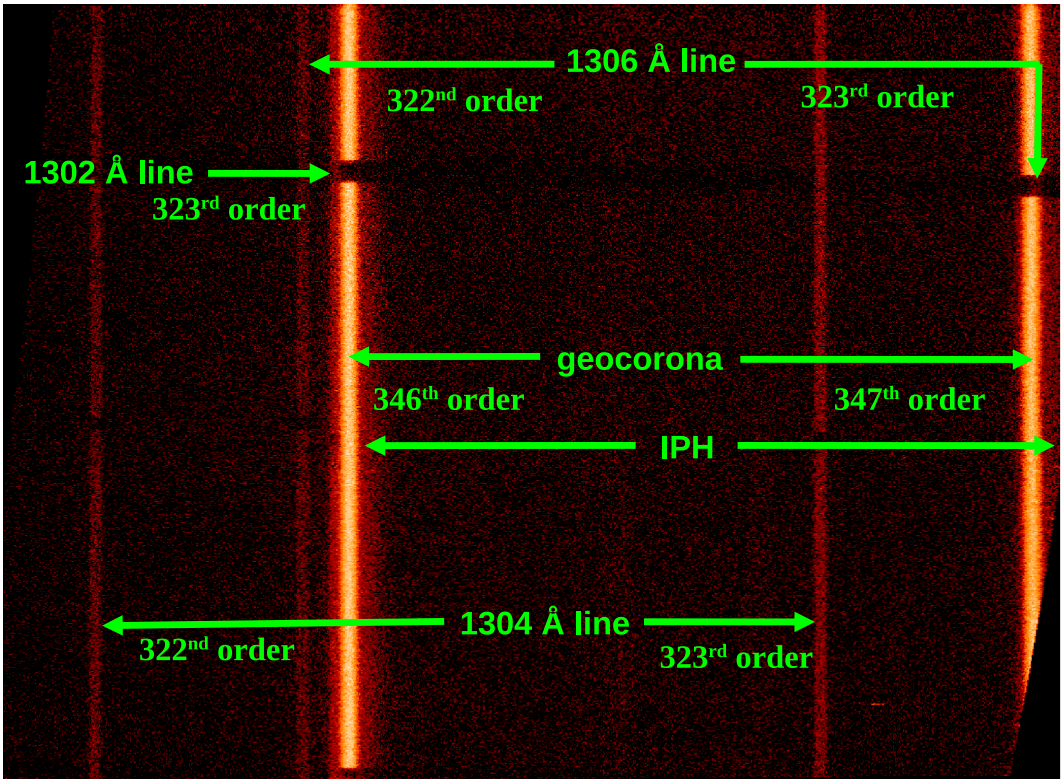

Figure 2.4: STIS spectro-image from observations made in the crosswind direction ($\alpha = 164.90°$, $\delta = 0.32°$) on 29 June 2000. The projection of the IPH velocity on the LOS is almost null while the LOS is opposite to the Earth's velocity vector, resulting into a Doppler shift of the IPH feature on the red side of the geocorona line. We used these observations to fit the blue side of the geocorona line (free of any contamination in the 347th order) and the 1306 Å O I line in the 322th order.

(Marquardt, 1963).

2.3.2 Error analysis

The 1σ errors were computed with $\sigma = \sqrt{\sigma_I^2 + \sigma_S^2}$, where σ_I and σ_S are respectively the instrumental and statistical uncertainties.

Instrumental uncertainties

For GHRS, σ_I is due to the uncertainty on the position of the carousel (a mechanical device that supports the echelle grating), and has been estimated to be ~ 0.274 pixels by Rebull et al. (1998), which corresponds to ~ 0.22 km/s in this configuration.

For STIS, σ_I has been estimated as the standard deviation of an uniform distribution over a pixel ($1/\sqrt{12} \simeq 0.289$ pixels), so ~ 0.38 km/s.

Statistical uncertainties

σ_S reflects the uncertainties on the fluxes (photon noise) that limit the precision of the fit, and was estimated by the MPFIT package.

For GHRS data, the errors on the fluxes are provided by the pipeline. However this was not the case for STIS data because observations have been made in an unsupported mode. After removing the spectra that were incomplete because of image distortion, the remaining spectra (or rows of the spectro-image) were averaged.

Photon noise in STIS data

Let us define n_{ij} the number of photons received in the pixel of the i-th row and j-th column. As shown in Fig. 2.5, an average spectrum is obtained by summing over the rows:

$$s_j = \frac{1}{M} \sum_{i=1}^{M} n_{ij}$$

where s_j is the j-th pixel of the average spectrum, and M is the number of rows (spatial direction of the spectro-image).

For each pixel (i,j) in the spectro-image, the error associated to that pixel is equal to the photon noise, so $\sigma_{ij} = \sqrt{n_{ij}}$. Let us note σ_j the error associated with the j-th average pixel s_j. To estimate this error, one can follow Bevington & Robinson (2003, chap. 3-4) and use the error propagation equation applied to the estimated error in the mean:

$$\sigma_j^2 = \sum_{i=1}^{M} \left[\sigma_{ij}^2 \left(\frac{\partial s_j}{\partial n_{ij}} \right)^2 \right]$$

which yields:

$$\sigma_j = \frac{1}{M} \sqrt{\sum_{i=1}^{M} \sigma_{ij}^2} = \frac{\sqrt{s_j}}{\sqrt{M}}$$

Then one can estimate the signal-to-noise ratio for the j-th average pixel:

$$SNR_j \equiv \frac{s_j}{\sigma_j} = \sqrt{M} \times \sqrt{s_j} \approx \sqrt{M} \times SNR_{ij}$$

where SNR_{ij} is the signal-to-noise ratio for the pixel (i,j) in the spectro-image. The last approximation comes from the fact that the signal source can be considered as spatially uniform, so $s_j \approx n_{ij}$ for any (i,j). One has just demonstrated that, for a diffuse uniform source, the signal-to-noise ratio of an average pixel increases as $\sqrt{M}$, where M is the number of rows (spatial direction).

This makes sense and an analogy can be made with the fact that, for a signal that dominates its background, the signal-to-noise of any exposure increases with

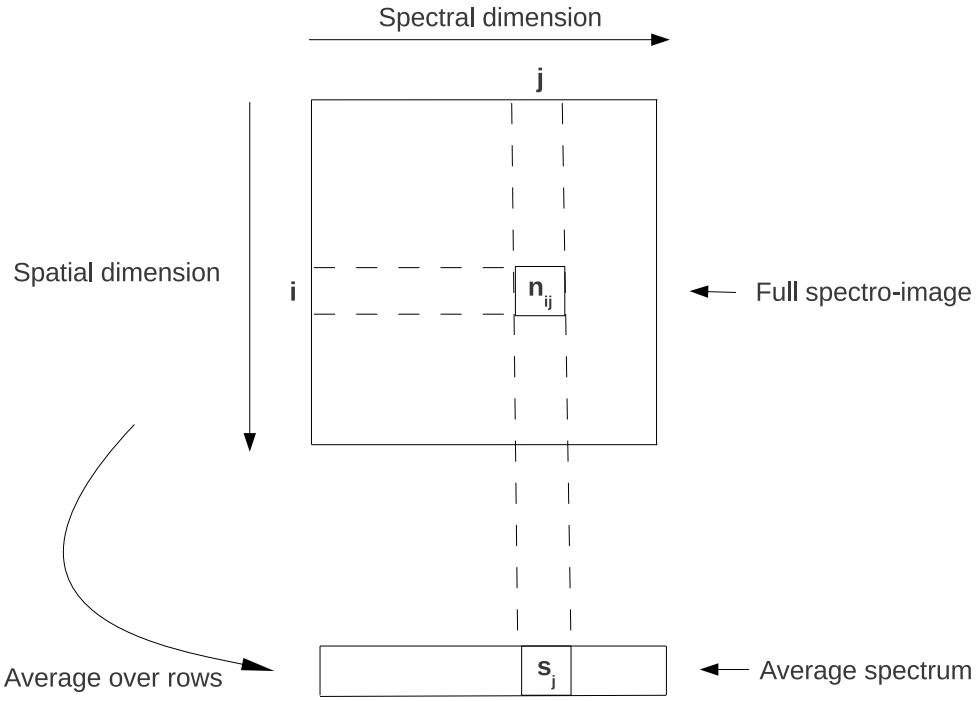

Figure 2.5: Reduction from a spectro-image to an average spectrum. The variable n_{ij} represents the number of photons in the pixel (i,j) of the spectro-image, while the variable s_j represents the number of photons in the j-th pixel of the average spectrum.

$\sqrt{t}$, where t is the exposure time (e.g., Schroeder, 2000, chap. 17). Increasing the spatial dimension of the spectro-image is equivalent to an increase of the exposure time. This is particularly useful for observations with HST/STIS that has a limited available time because of a huge demand from the scientific community. As shown previously, the price to pay is a contamination from other orders of the echelle grating.

Total errors

The true reduced chi-squared value allows to estimate the quality of a fit and is defined by:

$$\chi^2 = \frac{1}{N} \sum_{j=1}^{N} \left(\frac{\widehat{s_j} - s_j}{\sigma_j} \right)^2$$

where $\widehat{s_j}$ is the estimation of s_j by the fitting procedure, and N is the number of columns in the spectro-image (spectral direction). If the fitting procedure provides

an estimation within an error bar ($|\widehat{s_j} - s_j| \approx 1\sigma_j$), then the true reduced chi-squared value will be close to unity ($\chi^2 \approx 1$).

True reduced chi-squared value and total errors are summed up in Table 2.3. The error on GHRS data is clearly dominated by the statistical uncertainties due to the photon noise. For STIS data, the statistical uncertainties become comparable to the instrumental uncertainties, thanks to a better signal-to-noise ratio.

year (instrument)	χ^2	σ_S (km/s)	σ_I (km/s)	σ (km/s)
1994 (GHRS)	0.80	1.51	0.22	1.53
1995 (GHRS)	0.70	0.85	0.22	0.88
2001 (STIS)	1.12	0.19	0.38	0.42

Table 2.3: χ^2 values and error analysis for all observations.

Another algorithm

To reinforce our diagnostic on both the IPH line-shift and related statistical uncertainties, we also used PAN, another fitting software that allows Monte-Carlo simulation of statistical noise propagation on the final results (Dimeo et al., 2005).

We also checked our best fits by shifting wavelengths to measure the corresponding residuals and found that the estimated statistical errors correspond to the χ^2 value so far derived.

2.3.3 Results

Numerical values

Figure 2.6 shows the fit for STIS observations. The IPH line in the 346th order is contaminated by the 1302.168 Å O I line, so only the 347th order was used to derive the IPH line-shift. Our best fit to the STIS observations takes into account the contamination of the geocorona line on the red side by the O I lines, and provides a line-shift of 22.4 ± 0.4 km/s in 2001.

GHRS spectra were extracted using the existing pipeline. After fitting the lines with MPFIT and PAN, we obtained line-shifts of 24.0 ± 0.9 km/s in 1995 (Figure 2.7) and 22.2 ± 1.5 km/s in 1994 (Figure 2.8).

Optically thin approximation

We use an optically thin approximation for the IPH line. This is not strictly true but was shown to give good results for line-shifts in the upwind direction (Quémerais, 2000). So any observed line-shift represents approximately the bulk velocity of the IPH atoms (projected and integrated along the line of sight from the Earth).

Since the HST observations are all within 2.1° of the incoming direction, projection effects can be ignored ($\cos(2.1°) \simeq 0.999$). Therefore line-shifts are a good approximation of the IPH velocity in the upwind direction.

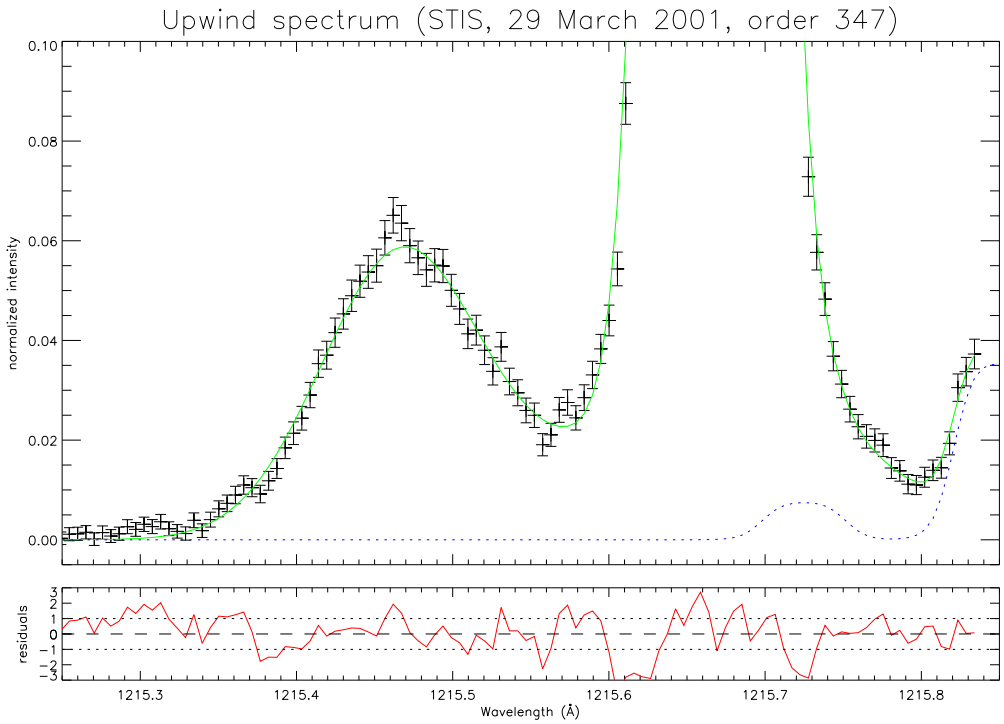

Figure 2.6: Fitting of STIS observations (29 March 2001) for the order 347. The blue dotted lines represent the contaminations by oxygen lines: 1306.029 Å (order 323) and 1302.168 Å (order 324), from left to right. This fit provides a line-shift of 22.4 ± 0.4 km/s.

Primary and secondary populations of interstellar hydrogen atoms

Following the method established by previous authors (Scherer et al., 1999; Quémerais et al., 2006), we fitted the data assuming a single Voigt profile for the IPH feature, despite the fact that it is expected that several different populations with individual distributions will alter the actual shape from that of a single Voigt profile.

As shown in figure 2.6, there is no evidence in the residuals for the presence of an offset secondary population at the spectral resolution of the STIS 52″ x 0.5″ slit. This is likely due to any difference being smaller than the accumulated uncertainty. We looked for a better fit of the IPH line profile with a combination of two populations (primary and secondary) but this did not produce any improvement in the quality of the fit.

The need for calibration observations

The fits could be also improved with a better estimate of the LSF for STIS observations. This could be achieved with the use of one of the three hollow cathode Pt/Cr-Ne arc lamps that will provide a thinner emission line.

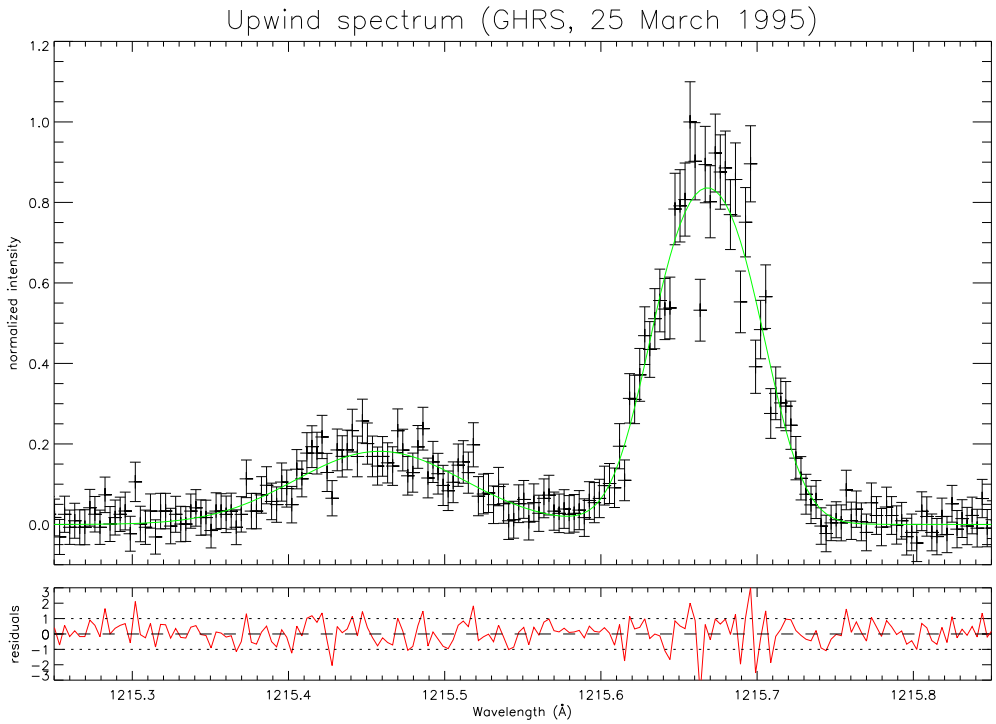

Figure 2.7: Fitting of GHRS observations (25 March 1995). This fit provides a line-shift of 24.0 ± 0.4 km/s.

Lamp observations can not be done with the 52″ x 0.5″ slit because the slit will be entirely filled and the illumination will exceed the bright object protection limits for the FUV-MAMA detector. However it is possible to take an E140H observation with the 0.2″ x 0.5″ slit without exceeding the bright object protection limits or overlapping the orders excessively.

Other possible features in the signal

In STIS observations (Figure 2.6), a couple of features appear between 1215.2 Å and 1215.4 Å. They could be related to the Ly-α radiation of geocoronal deuterium (Krasnopolsky et al., 1998) and a feature derived from a possible Fermi process at the heliospheric interface (Ben-Jaffel et al., 2000).

However the signals are just above the noise level. Moreover there is some uncertainty on the LSF, so lamp observations are required to confirm the presence of these features.

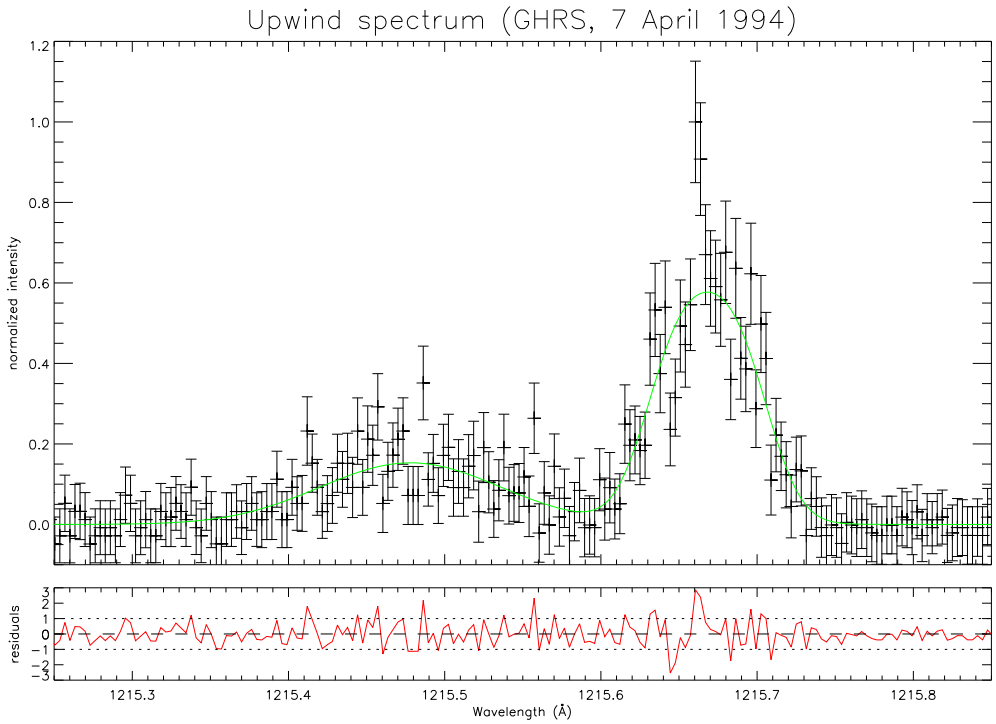

Figure 2.8: Fitting of GHRS observations (7 April 1994). This fit provides a line-shift of 22.2 ± 1.5 km/s.

2.4 Discussion

2.4.1 Comparison with other studies

Previous analyses of HST data

Table 2.4 makes a comparison of this work with previous analyses. Our results for GHRS observations differ significantly from those previously published by Clarke et al. (1995, 1998). The reasons of these consequent differences are still not clear. Scherer et al. (1999) had similar results to ours for the observations in 1995. Our results and those of Ben-Jaffel et al. (2000) (hereafter B2000) differ substantially from Scherer et al. (1999) for 1994, though the error envelopes of each data point overlap at their limits.

B2000 found different results for 1995, but there are some subtle differences between the two analyses (the use of a two-component fit to the match the possible Fermi feature; the fitting algorithm) and these may account for the difference. The net effect though is that it is very possible that the actual velocity is between ours and the B2000 number. This has consequences for the match between the data and the models.

Quémerais et al. (2006) found a lower velocity for STIS observations. However they used the 346th order (Clarke et al., 2010) which is more contaminated by O I

lines (especially in the IPH feature) and thus more difficult to fit accurately than the 347th order that has been used for this work.

Reference	1994	1995	2001
Clarke et al. 1998	18 ± 2	21 ± 2	-
Scherer et al. 1999	20.7	24.3	-
Ben-Jaffel et al. 2000	22.9	23.3	-
Quémerais et al. 2006	-	-	20.3 ± 0.2
This work	22.2 ± 1.5	24.0 ± 0.9	22.4 ± 0.4

Table 2.4: IPH velocity (km/s) from data analyses of GHRS & STIS

Comparison with SWAN data

Quémerais et al. (2006) derived interplanetary Ly-α line profiles from annually averaged observations made by the SWAN instrument. Their findings indicate a velocity change from 25.7 ± 0.2 km/s to 21.4 ± 0.5 km/s in the solar rest frame between 1997 and 2003. The HST data do not overlap the specific periods of the SOHO observations, however the periods they do cover (1994, 1995, and 2001) include the waning and waxing phases of the same solar cycle. We then have upwind IPH velocity measurements for most of the previous solar cycle (23). They provide a baseline for an initial study of effects of short-term solar cycle dependencies on the IPH velocity.

Figure 2.9 plots the IPH velocities found by this work for GHRS & STIS observations, and by Quémerais et al. (2006) for SWAN data and STIS observations. In order to show the possible solar cycle effect, we over-plotted the predictions of the physically realistic models developed by Quémerais et al. (2008) and Scherer et al. (1999) (noted Q2008 and S1999 respectively). The Q2008 model was also interpolated with Fourier series in order to extend their predictions over a larger interval and compare them with GHRS observations.

Comparison with numerical simulations of the IPH velocity

The Q2008 model was developed to interpret the SWAN data (1997-2003). It uses the kinetic-fluid model of Izmodenov et al. (2008) including the time variations of the solar parameters (solar wind flux, ratio of solar radiation pressure to solar gravitation, ionization rates) to compute the hydrogen velocity distribution, and a radiative transfer code using Angle Dependent Partial Frequency Redistribution (ADPFR) to model the scattering process and deduce the line profile (Quémerais, 2000; Quémerais and Izmodenov, 2002).

The S1999 model was developed to interpret the GHRS observations (1994/95). It combines the twin shock model of Baranov and Malama (1993) with a time-dependent hydrogen model (Rucinski and Bzowski, 1995; Bzowski et al., 1997) and a radiation transport model (Scherer and Fahr, 1996). Scherer and Fahr (1996)

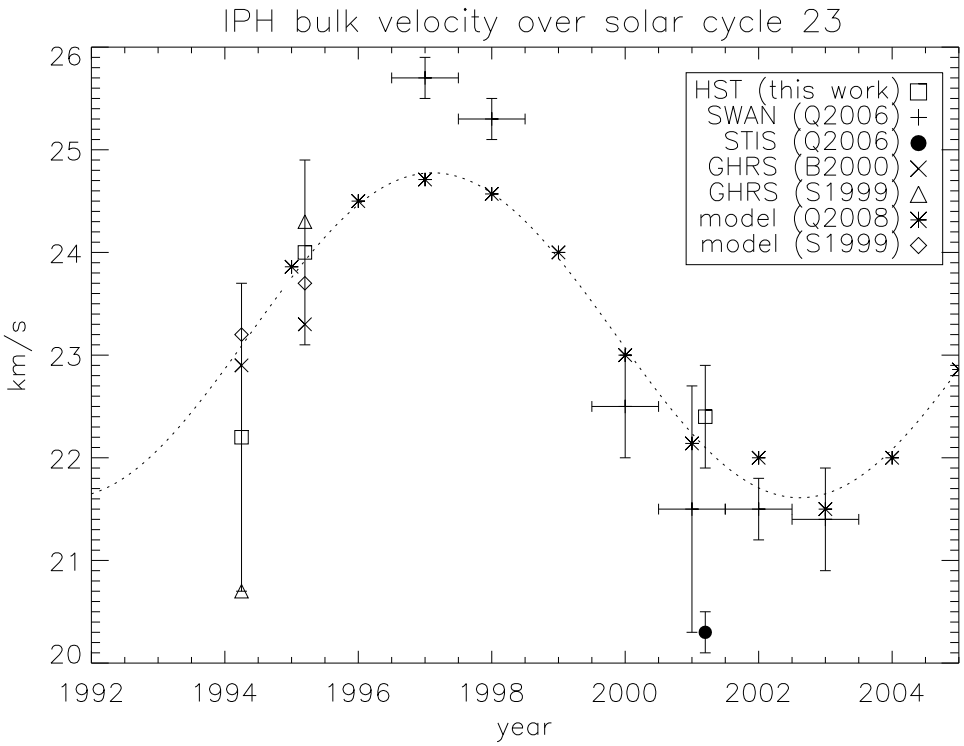

Figure 2.9: IPH bulk velocity in the upwind direction over solar cycle 23, with values reported by this work (squares for GHRS and STIS), by Quémerais et al. (2006) (plus signs for SWAN data, triangle for STIS observations), by Ben-Jaffel et al. (2000) (crosses) and Scherer et al. (1999) (triangles). The dotted curve is a Fourier interpolation of the model proposed by Quémerais et al. (2008) (asterisks). The values predicted by the model of Scherer et al. (1999) are represented with diamonds.

computed only the first scattering term and neglected multiple scattering effects: although this approach is not appropriate to estimate the Ly-α intensities, it gives a good approximation of the line profile and a line-shift within 1 km/s from the ADPFR result (Quémerais, 2000).

Compared to the value obtained by Quémerais et al. (2006), the updated STIS data reduction provides an IPH velocity that is more consistent with SWAN data and the Q2008 model for the period near solar maximum (in 2001). Similarly our revised GHRS analysis provides a much better fit to the models than that provided in Scherer et al. (1999). As a consequence, all data are within or close to 1σ from Q2008 and S1999 models, at the exception of the SWAN measurements in 1997/98.

Potential trends

Near solar minima (1994 and 2000-2003), every point from GHRS or SWAN is centred below the Q2008 model (Figure 2.9). Since the extent to which they are

'low' is within 1σ, it is difficult to determine if the difference is physically significant, a by-product of the data analysis, or an instrumental effect. However, it is unlikely that a consistent analysis or instrumental bias could explain both GHRS and SWAN, which are very different instruments.

Excluding the SWAN data of 1997/1998, a notable feature of the data is that they all are within or close to 1σ from each other. This effect is almost certainly not evidence of an unchanging IPH bulk velocity, but rather an artefact of the relatively large uncertainties in some of the measurements and of the timing of the observations. The lone exception to this trend is the 1995 GHRS data point, which is 1.8 km/s faster than the 1994 value. However, even for this point, the similar analysis of Ben-Jaffel et al. (2000) suggests a lower value that would bring it in line with the others. It is clear that additional data at higher precision are needed to better characterize the trend.

2.4.2 Possible reasons for discrepancies

Allowing for the statistically significant fit between the data and models near solar maximum, the primary discrepancy is found at solar minimum, where the SWAN data implies a velocity more than 2σ faster than the model. Two explanations that do not exclude one another, can be proposed to account for this difference: these include possible systematic uncertainty in the SOHO-SWAN data processing and/or an incomplete description of the IPH neutrals by the fluid-kinetic models (Scherer et al., 1999; Izmodenov et al., 2008).

SWAN measurements

The nature of SWAN measurements is such that there are unavoidable factors that can have a significant effect on the derived IPH velocity and/or the size of the error bars. SWAN obtains measurements of the IPH velocity indirectly: a hydrogen cell absorbs any Ly-α photon lying within $\pm$ 20 mÅ from the rest wavelength and acts as a negative filter, which allows to measure the ratio of intensities (reduction factor) by turning the cell on and off (Bertaux et al., 1995). The instrument uses the Earth's orbital velocity to provide a Doppler shift and scan the emission line of the IPH, so one year of observations is required to reconstruct the full line profile (Quémerais et al., 1999). This is a well-proven technique, but with accuracy subject to the performance characteristics of the hydrogen cell, which, in the case of SWAN, was evolving temporally during the course of the cycle 23 observations (Quémerais et al., 2006, table 1).

In addition, the observations represent an annual average of absorption measurements that must be inverted to a line profile as opposed the single, direct measurement of the spectral line at one point in time obtained from HST. There is substantial evidence that this annual stability in IPH velocity cannot be assumed. For instance, GHRS and SWAN report a shift in IPH velocity of 1.8 km/s (between 1994 and 1995) and 2.8 km/s (between 1998 and 2000) respectively. The two SWAN measurements obtained in 1997/98 report a shift of 0.5 km/s during

the period of their average measurement but displayed an uncertainty of only 0.2 km/s that is much smaller than the annual changes reported before, during, and after the measurements were made. It seems self-evident that the uncertainty at an annual averaged measurement should be at least as large as the amount by which the measured quantity changed in that period. While the interpretation of the effect of a changing target velocity on the derived line shape from an absorption cell is difficult, its effect on the uncertainties may be more straightforward.

Influence of the local interstellar magnetic field

Quémerais et al. (2006, 2008) showed that the temporal variation of the line-shifts is mainly due to the radiation pressure the intensity of which depends on the solar cycle. However these authors were not able to explain the discrepancy between their model and the data, especially SWAN data in 1997/98.

If we assume that SWAN data points of 1997/98 are correct, then a new process that modifies the IPH velocity distribution must be added to the description used by previous authors (Scherer et al., 1999; Izmodenov et al., 2008). The effect of this process must be such that it is stronger near solar minimum than near solar maximum. This physical process could be directly related to the solar parameters, this is why Quémerais et al. (2008) suggested that the discrepancy between data and models could be due to the anisotropy of the ionization rate. However it could be also an indirect effect of the interstellar influence, notably the local interstellar magnetic field that has not been taken into account by the previous authors.

Models taking into account the oblique local interstellar magnetic field (LIMF) have shown severe distortion in the shape of the heliopause (Fahr et al., 1988; Ratkiewicz and Ben-Jaffel, 2002; Izmodenov et al., 2005b). Ben-Jaffel et al. (2000) showed that the excess of backscattered solar Ly-α photons detected by *Voyager 1* UVS can be interpreted as a tilt of the heliosphere's nose by respect to the upwind direction, resulting from an oblique LIMF with a deviation $\sim 40°$ from the interstellar flow direction. Results obtained by SWAN showed that the interstellar neutral hydrogen flow is deflected relative to the helium flow, providing new evidence for the obliquity of the LIMF (Lallement et al., 2005, 2010). More recent models can account for the 10 astronomical units (AU) difference in the TS heliospheric distances observed by the *Voyager 1* and *Voyager 2* spacecraft (Ratkiewicz & Grygorczuk, 2008; Pogorelov et al., 2009; Opher et al., 2009). Even more recently, Interstellar Boundary EXplorer (IBEX) found a ribbon of energetic neutral atoms around the heliosphere, another proxy of the influence of the LIMF (McComas et al., 2009; Heerikhuisen et al., 2010). Comparison of *Voyager* data with three-dimensional MHD simulation suggests that the magnetic field in the inner heliosheath, previously assumed to be fully laminar, could contain densely packed magnetic islands (Opher et al., 2011). All observations and data analyses converge on the fact that the deviation of the LIMF from the interstellar flow direction is between 30° and 60°.

Because of the tilted nose, the density maximum will be shifted from the upwind direction as shown by most magneto-hydrodynamic and kinetic hydrogen models

(Izmodenov et al., 2005b; Ratkiewicz et al., 2007; Pogorelov et al., 2009). Therefore the upwind line of sight may probe regions with smaller densities and less charge exchange filtration in the outer heliosphere in the upwind direction. This weaker interaction would lead to a faster velocity component in the outer heliosphere but with a smaller weight, while the inner heliosphere component would have a bigger weight, leading to a higher IPH velocity than current models predict in the upwind direction. An oblique LIMF may thus result in a larger difference of IPH velocity (compared to IPH velocity without LIMF) at solar minimum than at solar maximum. This descriptive explanation can be explained by a simplified model.

Simplified model

We can evaluate the influence of an oblique LIMF on the IPH velocity and its variations. Let us note $\mathbf{u}_{LOS}$ the unity vector that is parallel to the line of sight (LOS). We consider the optically thin approximation, so the observed line-shift (V_{IPH}) is equal to the IPH velocity distribution projected on $\mathbf{u}_{LOS}$, integrated in the velocity space and along the line of sight, and normalized:

$$V_{IPH} = \frac{\int\int(\mathbf{v}\cdot\mathbf{u}_{LOS})\, f(\mathbf{v},r)\, d\mathbf{v}\, dr}{\int f(\mathbf{v},r)\, d\mathbf{v}\, dr} = \frac{\int v(r)\, f(r) dr}{\langle n\rangle}$$

where r is the distance from the Sun, $v(r)$ the local bulk velocity projected on the LOS and $\langle n\rangle$ the column density along the LOS. By linearity of the integral, V_{IPH} can be modelled as the sum of two components :

$$V_{IPH} = \alpha * V_{out} + (1-\alpha) * V_{in}$$

where V_{out} and V_{in} are the bulk velocities of the velocity distributions outside and inside the heliopause respectively. The coefficients α and $(1-\alpha)$ represent the weights of each component, they are proportional to the average hydrogen densities in both regions. Let us use upper indexes, B and NB, to differentiate the situations with (α^B) and without an oblique LIMF (α^{NB}) respectively. We define $\Delta\alpha = \alpha^{NB} - \alpha^B$. Then we can consider that the bulk velocity inside the heliopause does not depend on the LIMF ($V_{in}^{NB} \simeq V_{in}^B$) and it will then be noted simply V_{in} or declined into V_{in}^{max} and V_{in}^{min} to distinguish solar extrema.

In the presence of an oblique LIMF, the Hydrogen Wall will be off-centred from the upwind direction, leading to a lower weight of the hydrogen distribution outside the heliopause : $\alpha^B < \alpha^{NB}$, so $\Delta\alpha > 0$. On the other hand, hydrogen atoms will have a greater bulk velocity because of a lower deceleration through charge exchange, so $V_{out}^B > V_{out}^{NB}$. At the first order, we can assume that both inequalities compensate for each other, $\alpha^B * V_{out}^B \simeq \alpha^{NB} * V_{out}^{NB}$ which brings :

$$\Delta V = V_{IPH}^B - V_{IPH}^{NB} \simeq (\alpha^{NB} - \alpha^B) * V_{in} = \Delta\alpha * V_{in}$$

We showed that the term $\Delta\alpha$ is positive, so it gives :

$$V_{IPH}^{B} > V_{IPH}^{NB}$$

Including an oblique LIMF will increase the bulk velocity V_{IPH} because it gives more weight to the inside component ($1 - \alpha^{B} > 1 - \alpha^{NB}$) without changing the final contribution of the outside component ($\alpha^{B} * V_{out}^{B} \simeq \alpha^{NB} * V_{out}^{NB}$). Now we want to evaluate the extent of this increase, depending on the phase of the solar cycle. Under the influence of the solar wind, the variation of the number densities of all neutral hydrogen populations does not exceed 10% at distances greater than 10 AU from the Sun (Izmodenov et al., 2005a). This is why we can assume that the weights α^{B} and α^{NB} are more affected by the presence of an oblique LIMF than by solar variations, so we can write $\Delta\alpha^{min} \simeq \Delta\alpha^{max}$.

Thus the difference between both cases ($\Delta V = V_{IPH}^{B} - V_{IPH}^{NB}$) depends mainly on the the bulk velocity inside the heliopause (V_{in}), that will be lower at solar maximum ($V_{in}^{max} < V_{in}^{min}$) because of a higher radiation pressure, which gives :

$$0 < V_{IPH}^{B,max} - V_{IPH}^{NB,max} < V_{IPH}^{B,min} - V_{IPH}^{NB,min}$$

To sum up, the inclusion of an oblique LIMF does not change the contribution of the outside component at the first order ($\alpha^{B} * V_{out}^{B} \simeq \alpha^{NB} * V_{out}^{NB}$). But it gives more weight to the inside component ($1 - \alpha^{B} > 1 - \alpha^{NB}$), leading to a velocity increase proportional to the inside velocity ($\Delta V \simeq \Delta\alpha * V_{in}$) with a larger increase at solar minimum that could explain the discrepancy between the current models and the SWAN data in 1997/98.

2.4.3 The need for new data

The identified issues with data near solar maximum, including the consistently low velocities obtained and the larger uncertainties, along with the discrepancy between the models and the lone data points at solar minimum, all argue for the acquisition of new data. It has been nearly a full solar cycle since the last SWAN measurements in 2003, during which no additional velocity resolved data have been obtained. Future high-resolution measurements are required to reduce the current uncertainties, better characterize the trend induced by the solar cycle and answer the questions raised by the discrepancy at solar minimum.

At this time, only HST/STIS is in a position to contribute new results, and they would have much greater precision than either SOHO/SWAN or HST/GHRS, particularly if an instrumental LSF is obtained. High-resolution measurements of the IPH velocity could be acquired each year with one HST-orbit exposure (about 45 minutes) in March-April, using the E140H grating and the 52″ x 0.5″ aperture. Such a configuration would provide a resolving power of about 20,000 with a signal-to-noise ratio of about 20 at the IPH signal peak. The addition of a calibration spectrum using the 0.2″ x 0.5″ aperture can be used to obtain a more reliable instrument LSF and further improve the analysis. Moreover the work presented here provides a new reduction pathway for this previously unsupported mode. It should be straightforward to analyze new HST/STIS observations.

2.5 Conclusion

Updated analyses of both HST/GHRS and HST/STIS observations provide IPH bulk velocities of 22.2 ± 1.5, 24.0 ± 0.9 and 22.4 ± 0.4 km/s in 1994, 1995 and 2001, respectively. These results are much more consistent with existing models. With the exception of the SOHO/SWAN data at 1997/98 near solar minimum, all of the data now trend within 1σ of the most physically realistic models.

In addition, the influence of the interstellar magnetic field on the heliosphere and its obliquity by respect to the interstellar flow have been proved by a multi-observational approach over the last decade (Ly-α observations by *Voyager*/UVS and SOHO/SWAN, crossing of the terminal shock by the *Voyager* spacecraft and detection of a ribbon of energetic neutral atoms by IBEX). We think that this obliquity may explain the discrepancy between models and data treating of the IPH velocity at solar maximum, and therefore it should be included in future time-dependent kinetic-fluid models.

The rather large uncertainty of some measurements near solar maximum make it difficult to identify any trend in the IPH velocity. These uncertainties and the discrepancy at solar minimum call for the acquisition of future high-resolution measurements with HST/STIS or a new instrument such as HYPE-INSPIRE.

We also provide an updated procedure for utilizing HST/STIS in the unsupported mode that has been previously described. This tool can be applied to archival HST/STIS planetary observations made with this aperture (e.g., Ben-Jaffel et al., 2007, 2010), or to new data, including possible observations of the IPH line during the current solar cycle.

Chapter 3

HYPE-INSPIRE

Observing the backscattering of solar Ly-α by the interplanetary hydrogen brings precious information on the heliospheric interface. Currently only HST/STIS and SOHO/SWAN have the spectral resolution and the sensitivity to make velocity observations. Launched in 1995, SOHO/SWAN is dedicated to Ly-α observations but last observations with the absorption cell date from 2002 (Quémerais et al., 2006). HST/STIS is a wonderful instrument with a wide field of utilisations but has a very limited access because of the huge demand from the scientific community.

In this context, the HYPE-INSPIRE represents an opportunity for new Ly-α observations of the IPH and hopefully new science. HYPE-INSPIRE is a complex instrument which combines a spatial heterodyne spectrometer (SHS) with a polarizer and allows one-dimensional imaging, it will have a high spectral resolution ($R \approx 10^5$) and a polarimetric precision of 1%.

I will first review the scientific motivations of the project. Then I will explain the principles of the SHS concept. Finally I will describe the polarimetric part of the experiment and its optical design.

3.1 Scientific motivations

3.1.1 Scientific goals

Interplanetary Hydrogen

The interplanetary hydrogen (IPH) is an excellent target for a SHS. This is clearly an extended source as it fills the heliosphere. Moreover it possesses a resonance transition line (Lyman-α) that backscatters the solar photons.

There are different scientific motivations to study the IPH. Its interstellar origin makes a proxy to study the interstellar medium. This is also a tracer of the heliospheric interface because of charge exchange with protons that are decelerated and deviated at the heliopause. As explained in the previous chapters, its bulk velocity has temporal variations that reflect the impact of the solar cycle and maybe an indirect effect of the interstellar magnetic field.

Moreover the IPH line profile results from the superposition of different populations. The primary and the secondary population of hydrogen atoms both come from the interstellar medium. The primary population does not have any charge exchange when crossing the heliospheric interface, and therefore has a higher bulk velocity than the secondary population. Because the velocity difference is small, both populations overlap and have not been resolved by the past and current instruments. High resolution spectroscopy may be able to separate both populations and bring valuable information on the interstellar medium and the heliospheric interface.

Magnetic field of Jupiter

Jupiter is an important object of study in the field of planetary sciences. This is a giant gaseous planet with a significant amount of hydrogen in its atmosphere, which makes another interesting target for observations of Lyman-α radiation. Moreover polarimetry measurements would bring precious informations on the magnetic field through the Hanle effect.

The Hanle effect leads to a modification of the linear polarization arising from resonance-line scattering, in contrast to the circular polarization associated with the well-known Zeeman effect. The change in the linear polarization of resonance-scattered radiation in the presence of a magnetic field is related to the radiative lifetime of the atomic transition. Atomic physicists have used the Hanle effect to derive transition probabilities by observing the response of a polarimetric signal to a known ramped magnetic field. For astrophysical applications, the transition probabilities are taken as given, and the Hanle effect can be employed to derive the properties of stellar magnetic fields (e.g., Ignace et al., 1999).

In the case of Jupiter, the surface magnetic field ($\sim$1 bar level) could be detected by observing the change of linear polarization induced by the Hanle effect on the Lyman-α emission line of the planet. Ben-Jaffel et al. (2005) showed that the Hanle effect is sensitive to relatively weak values of the magnetic field strength and enhances the Lyman-α linear polarization, resulting in polarization rate that may exceed 2% at specific regions of the jovian disk. Therefore an accurate mapping of the linear polarization rate may provide a rather accurate estimate of the jovian total magnetic field strength on large area scale.

3.1.2 Benefits of interferometers in astrophysics

Remote sensing helps to understand the physics that take place in astronomical objects. Imaging gives access to the spatial distribution, while spectroscopy measures the line-of-sight component of the velocity distribution. Polarimetry complements these observations further by constraining either the light scattering geometry or the phase functions of the scattering agents.

Fabry-Pérot interferometers and Fourier-transform spectrometers are the best-known types of high-resolving power spectrometers used in astronomy. FPIs and FTSs are particularly well suited for extended sources with few discrete emission

lines and little background continuum. In the solar system, this applies especially to the far-ultraviolet (FUV) range: the solar continuum intensity begins to drop rapidly for $\lambda < 250$ nm and is completely dominated by emission lines below 160 nm. However this range of wavelengths is absorbed by the Earth's atmosphere and requires sounding rockets or satellites to make observations.

The spatial heterodyne spectrometer (SHS) belongs to the class of Fourier-transform spectrometers (Harlander et al., 1992). This is a compact instrument that does not require moving parts, contrarily to other interferometers, so robust enough to be flown in space.

3.2 All-reflective Spatial Heterodyne Spectrometer (SHS)

3.2.1 Genesis and development

SHS Concept

The spatial heterodyne spectrometer (SHS) is a Fourier transform spectroscopy method that has been rediscovered, conceived and developed at the University of Wisconsin (Harlander, 1991; Roesler et al., 2003). The first description of a SHS was given by Dohi & Suzuki (1971) and its configuration is similar to the SISAM interferometer (Connes, 1958).

The technique is initially based on a Michelson interferometer modified by replacing the mirror in each arm with diffraction gratings (Harlander et al., 1992), as shown in Figure 3.1. This interferometer creates a Fizeau fringe pattern, which is perpendicular to the diffraction plane and whose Fourier transform yields the input spectrum. There is an all-reflective SHS that uses a single grating as a beam-splitter and the dispersive element. The all-reflective SHS is particularly useful in the range of vacuum and extreme ultraviolet (VUV-EUV), where transmitting elements have big losses.

Development for ultraviolet range and spatial missions

The use of a SHS can be well suited for emission lines from faint extended sources, and has been implemented for different kinds of observations. For instance, SHIMMER is a SHS which was integrated on a STPSat-1 satellite in order to observe the solar resonance fluorescence of mesospheric hydroxyl near 308 nm (Harlander et al., 2002, 2003). An all-reflective SHS has been implemented by a group at Boston University (SCARI project) to observe the backscattering of solar Lyman-α photons by the IPH with one-dimensional imaging (Chakrabarti et al., 1994; Stephan et al., 2001).

The SCARI project proved the feasibility of Ly-α observations by an SHS on a sounding rocket. At UC Davis, a similar instrument is in development (HYPE-INSPIRE project, or HYPE) and will observe the IPH and Jupiter (Harris et al.,

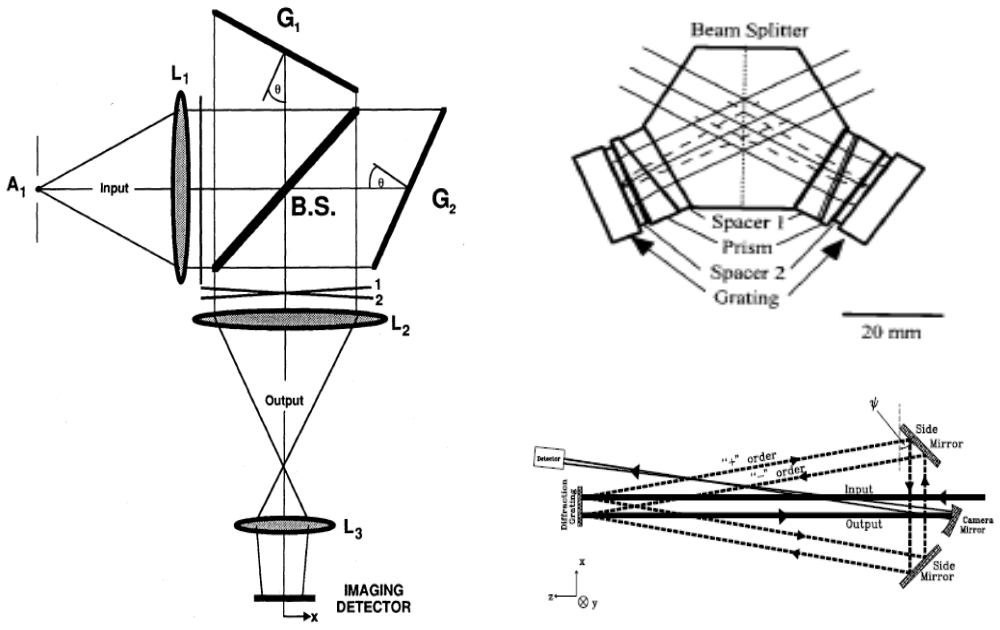

Figure 3.1: *Left:* SHS configuration based on a Michelson interferometer. Figure from Harlander et al. (1992). *Right-top:* Scale drawing of SHIMMER. Figure from Harlander et al. (2003). *Right-bottom:* all-reflective SHS implemented for the SCARI project. Figure from Stephan et al. (2001).

2004; Bétrémieux et al., 2010). Compared to SCARI, HYPE has several advantages: the use of a roof mirror, an anti-aliasing design and a polarimeter. These different aspects will be described with more details later.

Exploring the wavelength range

It should also be noted that tunable versions of SHS have been conceived and are currently developed in the visible range during the last years (Dawson & Harris, 2009; Hosseini et al., 2010). This kind of SHS allows a wider bandpass but requires a rotating mechanism. Monolithic versions are preferred for sounding rocket experiments, because of the harsh environment during a flight and the need for robustness.

SHS are also being developed in the infra-red range (e.g. Englert et al., 2009) but this is beyond the scope of this work.

Imaging capability

The SHS technique allows one-dimensional (1D) imaging, in the direction perpendicular to the diffraction plane, with the use of toroidal exit imaging optics (Stephan et al., 2001; Damiani et al., 2008; Bétrémieux et al., 2010).

3.2.2 Instrument design

Basics of interferometry

The intensity distribution produced by the interference of two coherent plane wave-fronts characterized by wave-vectors $\mathbf{k}_1$ and $\mathbf{k}_2$ (ignoring polarization) is:

$$I = I_1 + I_2 + 2\sqrt{I_1 I_2}\cos((\mathbf{k}_1 - \mathbf{k}_2)\cdot\mathbf{r} + \varphi_1 - \varphi_2)$$

Where I_1 and I_2 are the intensities of the individual waves and, φ_1 and φ_2 are their phases at the origin of $\mathbf{r}$. If $I_1 = I_2 \equiv I_0/2$ and $\varphi_1 = \varphi_2 = 0$, then the equation reduces to:

$$I = I_0(1 + \cos((\mathbf{k}_1 - \mathbf{k}_2)\cdot\mathbf{r}))$$

If the wave-fronts have different wave-vectors, their superposition will create interference patterns. If we note $\mathbf{k} = 2\,\pi\,\mathbf{u}/\lambda$ where $\mathbf{u}$ is a unit vector, then the x-component of the wave-vector will be $k_x = 2\,\pi\,u_x/\lambda$, and the fringe frequency in the x-direction will be:

$$f_x = \frac{1}{\lambda}(u_{x1} - u_{x2})$$

Grating equation

The grating equation is given by:

$$d\,(\sin\alpha + \sin\beta) = m\,\lambda$$

Where d is the spacing between two adjacent grooves, α is the incidence angle, β is the exit angle, m is the considered order and λ is the wavelength of the incoming light. One needs also to define the groove density of the grating: G=1/d.

Common-path

Let us consider the trajectory of light diffracted by a grating and reflected by two mirrors, as show in Fig. 3.2. We assume that the system is symmetric by respect to the optical axis. For the sake of simplicity, we look at only one order and disregard the other ones. Under normal incidence, the light is diffracted with an exit angle that depends on the wavelength of the incoming wave and the diffraction order.

There is one trajectory, such that the light will hit the grating at the same spot than for the first bounce. Because of the symmetry of the system, the opposite order will have the same trajectory, but in the opposite way. This is why we define this particular trajectory as the common path.

By considering the appropriate triangles, one can easily show that the exit angle after the first bounce on the grating is the complementary of the angle between both mirrors in the diffraction plane.

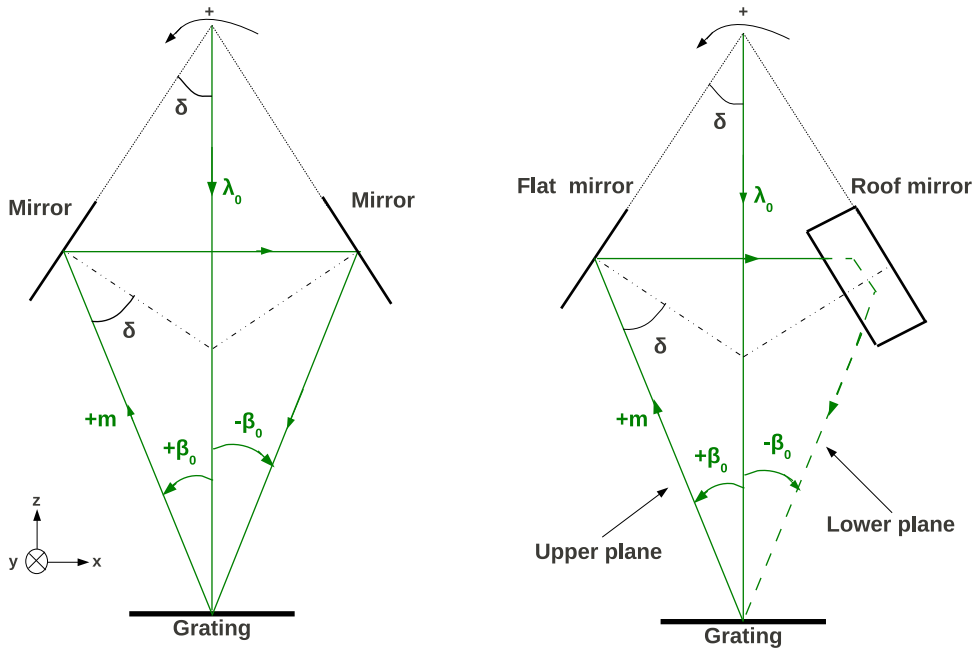

Figure 3.2: Geometry of an all-reflective SHS.

$$\beta = \frac{\pi}{2} - 2\,\delta$$

So the common path is obtained for one single exit angle that depends only of the orientation between both mirrors. For the HYPE-INSPIRE project, this angle has been fixed to $\beta_0 = 8.39°$ (Bétrémieux et al., 2010).

Heterodyne wavelength

Using the grating equation for normal incidence ($\alpha = 0$), one can define the heterodyne wavelength:

$$\lambda_0 = \frac{d \sin \beta_0}{m} \tag{3.1}$$

The heterodyne wavelength depends on the geometry of the system (tilt between both mirrors), the groove density of the grating and the diffracted order. For instance, HYPE-INSPIRE uses a symmetric grating in the first orders (± 1) with a groove density G of 1200 lines/mm. The numerical application of the equation (3.1) yields a heterodyne wavelength of $\lambda_0 = 121.592$ nm.

One has just shown, that after a first bounce on the grating, a monochromatic wave at the heterodyne wavelength is then reflected by both mirrors and comes back on the grating with an incidence angle equal to the exit angle of the first bounce. So, due to the symmetry of the grating equation, the second bounce on the grating

diffracts the light in the same direction as the incoming beam but in the opposite way.

Roof mirror

To avoid overlapping between incoming and outgoing beams, one introduces one roof mirror, as shown in Figure 3.2, so that the outgoing beams belong to a plane lower than the plane of the incoming beams. Although the beams do not overlap anymore, the denomination of common path remains adequate because the projections of the trajectories in the diffraction plane (plane xz) still overlap.

First bounce

Now we consider a wavelength different than the heterodyne wavelength. Because of the grating equation, a greater wavelength will be diffracted with a greater exit angle ($\beta > \beta_0$) as shown in Figure 3.3. Geometrical considerations demonstrate that, after reflections on both mirrors, the light-ray comes back on the grating with an incidence angle equal to $2\beta_0 - \beta$. This geometrical property is also true for wavelengths smaller than the heterodyne wavelength, that diffract after the first bounce on the grating with smaller exit angles.

It makes sense to define:

$$\Delta\beta \equiv \beta - \beta_0 \qquad \text{and} \qquad \Delta\lambda \equiv \lambda - \lambda_0$$

We have just shown that any light-ray diffracted by the grating with an exit angle of $\beta_0 + \Delta\beta$ comes back on the grating with an incidence angle equal to $\beta_0 - \Delta\beta$. For the first bounce, the grating equation is:

$$d \sin(\beta_0 + \Delta\beta) = m\,(\lambda_0 + \Delta\lambda) \tag{3.2}$$

Considering wavelengths close to the heterodyne wavelength ($\Delta\lambda \ll \lambda_0$) implies small angular variation ($\Delta\beta \ll \beta_0$). Then we may expand the grating equation at the first order and use the equation (3.1). It yields the offset from the heterodyne angle for the first bounce on the grating:

$$\Delta\beta \approx \frac{m\,\Delta\lambda}{d\cos\beta_0} \tag{3.3}$$

Second bounce

Now we want to estimate the angle ε at which this diffracted light leaves the grating after the second bounce. If the light-ray has been diffracted at the order +m at the first bounce, then we are interested by the order -m at the second bounce. Applying the grating equation with a proper use of the sign convention, we obtain:

$$\sin\varepsilon - \sin(\beta_0 - \Delta\beta) = -\frac{m\,(\lambda_0 + \Delta\lambda)}{d}$$

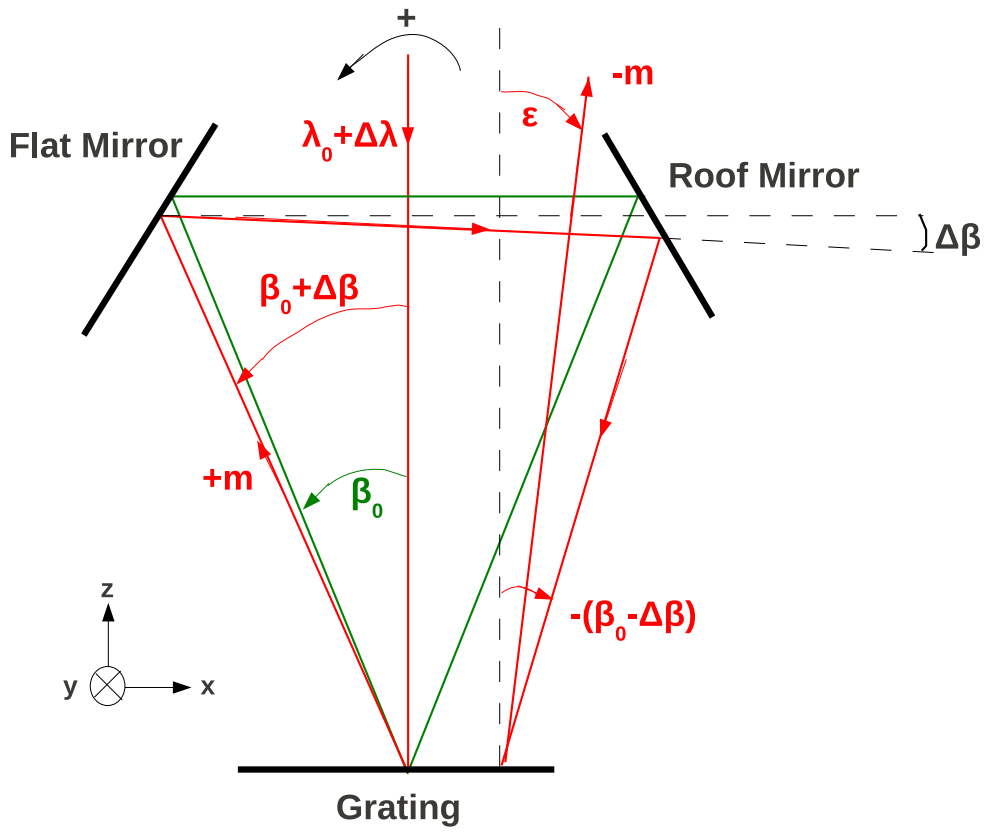

Figure 3.3: Geometry of the first bounce. The green lines correspond to the heterodyne wavelength, the red lines to a greater wavelength.

Combining with the equation (3.2) to replace the right-hand side, we obtain an exact relation for the exit angle:

$$\sin\varepsilon = 2\cos\beta_0 \sin\Delta\beta \tag{3.4}$$

Then we can expand at the first order and use the relation (3.3) to introduce the difference from the heterodyne wavelength. It yields the following approximation:

$$\varepsilon \approx -\frac{2\,m\,\Delta\lambda}{d}$$

At the first order, the exit angle from the SHS is proportional to the difference from the heterodyne wavelength. In the case of HYPE-INSPIRE, a wavelength difference of 0.009 nm yields a deviation of about 0.0012° by respect to the optical axis.

3.2.3 Interference fringes

Fringes localization

After the second bounce on the grating, the light-rays are diffracted by the opposite order of the first bounce and get out of the SHS. For the heterodyne wavelength, the wave-fronts exit parallel to the optical axis. For any other wavelength, both beams diverge from each other, whether the wavelength is smaller or larger than the heterodyne wavelength, as shown in Figure 3.4.

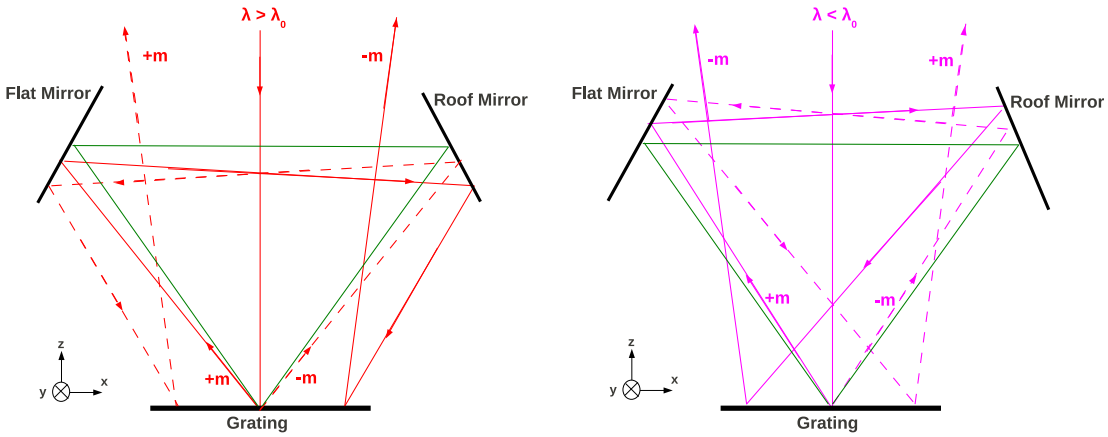

Figure 3.4: Exiting beams from the SHS. The green lines correspond to the heterodyne wavelength while the red and violet correspond, respectively, to greater and smaller wavelengths.

When looking at Figure 3.4, one realizes that the wavelengths $\lambda_0+\Delta\lambda$ and $\lambda_0-\Delta\lambda$ create the same pair of exiting beams. However there is a subtle difference that will be useful later. Indeed both orders can exit either on the side of the flat mirror or on the other side (roof mirror), depending on whether the considered wavelength is smaller or greater than the heterodyne wavelength. This can be expressed by the following approximation on the wave-vectors:

$$\mathbf{k}_m(\lambda_0 + \Delta\lambda) \approx \mathbf{k}_{-m}(\lambda_0 - \Delta\lambda)$$

The divergent beams appear to come from a virtual source located behind the grating. The location of this virtual sources depends on the geometry of the system and the grating. The distance has been calculated by Harlander (1991, pp.90-91) and is given by the following approximation:

$$z \approx -\frac{L}{2\cos^2(\beta_0)}$$

Where L is the average optical path length within the system for a wave-front at the heterodyne wavelength, i.e., the distance along the triangular path from the

grating center, to the first mirror, then the second mirror and finally back on the grating center. At the first order, the location of the virtual source is independent of $\Delta\lambda$.

Fringes frequency

After the second diffraction from the grating in the SHS, two slightly diverging beams tilted by 2ε by respect to each other exit from the system. This tilt induces an optical path difference. Since the two beams are coherent, the overlap of the beams create interferences and give rise to Fizeau fringes that are parallel to the grooves of the grating. In the x-direction (perpendicular to the grooves and the optical axis), the spatial frequency is given by:

$$f_x = \frac{2}{\lambda}\sin\varepsilon = \frac{4}{\lambda}\cos\beta_0 \sin\Delta\beta$$

Where the second equality has been obtained with the relation (3.4). Combining with the equation (3.3), it yields:

$$f_x \approx 4\frac{m}{d}\frac{\Delta\lambda}{\lambda} \tag{3.5}$$

As pointed previously, we observe that the wavelengths $\lambda_0 + \Delta\lambda$ and $\lambda_0 - \Delta\lambda$ produce the same spatial frequency of fringes. This symmetry creates an aliasing problem that will be addressed later in this section.

In the case of HYPE-INSPIRE, a separation of 0.009 nm from the heterodyne wavelength (121.592 nm) generates a spatial frequency of about 0.36 fringes per mm. It gives an order of magnitude however this is not an accurate value because it does not take into account the magnification by the output optics necessary to focus the light on the detector.

Let us define σ and σ_0 as the wave-numbers for the incoming monochromatic wave and the heterodyne wavelength, respectively. Then the previous approximation can be rearranged into a simpler and widespread expression for the fringe frequency:

$$f_x \approx 4\sin\beta_0\,(\sigma_0 - \sigma)$$

3.2.4 Resolving power, field of view and bandpass

Resolving power

For any spectrometer, the spectral resolution is defined by the ratio of the wavelength of interest over the minimal wavelength interval that can be resolved by the instrument:

$$R \equiv \frac{\lambda}{\delta\lambda}$$

For the SHS, two different wavelengths are distinguished by the number of fringes (n_f) produced across the detector. Hence the minimal wavelength interval changes

the number of fringes by one single fringe. The number of fringes is equal to the product of the fringe frequency by the beam width:

$$n_f = f_x W \approx 4\, m\, G\, W\, \frac{\Delta\lambda}{\lambda}$$

Where the approximation has been obtained with the relation (3.5), G=1/d is the groove density of the grating, and W is the width of the beam that illuminates the grating. $\Delta\lambda = \lambda - \lambda_0$ is the separation from the heterodyne wavelength and should not be confused with $\delta\lambda = \lambda' - \lambda$ which is the minimal separation between two wavelengths that can be resolved from each other by the SHS. Indeed $\delta\lambda = \Delta\lambda' - \Delta\lambda$. Then one can express the difference of one fringe between the patterns created by these wavelengths:

$$1 \approx 4\, m\, G\, W\, \frac{\delta\lambda}{\lambda}$$

Assuming that the detector captures the integrity of the outgoing beams, one can deduce the following expression for the resolving power of the SHS:

$$R \approx 4\, m\, G\, W$$

Another derivation has been made by Harlander (1991, pp. 36-37), considering the spectrum as the Fourier transform of the interferogram provided by the SHS. Theoretically, the SHS achieves the resolving power of the grating. With a beam width of 23.5 mm on the grating (Bétrémieux et al., 2010) and a groove density of 1200 line/mm, HYPE-INSPIRE could have a resolving power as high as 112,800.

Field of view

Enlarging the input aperture increases the sensitivity of the instrument because more light is admitted in the system. However this increase in sensitivity must be weighed against a reduction in fringe contrast resulting from the dependence of fringe frequency on off-axis angle. Similar trade-offs are encountered in the analysis of every spectroscopic system.

Harlander (1991, pp.40-43) derived the expression for the maximal field of view that can be accepted by the SHS without any loss in resolving power:

$$\Omega_m \approx \frac{2\,\pi}{R}$$

This relation expresses the fact that one can increase the field of view until the total number of fringes produced by the extreme rays differs by one from the number produced by the axial rays.

A more detailed calculation has been achieved by Chakrabarti et al. (1994), who made the distinction between the light entering in or out of the diffraction plane (plane xz in the figures). A Taylor expansion performed at the second order yields

an elliptical field of view with half-angles that can be related to the instrument resolving power R given by:

$$\theta_{IP} = \sqrt{\frac{2}{R}} \cos\beta_0 \qquad \theta_{OP} = \sqrt{\frac{2}{R}}$$

Where IP and OP refer, respectively, to the half-angles of the in-plane and out-of-plane field-of-views. Then one obtains a more accurate expression for the field of view that can be accepted by the SHS:

$$\Omega_m \approx \frac{2\,\pi \cos\beta_0}{R}$$

Contrarily to the resolving power that depends only on the grating properties, the field of view depends also on the geometry of the system, in particular the angle between both mirrors. In the case of HYPE-INSPIRE, the difference between the in-plane and out-of-plane half-angles is negligible ($\cos(8.39°) \approx 0.98$), so the field of view can be considered as circular. The half-angle is about 0.25°, so the field of view covers the apparent area of the Moon in the sky.

Bandpass

In the previous section, we demonstrated that the total number of fringes produced by the wavelength $\lambda_0 \pm \Delta\lambda$ is approximately equal to:

$$n_f \approx R\,\frac{\Delta\lambda}{\lambda} \approx R\,\frac{\Delta\lambda}{\lambda_0}$$

We consider a detector with N resolution elements (pixels). And we define k as the minimum number of pixels required to resolve one fringe. A hard limit, according to Nyquist sampling, is two pixels sampling the spatial region between two adjacent fringes, so k=2. Typical choices for k are either 2, 3 or 4.

Whatever the numerical value of k, the detector can distinguish a maximum of N/k fringes. Hence the useful bandpass is:

$$\Delta\lambda_B \approx 2\,\frac{N\,\lambda_0}{k\,R}$$

Theoretically, the bandpass results from a trade-off between the resolving power of the grating and the number of the detector pixels. In practice, the bandpass is significantly smaller because of distortion in the optics, the modulation transfer function of the detector pixels and the match of the pattern to the fixed pixel array (Hosseini et al., 2010). HYPE-INSPIRE uses a detector with 1,000 resolution elements. If we assume a value of k=4 to have some redundancy and be safe, we obtain an useful band pass of about 0.5 nm.

Wavelengths outside the bandpass produce fringes with spatial frequencies too high to obtain useful information. However they still contribute to the noise and must be filtered out (Bétrémieux et al., 2010).

3.2.5 Anti-aliasing

Problem to address

One major limitation in the current design is the symmetry of the system by respect of the heterodyne wavelength. There is no mechanism to tell the difference between $\lambda_0 + \Delta\lambda$ and $\lambda_0 - \Delta\lambda$, because these wavelengths produce the same interference pattern with the same number of fringes and are thus indistinguishable. This aliasing problem was present in the SCARI project (Chakrabarti et al., 1994; Stephan et al., 2001).

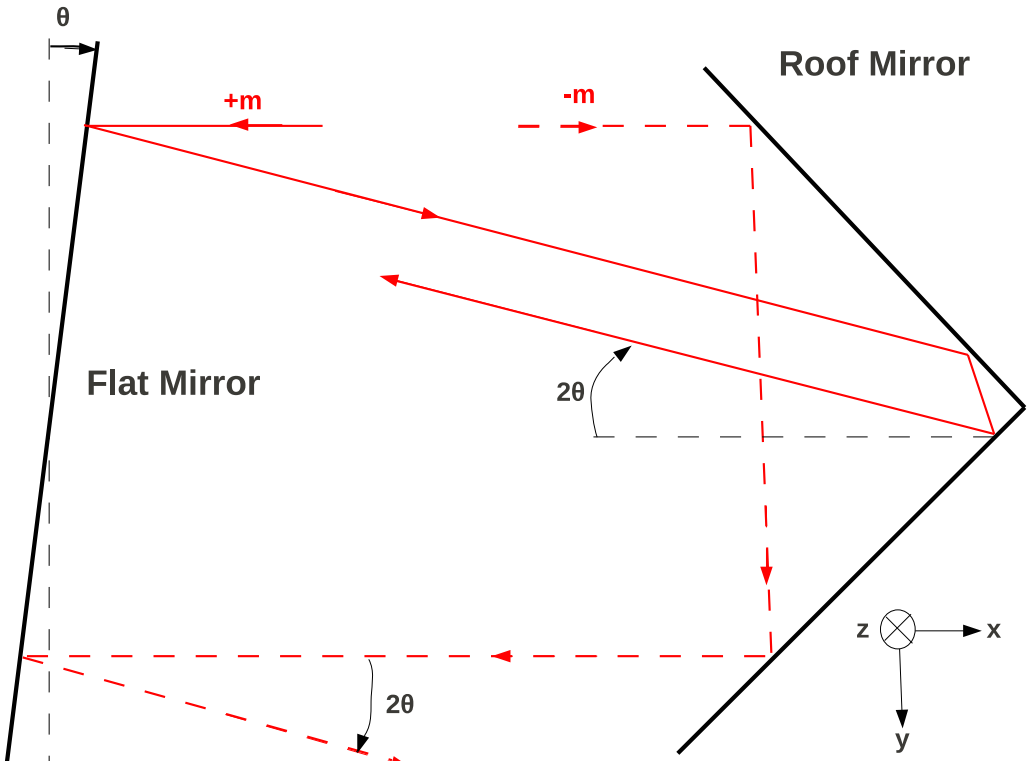

Figure 3.5: View of the mirrors in a plane parallel to the grating plane (xy). A tilt of the flat mirror induces a tilt of each order out of the diffraction plane (xz) but in opposite direction. For clarity, the angles and the distances have been exaggerated, the perspectives of the mirrors have not been rendered.

Tilt of the flat mirror

The confusion created by aliasing can be removed by breaking one symmetry of the system. A tilt of the flat mirror out of the plane of diffraction by an angle θ will result into a tilt of each order by an angle 2θ with respect to the plane of diffraction, but in opposite directions as shown in Figure 3.5. Hence the recombination of the beams create interference fringes that are parallel to the x-direction, which is perpendicular

to the grooves and to the optical axis. The spatial frequency along the y-direction is given by:

$$f_y = \frac{2}{\lambda}\sin(2\theta)$$

Now, even the central wavelength produced fringes, as shown in Figure 3.6 that displays a ZEMAX model of the fringes produced by a collimated beam penetrating the SHS component of HYPE (Bétrémieux et al., 2010).

Rotation of the fringes

Let us define the north as the direction of negative y, and the east as the direction of positive x (toward the roof mirror). We have just shown that the order +m will be north-bound because of the tilt of the flat mirror. Moreover we also previously showed that the order +m of the wavelength $\lambda_0 + \Delta\lambda$ exits the SHS in the west direction, while the order -m will be east-bound (see Figure 3.4). The combination of both tilts result into the order +m being orientated toward north-west, while the order -m will be south-east. The fringes are perpendicular to the difference of the wave-vectors, so the fringes will be orientated along an axis that goes from south-west to north-east.

A similar reasoning with the wavelength $\lambda_0 - \Delta\lambda$ shows that the fringes will be orientated along an axis that goes from south-east to north-west. Hence the tilt of the flat mirror results into a rotation of the fringes, but in different directions, depending on whether the considered wavelength is smaller or greater than the heterodyne wavelength.

3.2.6 Intensity distribution

Imaging of the fringes

Since the exiting beams from the SHS diverge from each other, an imaging mirror is required to image the fringes onto a detector. Hence the fringe frequency at the detector is actually a factor 1/M greater than in the SHS fringe plane (which is virtually located behind the grating), so $f'_x = f_x/M$ and $f'_y = f_y/M$, where M is the transverse magnification of the imaging mirror.

The transverse magnification is given by M=i/o, where o is the distance from the virtual fringes to the imaging mirror, and i is the distance from the imaging mirror to the re-imaged fringes on the detector

Intensity distribution

Ignoring instrumental efficiencies and vignetting, the intensity distribution I(x,y) on the detector is given by:

$$I(x,y) = \int_0^\infty B(\lambda)\left[1 + \cos\left\{2\,\pi\,x\,f'_x(\lambda) + 2\,\pi\,y\,f'_y(\lambda) + \frac{2\pi}{\lambda}\Delta L\right\}\right] d\lambda$$

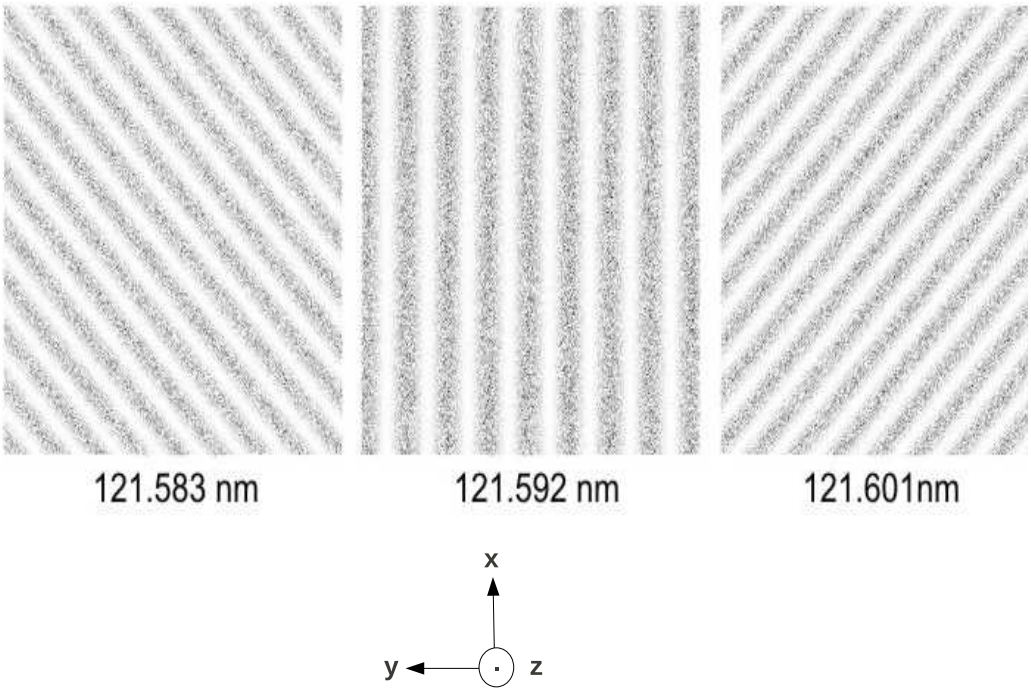

Figure 3.6: ZEMAX model of fringes produced by an SHS with an input collimated beam at three different wavelengths. The diffraction plane (xz) is along the vertical and perpendicular to the plane of the figure. A slight tilt outside the diffraction plane by 0.0008° of the flat mirror causes fringes to produced parallel to the x-direction for the heterodyne wavelength of 121.592 nm. The other two wavelengths, which are both 0.009 nm away from the heterodyne wavelength, produce fringes tilted by about 45° in opposite direction and can be thus distinguished without any ambiguity. Figure adapted from Bétrémieux et al. (2010).

where $B(\lambda)$ is the spectrum of the source and ΔL is the path length difference between the two orders of the SHS.

The additional phase term due to ΔL was an issue for the SHS on board SCARI, because path lengths were unequal for both orders, providing a non-zero and wavelength-dependent phase-shift. On HYPE, the use of a roof mirror allows to center the input and output beams on the grating center, hence both arms of the SHS are of the same length ($\Delta L = 0$).

Then all wavelengths constructively interfere along the central line (x=0), creating a bright pole that can be useful when aligning the SHS. Moreover the interferogram becomes complete (Bétrémieux et al., 2010).

3.3 Polarimetry measurements

3.3.1 State of the art

Predictions of the polarization of the IPH

Brandt & Chamberlain (1959) first suggested the importance of polarization measurement of the interplanetary Lyman-α radiation, and provided an analytical expression of the polarization from a hydrogen atom illuminated by solar Lyman-α:

$$P(\theta) = \frac{I_\perp - I_\parallel}{I_\perp + I_\parallel} = \frac{0.2 \sin^2\theta}{1 - 0.2(\frac{1}{3} - \sin^2\theta)}$$

where θ is the scattering angle, $I_\perp$ and $I_\parallel$ are the components of the radiation field that are respectively perpendicular and parallel to the plane of scattering (Sun - hydrogen atom - observer). The polarization of an individual hydrogen atom varies from 0% at 0° and 180° scattering angles, to 27% at 90°.

Ajello & Thomas (1985) extended this expression to a distribution of hydrogen atoms, by letting $I_\perp$ and $I_\parallel$ be replaced by the integrated intensities for each polarized components of the radiation field, yielding:

$$P(\theta) = \frac{0.2 \int_0^\infty \sin^2\theta(s)\, g(s)\, N(s)\, ds}{\int_0^\infty [1 - 0.2(\frac{1}{3} - \sin^2\theta(s))]\, g(s)\, N(s)\, ds}$$

where s is the distance along the line of sight, N(s) is the number density at position s, and g(s) is the scattering rate at position s, as given by Ajello (1978):

$$g(s) = g_e \frac{r_e^2}{r^2(s)}$$

where r_e is the radial distance from the Sun to the Earth (1 AU), $r(s)$ is the radial distance from the Sun to the scattering point, and g_e is the scattering rate at 1 AU at solar line center.

Polarimetry measurements at Ly-α

Experimentally, measurements of the polarization and interplanetary Lyman-α were reported by Blamont et al. (1975), Emerich et al. (1976) and Cazes & Emerich (1977), using LiF polarization analyzers on the French D2-A satellite. Cazes & Emerich (1977) found a polarization of about 10% in the ecliptic plane for an April 1971 observation at 90° from either side of the Sun.

It is worth noting that other polarimetric experiments have been conducted, either at Ly-α on other targets, or at different wavelengths in the ultraviolet range. For instance, Stenflo et al. (1976, 1980) flew a Swedish-built spectro-polarimeter on the Soviet satellite Intercosmos-16 in 1976 and reported a polarization rate of 1% in the Ly-α solar limb.

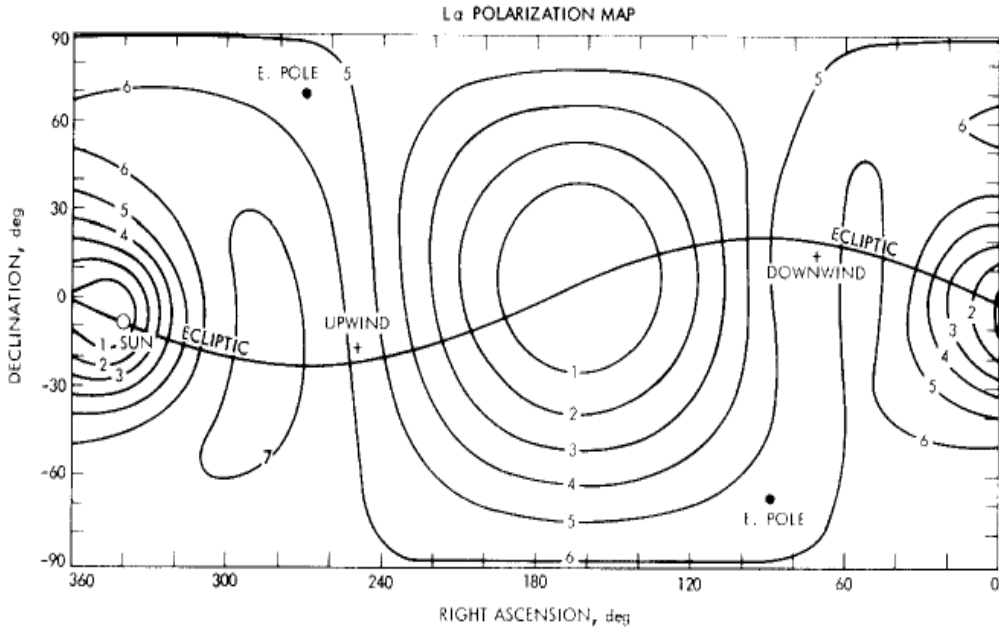

Figure 3.7: From Ajello & Thomas (1985).

Polarimetry in the ultraviolet

The Solar Maximum Mission (SMM) spacecraft was launched in 1980 to investigate solar phenomenon, particularly solar flares. Among other instruments, it carried the Ultraviolet Spectrometer and Polarimeter (UVSP), which used a rotatable retarder into the spectrometer beam for measurement of Zeeman splitting and linear polarization in the transition region and chromosphere (Woodgate et al., 1980).

Polarimetric images have been also obtained by the Space Astronomy Lab at the University of Wisconsin. A sounding rocket payload, the Wide-Field Imaging Survey Polarimeter (WISP), had flown successfully four times, targeting the Pleiades Reflection Nebula, the Large Magellanic Cloud, comet Hale-Bopp and the diffuse light of our Galaxy (Nordsieck & Harris, 1999). The WISP design consists of a Schmidt telescope, a rotatable stressed CaF_2 waveplate and a fixed polarizing mirror illuminated at the Brewster angle.

3.3.2 Basics of polarimetry

Polarization and Stokes parameters

Polarization is a property of certain waves (mainly electromagnetic waves and gravitational waves), describing the orientation of their oscillations. Acoustic waves do not have polarization because the direction of vibration and direction of propagation are the same. For electromagnetic waves, the polarization can be fully described by

the oscillations of the electric vector (e.g., Rybicki & Lightman, 1979, pp. 62-69).

First let us define the quasi-monochromatic waves, as a generalization of monochromatic waves, with an electric vector equal to:

$$\mathbf{E} = \left[E_1(t)\, e^{i\phi_1(t)}\, \mathbf{x} + E_2(t)\, e^{i\phi_2(t)}\, \mathbf{y}\right]\, e^{-i\omega t}$$

where the amplitudes and the phases possess a relatively slow time. It means that over short times (of order $1/\omega$), the wave looks like a monochromatic wave, but is no longer monochromatic over much longer times. For quasi-monochromatic waves, the Stokes parameters are defined as:

$$\begin{aligned} I &\equiv \left\langle E_1^2 + E_2^2 \right\rangle \\ Q &\equiv \left\langle E_1^2 - E_2^2 \right\rangle \\ U &\equiv \left\langle 2E_1 E_2 \cos(\phi_1 - \phi_2) \right\rangle \\ V &\equiv \left\langle 2E_1 E_2 \sin(\phi_1 - \phi_2) \right\rangle \end{aligned}$$

It can be shown that:

$$I^2 \geqslant Q^2 + U^2 + V^2$$

where the equality holds for a completely elliptical polarized wave (e.g. a monochromatic wave).

The Stokes parameters are additive for a superposition of independent waves. With this superposition principle, one can represent any wave as the sum of a polarized wave and an unpolarized wave, where the intensity of the unpolarized wave is equal to $I - \sqrt{Q^2 + U^2 + V^2}$. And one defines the *degree of polarization* as:

$$\Pi = \frac{\sqrt{Q^2 + U^2 + V^2}}{I}$$

Pure elliptical polarization is determined solely by three parameters that are directly related to Q, U and V:

$$\begin{aligned} E_{pol}^2 &= \sqrt{Q^2 + U^2 + V^2} \\ \sin 2\beta &= \frac{V}{\sqrt{Q^2 + U^2 + V^2}} \\ \tan 2\chi &= \frac{U}{Q} \end{aligned}$$

where E_{pol} is the amplitude of the electric vector of the polarized wave, β describes the ellipticity of the polarization state (in particular, $\beta = 0$ or $\pm\pi/2$ for linear polarization, and $\beta = \pm\pi/4$ for circular polarization), and χ measures the orientation of the ellipse relative to the x-axis.

The polarimetric technique

The basic polarimetric technique consists in obtaining spectra or images of the source at four different orientations (0°, 45°, 90°, 135°) of the polarizer. These measurements (I(0), I(45), I(90) and I(135)) are combined to compute the Stokes parameters Q and U, normalized by the intensity I, and given by:

$$\frac{Q}{I} = \frac{I(0) - I(90)}{I(0) + I(90)} \qquad \text{and} \qquad \frac{U}{I} = \frac{I(45) - I(135)}{I(45) + I(135)}$$

from which Π_{lin} (the degree of linear polarization) and χ can be derived by:

$$\Pi_{lin} = \sqrt{\left(\frac{Q}{I}\right)^2 + \left(\frac{U}{I}\right)^2} \qquad \text{and} \qquad \tan(2\chi) = \frac{(U/I)}{(Q/I)}$$

For HYPE-INSPIRE, four interferograms will be obtained. With a two-dimensional inverse-Fourier transform, these interferograms will be converted into spectra from which the Stokes parameter can be then computed.

The Brewster effect

The Brewster effect is a particular phenomenon that happens at a boundary between two media. Under certain circumstances, the coefficient of reflection for light polarized parallel to the boundary becomes null.

Akhmanov & Nikitin (1997, pp. 395-396) gives a physical explanation of the Brewster effect, based on the Fresnel formulae for the reflection of light at a boundary between two media:

$$r_\perp = \frac{\sin(\theta_1 - \theta_2)}{\sin(\theta_1 + \theta_2)} \qquad \text{and} \qquad r_\parallel = -\frac{\tan(\theta_1 - \theta_2)}{\tan(\theta_1 + \theta_2)}$$

where the symbols $\perp$ and $\parallel$ denote respectively the directions perpendicular and parallel to the boundary between both media (referred by the indexes 1 and 2), θ_1 is the angle of incidence while θ_2 is the angle of refraction. It becomes obvious that the coefficient of reflection $r_\parallel$ becomes null when the angles θ_1 and θ_2 are complementary. Both angles are also related to each other by the law of refraction (Snell's law):

$$n_1 \sin\theta_1 = n_2 \sin\theta_2$$

where n_1 and n_2 are the refractive indices of each medium. One can deduce the Brewster angle, for which the coefficient of reflection $r_\parallel$ is null:

$$\theta_B = \arctan\left(\frac{n_2}{n_1}\right)$$

When non-polarized light falls at this angle, the reflected beam is linearly polarized in the direction perpendicular to the plane of incidence. For instance, the polarimeter on HYPE-INSPIRE uses a piece of polished diamond which has a Brewster angle of about 73.1° at Lyman-α.

Light polarization control

Akhmanov & Nikitin (1997, chap. 21) is an useful reference to understand the optics of anisotropic media, in particular the properties of birefringence. The main feature in anisotropic crystals is that an optical wave with an arbitrary polarization state splits into two linearly polarized waves with orthogonal polarization directions, each travelling at a different velocity.

The physical interpretation of this phenomenon is that the anisotropy of the crystal makes the electrons move predominantly along a definite direction with respect to the crystal axis. The crystal lattice will then have a more or less strong interaction with the light depending on the polarization state. This results into an anisotropy of the dielectric permittivity tensor (e.g. $\varepsilon_{xx} \neq \varepsilon_{yy} \neq \varepsilon_{zz}$ for a biaxial crystal).

For an uniaxial crystal ($\varepsilon_{xx} = \varepsilon_{yy} \neq \varepsilon_{zz}$), one defines two principal refractive indices:

$$n_o = \sqrt{\varepsilon_{xx}} = \sqrt{\varepsilon_{xx}} \qquad \text{and} \qquad n_e = \sqrt{\varepsilon_{zz}}$$

where the subscripts "o" and "e" denote respectively the ordinary and extraordinary modes. An ordinary wave is polarized in the plane xy. For positive uniaxial crystals ($n_o < n_e$), the ordinary wave is faster. A direct application of this property consists of special plates of anisotropic crystals, so-called quarter-wave and half-wave plates. If the optic axis of the crystal is parallel to the face illuminated by a plane monochromatic wave, the difference of refractive indexes creates a phase shift between the ordinary and extraordinary waves:

$$\Delta\varphi = \frac{2\pi}{\lambda}(n_o - n_e)d$$

where λ is the wavelength and d is the thickness of the plate. By choosing the thickness of the plate such that $\Delta\varphi = \pi$, one obtains a half-wave plate that flips the axis of linear polarization of the light by respect to the fast axis of the plate.

3.3.3 Design of the polarimeter

The design of the polarimeter on HYPE-INSPIRE, described in details by Bétrémieux et al. (2010), has been directly inspired by the one on board of the Far-Ultraviolet Spectro-Polarimeter (FUSP; Nordsieck et al., 2003).

This polarimeter is a pre-filter to the SHS: it uses a half-wave plate in lithium fluoride (LiF) and places a Brewster mirror at the telescope focus, as show in Figure 3.8. Spatial constraints only allow an incidence angle as small as 76°, so slightly higher than the Brewster angle (about 73.1°), which results into a degree of polarization of about 96% for the reflected beam.

By looking into the reverse direction to the light propagation in the instrument, one realizes that the half-wave plate flips the polarization axis of the Brewster mirror, as it maps back onto the sky. If the fast axis of the half-wave plate is inclined

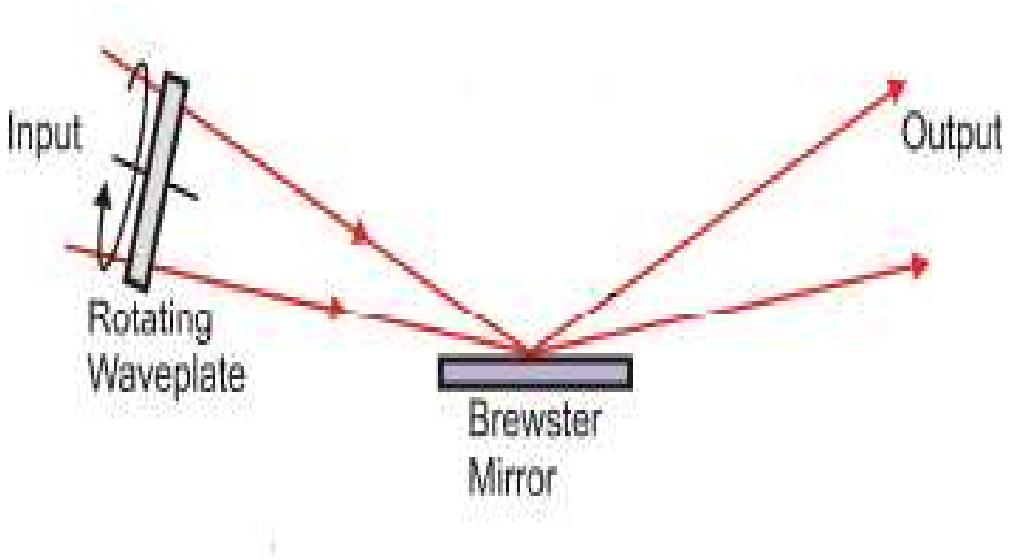

Figure 3.8: Optical layout of the HYPE-INPIRE polarimeter. The telescope focuses the beam onto the diamond Brewster mirror. The rotation of the Li-F half-wave plate rotates the mapping of the polarization plane of the Brewster mirror back onto the sky. The figure is a courtesy of Walt Harris.

with an angle θ by respect to the polarization axis of the Brewster mirror, then this polarization axis will map back to the sky with a rotation of 2θ around the propagation direction. Hence, one can sample different angles of linear polarization.

The rotating half-wave plate has to be located prior to the Brewster mirror. Indeed the incident light on the grating in the SHS must be polarized parallel to the grooves axis (or perpendicular to the diffraction plane) in order to optimize the throughput.

3.4 Payload design

3.4.1 Optical layout and imaging

Optical layout of the instrument

HYPE is a complex instrument which has been modelled in ZEMAX (Bétrémieux et al., 2010). It combines a SHS with a polarizer, previously described, through a system that allows one-dimensional imaging along the axis perpendicular to the diffraction plane of the grating, so parallel to the grooves of the grating (y-direction). Figure 3.9 shows the optical layout of the instrument.

The telescope belongs to the class of Cassegrain reflectors: it combines a primary concave spherical mirror with a secondary asphere convex mirror. This telescope

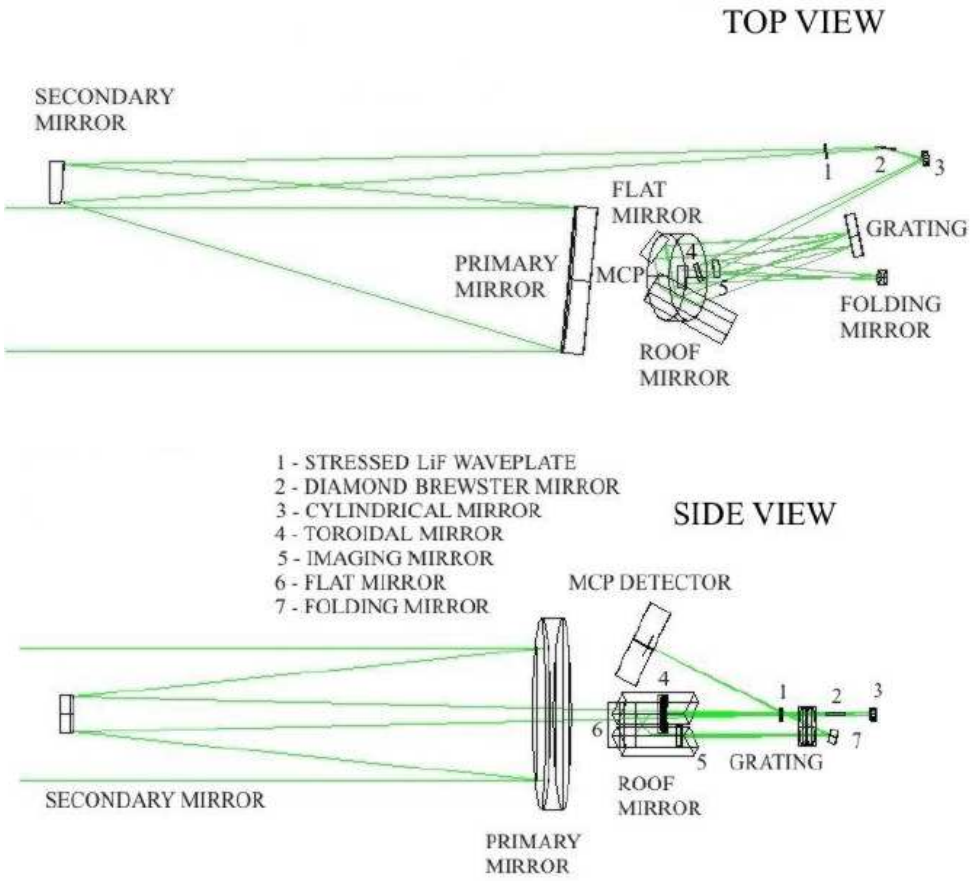

Figure 3.9: Optical layout of the payload. Figure from Bétrémieux et al. (2010).

focuses the light through the LiF half-wave plate onto the diamond Brewster mirror. The diverging polarized beam then encounters a cylindrical mirror and a toroidal mirror, prior to entering the SHS.

One-dimensional imaging

The cylindrical mirror only affects the imaging direction (y-direction). The toroidal mirror collimates the beam in the direction perpendicular to the grooves (x-direction). The association of both mirrors focus the beam on the grating along the imaging direction.

Upon exit of the SHS, a concave parabolic mirror re-images the fringes (x-direction) and the sky (y-direction) onto a micro-channel plate detector.

3.4.2 Detector

HYPE uses a detector manufactured by Siegmund Scientific Corporation (SSC). This detector combines a Z-stack of three micro-channel plates with a caesium iodide (CsI) photocathode and a double delay line anode.

Micro-channel plate

A micro-channel plate (MCP) is a planar component used for detection of particles (electrons or ions) and impinging radiation (ultraviolet radiation and X-rays).

A MCP is essentially a small, thin disk with numerous microscopic channels running parallel to each other from one face of the disk to the other, as shown in Figure 3.10. Channel axes are typically normal to, or biased at small angle ($\sim 8°$) to the MCP input surface. The channel matrix is usually fabricated from a lead glass, treated in such a way as to optimize the secondary emission characteristics of each channel and to render the channel walls semiconducting so as to allow charge replenishment from an external source (Wiza, 1979). Each tiny channel (or pore) acts like a electron multiplier tube since electrons hitting the walls eject additional electrons resulting in a cascade of electrons.

A photocathode on the top of the MCP allows the conversion from light to electrons. Materials such as CsI, CsTe or KBr have good ultraviolet (UV) quantum efficiency and are almost solar-blind with a very low response to visible photons. For one incident UV photon, a charge cloud of 500,000 electrons can emerge from one channel and can therefore be detected or counted. Various anode structures or solid-state devices can be placed below the MCP to act as readouts (McLean, 2008).

Delay line anode

In a delay line, the charge cloud from the MCP strikes an anode structure and two pulses begin to propagate in opposite directions. The event location is deduced from the difference in arrival times at the ends. A double delay line with outputs at each corner is used with the MCPs on GALEX (Siegmund et al., 1999).

Such readout structures require very large gain, so they employ not one but several MCPs in a stack called a "Z-stack". A stack of three MCPs can provide a gain of 2×10^7 electrons, which is needed for a delay line to give a spatial resolution of about 25 microns.

Disadvantages and constraints

MCPs suffer from "gain sag" due to the inability of the channels to replenish the charge extracted in time for the next pulse. Consequently, a second event arriving within the charge cloud radius while some lower channels are still depleted of charge will experience less gain.

The length of a microchannel is typically 50-100 times the diameter of the channel, which implies a large surface-to-volume ratio and the tendency to trap residual gas unless exceptional measures on cleanliness and plate conditioning are employed.

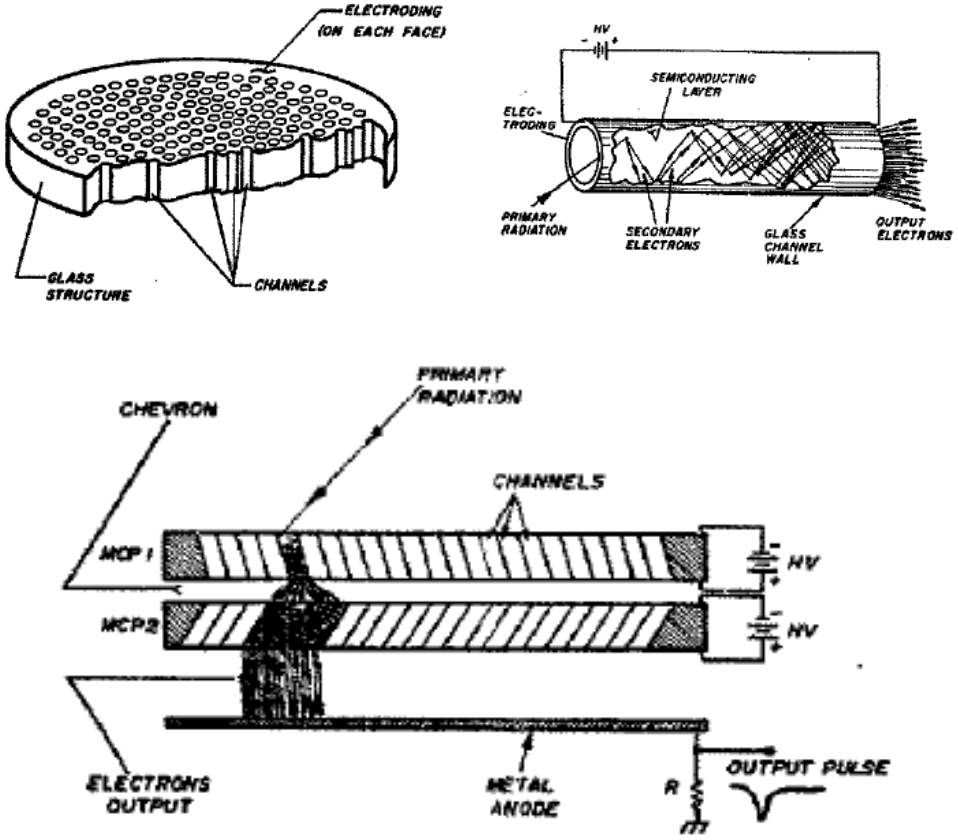

Figure 3.10: *Top-left:* Cutaway view of a microchannel plate. *Top-right:* Cutaway view of a straight channel electron multiplier. *Bottom:* Side view of a Chevron operation, two MCPs rotated from each other form a chevron (v-like) shape. Figures from Wiza (1979).

Because MCPs are operated at potentials of a few thousand volts, residual gases can lead to destructive discharges. In the case of HYPE-INSPIRE, a small vacuum pump will be installed in the payload in order to maintain a sufficiently low pressure.

The use of high-voltage (HV) power supply for the MCPs represents another danger in an evacuated payload, because this is a possible source of electrical arcing, especially around the pressure of 10^{-5} Torr. Such discharges can damage the payload, including the rest of the electronics. This is why the HV power supply must be carefully isolated.

3.4.3 Mechanical structure and electronics

Mechanical structure

The HYPE-INSPIRE experiment can be decomposed in two parts: the telescope and the combination SHS-polarimeter (SHSPOL). The whole instrument is self-contained in an isolated evacuated 22" diameter skin section with the telescope and SHSPOL on either side of an internal bulkhead plate, as shown in Figure 3.11.

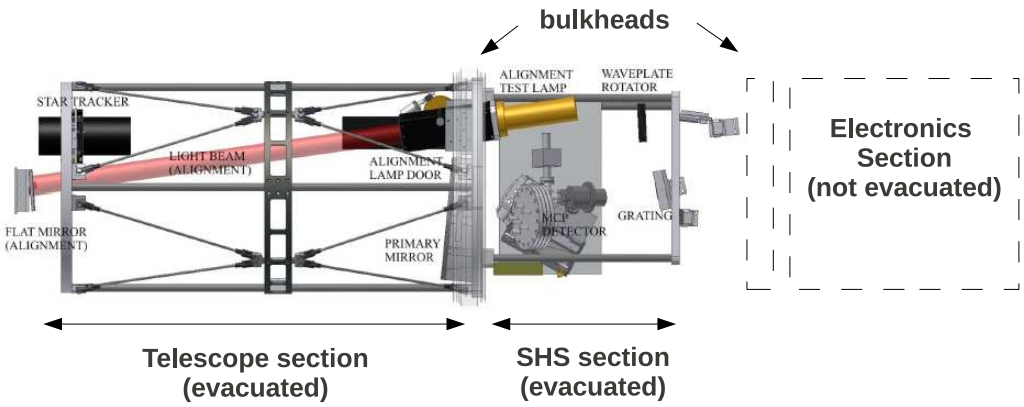

Figure 3.11: Mechanical structure of the payload. The length of the evacuated sections (telescope and SHS) is about 48", so about 1.2 m. The diameter is 22", so about 66 cm. The electronics section is not to scale. Figure adapted from Bétrémieux et al. (2010).

The aft facing bulkhead is to be a standard vacuum-sealed aperture door that opens during flight, while the forward facing bulkhead serves as an interface into an electronics section house. Also housed in the electronics section bulkhead will be a vacuum flange through which the payload will be continually pumped out until just prior to launch.

Electronics

Figure 3.12 represents schematically the electronics within the payload. The telemetry rate will be about 2 megabytes per second (MB/s).

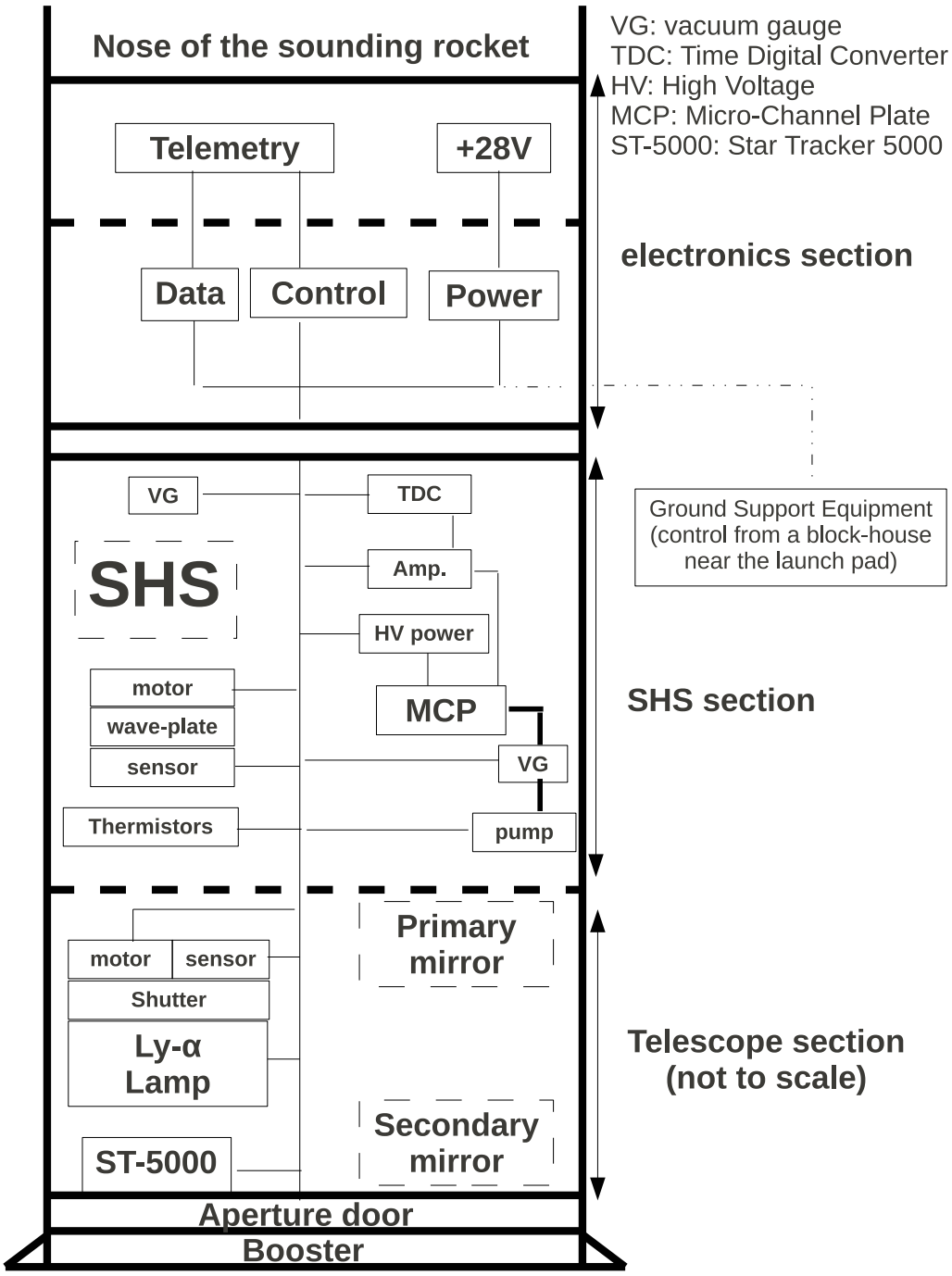

Figure 3.12: Schematic of the electronics. Figure made with the assistance of Loan-anh Nguyen.

Chapter 4

Experimental challenges

In the context of the HYPE-INSPIRE project, we met several experimental challenges. First, I will review common problems to astronomical applications in the vacuum ultra-violet range.

Then I will present how we identified and treated an efficiency anomaly on a diffraction grating, in the second section which is an adapted version of the work published by Vincent et al. (2011b). Finally I will present the next steps for the HYPE-INSPIRE project.

4.1 The vacuum-ultraviolet range

4.1.1 Choice of optics

Flatness

Optical components need to be carefully polished in order to limit the scattering of light by the roughness of the surface. So one needs to optimize the wave-front flatness, which is expressed as λ/n with $\lambda = 632.8$ nm (wavelength of a helium-neon laser).

A wave-front flatness of $\lambda/5$ or $\lambda/2$ seems to be common for applications in the visible range. However this may not be good enough for the ultraviolet range: for instance, the Ly-α wavelength is smaller by a factor 5 than the He-Ne wavelength, so a better flatness is required in order to reach a minimal efficiency which is necessary for the success of the project.

For the HYPE-INSPIRE project, the manufacturer (Jobin-Yvon) was asked to reach a flatness of $\lambda/20$ for the diffraction grating, which is at the limit of the feasibility ("best effort value").

Coatings

Typically, diffraction gratings are produced either by ruling or by holography. Then they are coated with aluminium (Al) and magnesium fluoride (MgF_2). Mirrors re-

ceive a similar treatment. Aluminium allows to reach high efficiencies, unfortunately it gets oxidised over time, so it requires a protective layer of magnesium fluoride.

For diffraction gratings, the thickness of the MgF_2 is especially critical, as it will be explained in the section 4.2.

4.1.2 Working under vacuum

Units of pressure

Common units of pressure are the bar and the Torr. The atmospheric pressure is at 1.01 bar or 760 Torr.

Vacuum systems

A basic vacuum system consists of a vacuum chamber and vacuum pumps. The vacuum chambers have a wide range of dimensions: the average size is of the order of the meter.

Bringing the system to a low pressures require the combination of different pumps. Typically a rough pump to reach pressures of the order of 10^{-1} Torr (about 4 orders of magnitude below atmospheric pressure), and a turbo pump to go down to 10^{-6} Torr and below. Vacuum grease is usually applied to the flanges, in order to maintain a good seal and limit the leaks.

Cycling a vacuum chamber is time-consuming, so any set-up requires anticipation and a proper design in order to reduce the time losses.

Cleanliness

Cleanliness should be the norm when working in the lab. Vacuum systems are very sensitive to any kind of dirt, because any residual on a piece of equipment will out-gas when submitted to low pressures. This out-gassing represents a source of contamination for the whole system and is a real concern for the experimentalist who needs to operate under vacuum. Oil may be the worst enemy when working in the ultraviolet range: illuminated by ultraviolet radiation, it will have chemical reactions and become opaque, resulting into a complete loss of efficiency for the contaminated optical components.

Unfortunately for the optical components, the human skin is covered of oil. When working with a piece of equipment that will go into the vacuum system, the operator need to wear latex gloves to handle the piece. Indeed gloves should be used for the handling of any optical component, even in the visible range. Certain operations, as leaning over the vacuum tank to manipulate an optical component, are more critical, so they require the use of a mask, a bouffant cap and a coat to avoid any contamination, as the drop of a single hair.

Handling precautions may not be enough and some pieces need some cleaning in order to be *vacuum-compatible*. A basic cleaning consists of alcohol and acetone. Acetone can break the bonds of oil, and alcohol can remove the residuals. Thorough

cleaning requires a bath of ultrasound, similarly to a washing-machine where the acetone plays the role of the soap and the ultrasound creates the cyclic vibrations.

The highest level of cleanliness requires the use of a clean-room which is kept at positive pressure (greater than environment pressure), so the air is pushed out of the room. To give perspective, the ambient air outside in a typical urban environment contains 8,000,000 particles with a diameter of 1 μm or greater in a volume of 1 cubic meter, corresponding the ISO 9 clean-room. For the HYPE-INSPIRE project, we are using a ISO 6 clean-room [1], which allows only 8,000 particles with a diameter greater than 1 μm in a volume of 1 cubic meter. An ISO 1 clean room allow no particle with a diameter greater than 0.3 μm. Obviously, the operator needs to be appropriately dressed when entering the clean room.

Magnesium fluoride coatings can be damaged by moisture, so this kind of optics must be handled carefully and must be kept safely in desiccators which allow to reduce the humidity and provide a dry environment.

4.1.3 Constraints in space applications

Because of the absorption by the Earth's atmosphere, observations of ultraviolet astronomical sources can not be done from the ground. Depending on the wavelength range and the budget, instruments need a platform like a balloon, a sounding-rocket, a satellite or a spacecraft.

Examples

It is difficult to make an exhaustive list of space missions which made ultraviolet observations. However it may be really useful to know the different milestones in the space exploration.

The International Ultraviolet Explorer (IUE) is clearly a milestone: the concept was initially proposed in 1964, the satellite was launched in 1978 and operated until 1996. The Solar Maximum Mission (SMM) satellite was launched in 1980 and operated until 1989.

Launched with HST in 1990, GHRS on-board of HST took the relay of IUE and was then replaced by STIS in 1997. The Far Ultraviolet Spectroscopic Explorer (FUSE) was launched in 1999, giving access to wavelengths below 115 nm until its termination in 2007. The Cosmic Origins Spectrograph (COS) was installed in 2009 on HST: COS has a narrowed bandpass and a lower resolution than STIS but it is many times more sensitive.

All these experiments had to minimize the number of optics to compensate for the reflectivity and transmission efficiencies which are quite low compared to what is common at visible wavelengths.

[1] The ISO 6 clean-room is also referenced as a class 1,000 clean-room in the US FED STD 209E standard (which is technically obsolete but still widely used).

Specificities of a sounding-rocket flight

A sounding rocket flight reaches intermediate altitudes (300 km) between balloon experiments (up to 50 km) and satellites (800 km and above). It is also less expensive than a satellite, so it can be a first step to prove the feasibility of an instrument concept before going toward a larger scale project as a satellite or a spacecraft.

The principal inconvenience is the limited amount of integration time for observations, typically 5 minutes above 120 km which is the minimal altitude to detect Ly-α radiation from outside the geocorona. This time constraint creates another difficulty in addition to the relatively low efficiencies due to the ultraviolet range.

This is why the instrument has to be seriously optimized in order to obtain data with an interesting signal-to-noise ratio. In the context of the HYPE-INSPIRE project, we met an unexpected low efficiency in the diffraction grating, which was representing a serious problem for the success of the project.

4.2 Efficiency anomaly on a diffraction grating

4.2.1 Context

The use of gratings for symmetric dispersion, where both positive and negative orders are diffracted (symmetric blaze gratings), is an uncommon implementation but one that is employed in specialized astronomical instrumentation including dual order spectrographs (McCandliss et al., 2001) and all-reflective spatial heterodyne spectrometers (Harlander, 1991; Chakrabarti et al., 1994; Bétrémieux et al., 2010). These implementations require illumination at normal incidence in order to produce two beams with comparable intensity and dispersion. This configuration is often not tested experimentally for commercial gratings where the desire for high efficiency in a single order is the primary goal.

We report here efficiency testing of a normal incidence dual-order efficiency testing of an Al-MgF_2 coated holographic grating with a trapezoid profile optimized to 121.6 nm. Both the grating and coating were provided by Horiba Jobin-Yvon (HJY) in support of HYdrogen Polarimetric Explorer (HYPE-INSPIRE) experiment, a sounding rocket experiment developed in cooperation between NASA and the Centre National d'Etudes Spatiales (CNES). Our tests revealed an anomaly that was sharply peaked at normal incidence that was not predicted by industry-standard theoretical models. The anomaly resulted in a 50% reduction in the efficiency into each of the m = +/- 1 orders of the grating. Our mitigation strategy for this involved over-coating the grating, using an optimized Al-MgF_2 mix developed by the Goddard Space Flight Center (GSFC) for the UV gratings used in the Cosmic Origins Spectrograph on the Hubble Space Telescope. After re-coating the anomaly was eliminated, but at a cost of a reduction of 30% in the peak efficiency of the symmetric orders and an increase in grating specular (zero-order) reflection.

After an overview of grating anomalies and a presentation of the instrument, we discuss the respective roles of the new coating characteristics and the effect of

groove smoothing from repetitive overlays in the observed changes in the grating performance.

4.2.2 Generalities on gratings

Different textbooks or seminal papers (e.g., Petit, 1980; Maystre, 1984; Loewen & Popov, 1997) are really useful for the reader interested in the understanding of physical processes that take place in a diffraction grating.

Groove profile

Figure 4.1 shows the groove profile of a trapezoidal grating. This profile is defined by the following parameters:

- d: the groove period
- h: the groove depth
- c: the groove width at half-depth
- θ: the trapeze angle

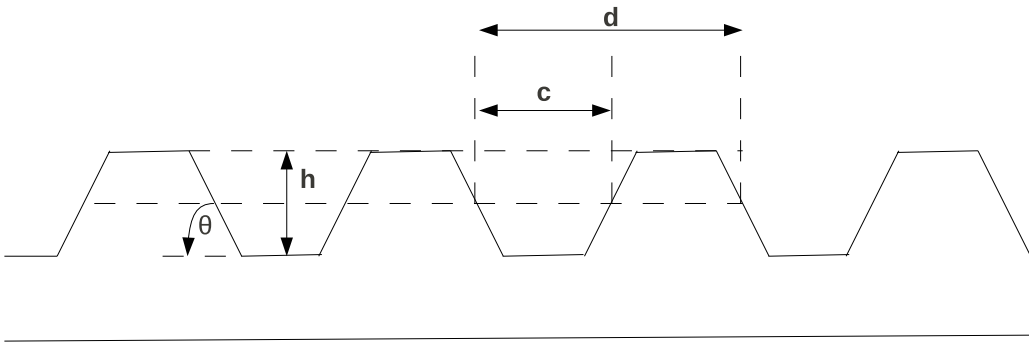

Figure 4.1: Groove profile of a diffraction grating.

Grating equation

The famous property of gratings to diffract incident light into clearly distinguished directions is expressed in a simple equation, called the grating equation:

$$\sin\alpha + \sin\beta = m\frac{\lambda}{d}$$

where α is the incidence angle, β the exit angle, λ the wavelength and m the order of diffraction. Figure 4.2 shows the propagating orders ($|\sin\beta| < 1$) resulting from incoming light on the grating.

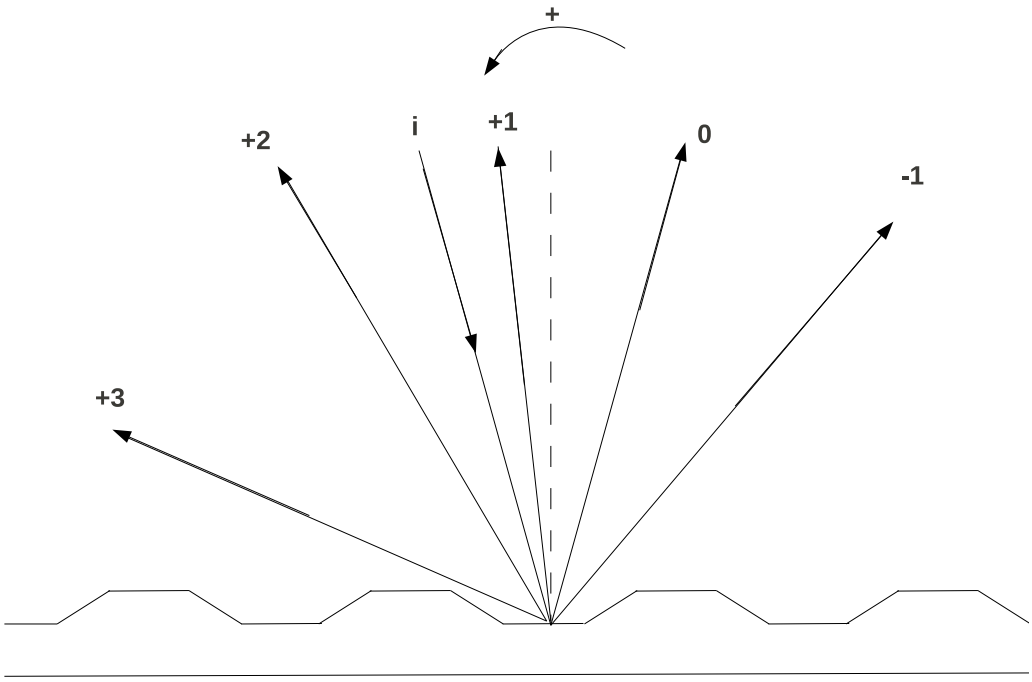

Figure 4.2: Schematic representation of the orders of a diffraction grating.

The orders having $|\sin\beta| > 1$ are called the evanescent orders. They can not be detected at distance greater than a few wavelength from the grating surface, but can play an important role in some surface-enhanced grating properties and must be taken into account in any electromagnetic theory of gratings.

Polarization

It is necessary to distinguish the two cases of polarization. If the incident wave is linearly polarized and the electric field vector is perpendicular to the plane of incidence (or parallel to the grooves), all the diffracted orders have the same polarization. This is called the transverse electric (TE) polarization.

The other case, when the electric field lies in the plane of incidence (so perpendicular to the grooves), also preserves the polarization direction and is called the transverse magnetic (TM) polarization. Any other polarization state can be represented as a linear combination of these two fundamental cases. So, luckily, it is necessary to investigate the grating response only for these polarizations.

4.2.3 Grating anomalies and VUV region

Discovery and first interpretations

Wood (1902) discovered grating anomalies, which are large and sharp irregularities of the function representing the intensity of light diffracted by a grating illuminated with Transverse Magnetic (TM) polarized light. Rayleigh (1907) partially explained these anomalies by connecting them to the threshold (passing off) of higher orders.

Fano (1941) suggested that some of these anomalies could be also associated with the excitation of a surface wave along the grating, which was experimentally confirmed later (Teng & Stern, 1967). Palmer (1952) experimentally showed that anomalous effects could also occur for Transverse Electric (TE) polarization.

Importance of the coating

Gratings are generally coated to prevent oxidation from the air on the surface: Hass & Tousey (1959) discovered that the high reflectance of aluminum can be maintained with transparent overcoatings of MgF_2. Hunter et al. (1971) investigated the dependence of the reflectance on the coating thickness, finding that the reflectance at 121.6 nm under normal incidence was highest for a MgF_2 thickness around 25 nm.

The reflectance of this coating depends also on the MgF_2 deposition rate (Hutcheson et al., 1972), because the conditions of film deposition affect the refractive index of MgF_2 (Wood et al., 1984). Moreover, varying the thickness of a protective dielectric layer can produce efficiency anomalies through the generation of leaky modes (Nevière et al., 1977), and can shift either anomalous wavelengths (Palmer, 1952) or anomalous incidence angles (Loewen et al., 1977). Thus, in addition to the groove profile, the coating must be taken into account to study the grating efficiency and the appearance of anomalies.

VUV region

In the VUV region, the majority of gratings are used at relatively low wavelength to groove spacing ratios ($\lambda/d < 0.2$), where the grating diffraction is virtually free of polarization effects, including anomalies (Loewen et al., 1978). Trapezoidal gratings have an extra degree of freedom compared to conventional gratings (sinusoidal or triangular profile), and theoretical calculations showed they can have a superior efficiency (Mashev et al., 1987).

Nowadays, the anomalous physics is being pulled apart by new techniques, but this does not remove the need for a deeper understanding of the underlying physical mechanisms (McPhedran, 2006). For instance, there is a discussion about the physical nature of the plasmon surface waves and the role played by the groove resonances (Popov et al., 2007).

4.2.4 Experimental procedure

Efficiency testing

The first HJY grating has a groove density of 1200 grooves/mm, a groove depth of 31 nm and a groove profile ratio of 0.53. It was coated with a reflective surface consisting of an 80 nm thick coating of aluminum on top of a 15 nm layer of chromium. To prevent oxidation, a third layer of magnesium fluoride (MgF_2) was added with a thickness of 25 nm. A theoretical analysis was made by HJY, showing that no anomaly should be expected and that an overall efficiency of 27% (not including the coating) would be obtained in the m=+/- 1 orders. No polarization effects were predicted.

Efficiency tests were conducted under high vacuum (below 10^{-6} Torr). A first set of tests was conducted by HJY that found an efficiency of about 25% for each of m = +1 and -1 orders. The design of their test chamber was such that incidence angles smaller than 7° were not possible.

A second set of tests were then conducted at the University of Wisconsin (UW) using a chamber that could support normal incidence illumination. In this chamber, incoming light was collimated through a MgF2 lens, then either diffracted by the grating or reflected by a witness mirror, and then redirected by fold mirrors on a CCD camera (see Fig. 4.3). In these tests we found an efficiency of 11% in both orders at normal incidence, slightly less than half the efficiency measured by HJY.

To verify the discrepancy with the HJY measurements, a third set of tests was conducted at the Center for Astronomy and Space Astronomy (CASA). In these tests, collimated light from a monochromator was first directly imaged onto a detector. The grating was then rotated into the optical path and the diffracted light was collected by the detector. The grating and the detector were mounted respectively on a rotation stage and at the end of a swing arm on circular rail track, allowing the incidence angle and detector position to be externally changed while the experiment was still under vacuum (see Fig. 2). These measurements were more detailed, as the configuration allowed rapid measurement of multiple angles of incidence without cycling the chamber.

The results were consistent with both the HJY and Wisconsin results. At 7° the grating efficiency was near 30%. As the angle from normal incidence was reduced until 0.36°, the efficiency slowly decreased to about 20% until a final measurement at exactly 0° revealed a sharp drop to 11%, confirming the presence of an anomaly (see Fig. 4.4).

Recoating

The measured grating efficiency at normal incidence was a factor of 2 below our required specification. Since the previous modeling had not indicated the presence of an anomaly based on the groove characteristics, we adopted the strategy of addressing the problem through recoating. A new coating deposition was performed at GSFC. They deposited extra-layers of reflecting and protecting materials onto the grating: 60 nm of Al and 25 nm of MgF_2.

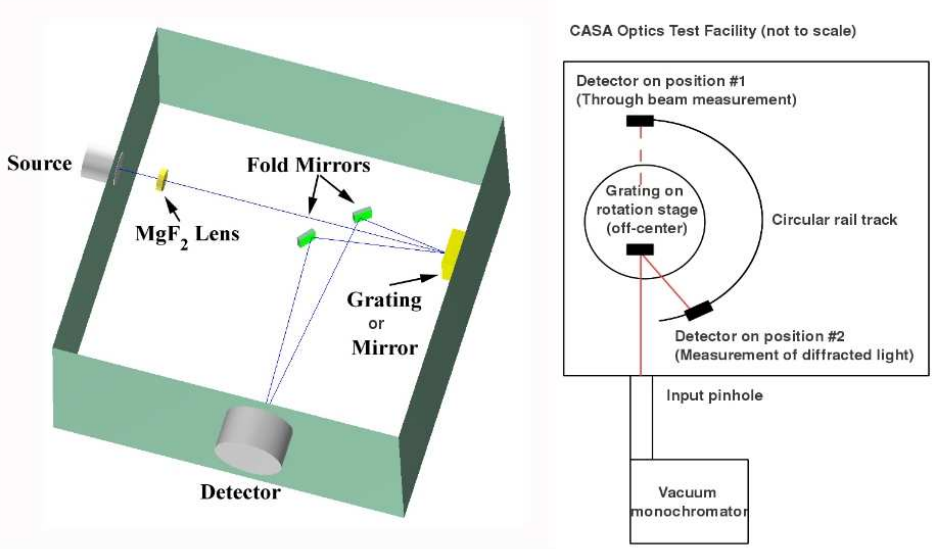

Figure 4.3: (Left) Experimental set-up used at UW. The grating was illuminated on a 2 mm x 5 mm region under normal incidence by a Deuterium Lamp coupled to a vacuum monochromator. Light was collimated through a MgF2 lens; the grating or the witness mirror was mounted on a rotation stage; two fold mirrors redirected light from the +/-1 order onto a CCD camera; an aluminum plate between a fold mirror and the camera was used to block one of both orders. (Right) Experimental set-up used at CASA. The light source is a flowing gas discharge lamp with a selection of gases available. For this test, 65% argon was used with 35% hydrogen. The detector measured light either in a through beam, or after diffraction. The grating was tested under normal incidence and for a series of higher incidence angles up to 10°.

Several tests were performed on the recoated grating. The CASA chamber was again used to map the efficiency of one order for a series of incidence angles from 10° to 0°, for a single order. They found that the new efficiency curve was smooth as a function of the incidence angle: no anomaly was present. However, the application of the second coating had substantially affected the efficiency at higher angles, which had now dropped to between 21% and 23% (see Figure 4.4).

A final set of efficiency measurements were made at normal incidence using the University of Madison chamber, this time for both the m = 1 and -1 orders. They confirmed the CASA findings for both the elimination of the anomaly and the reduced overall efficiency. They also revealed a slight asymmetry in the orders, with

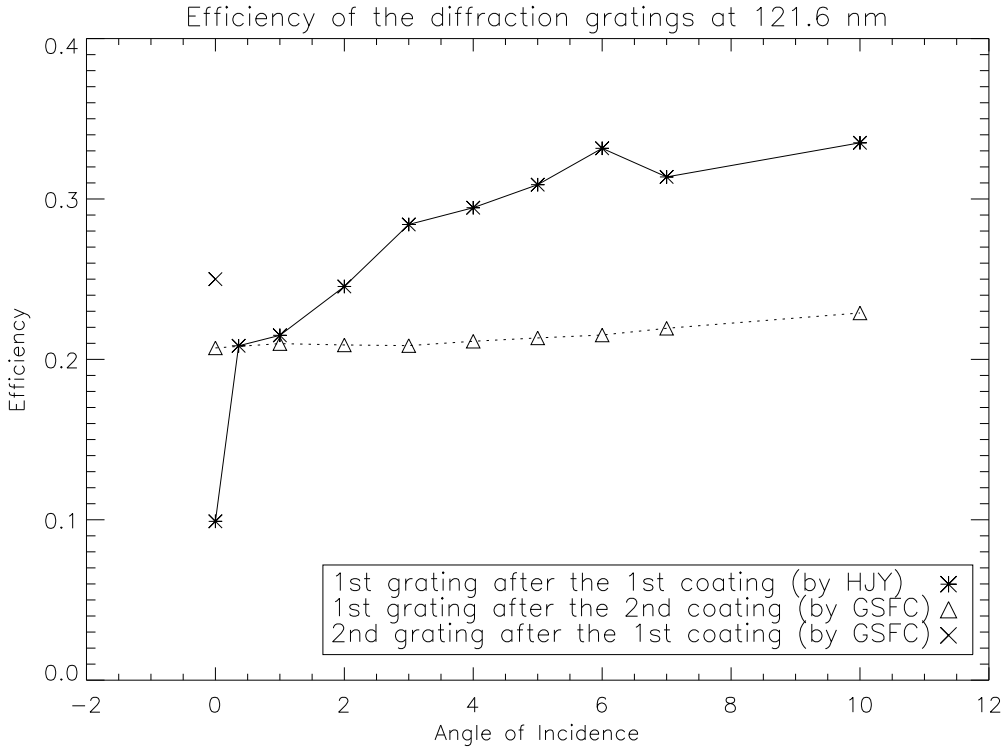

Figure 4.4: Efficiency of both diffraction gratings as a function of incidence angle. The signal-to-noise ratio is about 100.

the m=-1 direction having a 20.5% efficiency and the m=1 order having a 17.5% efficiency. The grating was then returned to HJY for surface characterization using an atomic force microscope (AFM). The AFM showed that the new coating had modified the groove profile with considerably more variation in shape and depth among the individual facets (see Figure 4.5).

A second grating

While the new coating eliminated the anomaly, the variation in groove shape from the accumulation of multiple coatings both reduced the efficiency of the grating for the HYPE-INSPIRE experiment and created uncertainty as to whether the groove shape or coating was responsible for the anomaly. To address both concerns simultaneously, a second grating was obtained from HJY but free of any coating.

This time, the first coating for the grating was provided by GSFC using a 45 nm Al coating overlaid again by 25 nm of MgF_2. This new grating was then tested at the University of Wisconsin, where it was shown to have an efficiency of 25% at normal incidence, very much in line with the original theoretical analysis of HJY.

Table 4.1 shows the parameters of the different coatings.

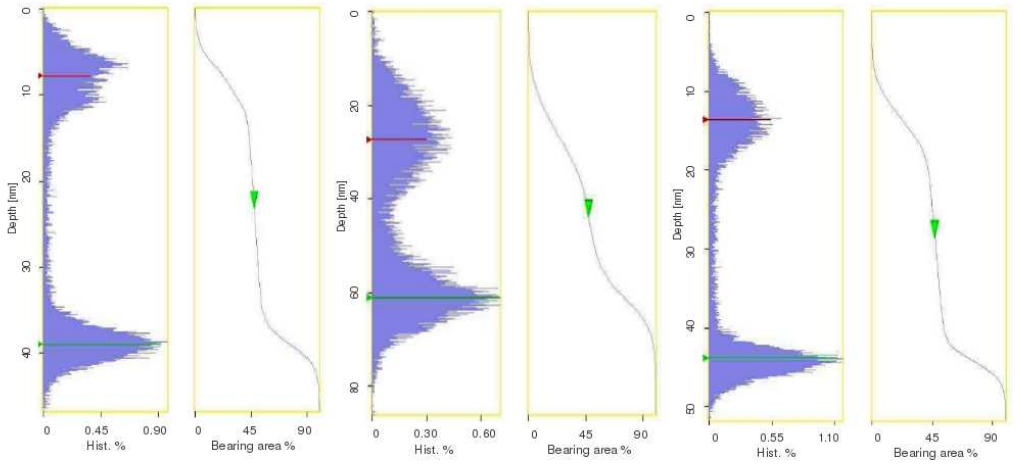

Figure 4.5: AFM measurements of the first grating after the first coating by HJY (left), after the second coating by GSFC (center), and of the second grating without any coating (right). The bearing area percentage curve is the integral of the histogram curve. Note the much sharper distinction between the groove top and valley in the measurements with a single coating.

		Cr (nm)	Al (nm)	MgF_2 (nm)	h (nm)
Grating # 1	coating # 1	15	80	25	31
	coating # 2	-	60	25	33.7
Grating # 2		-	45.1	24.5	30.1

Table 4.1: Layer thickness of different coatings. The parameter h is the groove depth, which has been measured with an Atomic Force Microscope (AFM).

4.2.5 Numerical simulations

Fixed thickness

Figure 4.6 shows calculations made by Popov (2011), using the integral method (Petit, 1975) and verified against the Coordinate transformation method (Chandezon et al., 1980). Unfortunately these calculations do not show any anomaly.

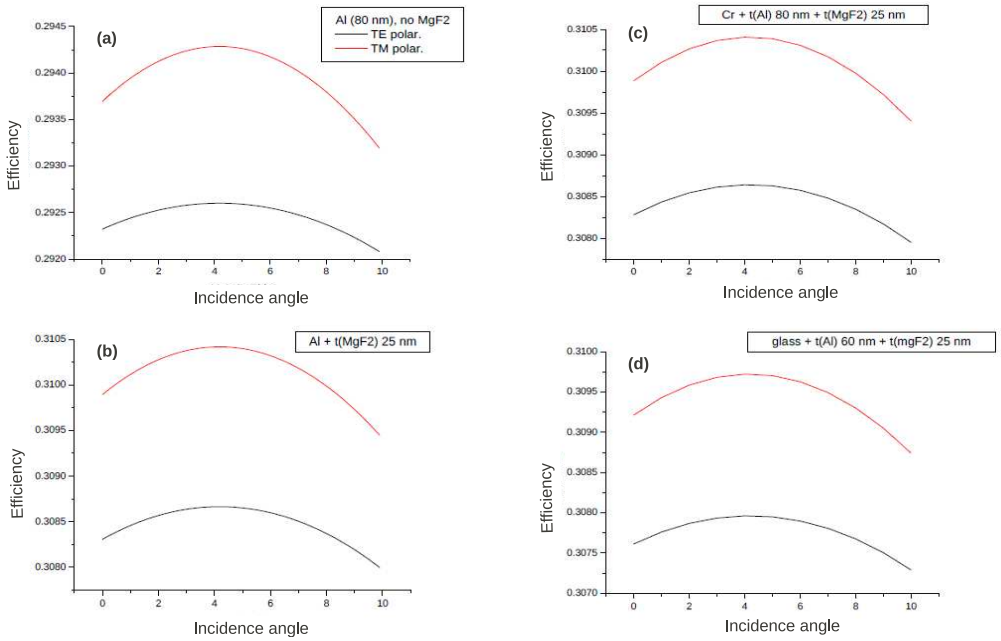

Figure 4.6: Efficiency as a function of the incidence angle (Courtesy of Evgeny Popov). (a) Bare aluminium profile. (b) Aluminium substrate and a 25 nm thick layer of MgF_2. (c) Chrome with a 80 nm thick layer of Al and a 25 nm thick layer of MgF_2. (d) Glass with a a 60 nm thick layer of Al and a 25 nm thick layer of MgF_2.

Variable thickness

Another possibility to explain the anomaly is a calibration error in the coating thickness, resulting into a coating thicker or thinner than expected. Figure 4.7 shows other calculations made by Popov (2011) who tested different thickness of Al and MgF_2. But these calculations can not explain the anomaly either.

4.2.6 Discussion and conclusion

These gratings have a relatively low wavelength to groove spacing ratio (λ/d = 0.15) and, as discussed above, should be virtually free of anomalies based on the general case. However the normal incidence configuration used here is unusual and, combined with trapezoidal grooves of the grating, may have produced an unanticipated effect.

As shown in Figure 4.5, recoating of the first grating significantly smoothed out the groove features. Since this reduced the effect of narrow projected facets on the sides of the trapezoidal profile, it may have contributed to the disappearance of the anomaly. The test for this effect comes from the second grating. The groove profile of the second replica is nearly identical to the first one, as illustrated by the AFM measurements (Figure 4.5, left and right). It was coated with an identical MgF_2 layer thickness on a slightly thinner Al reflective substrate, which implies that

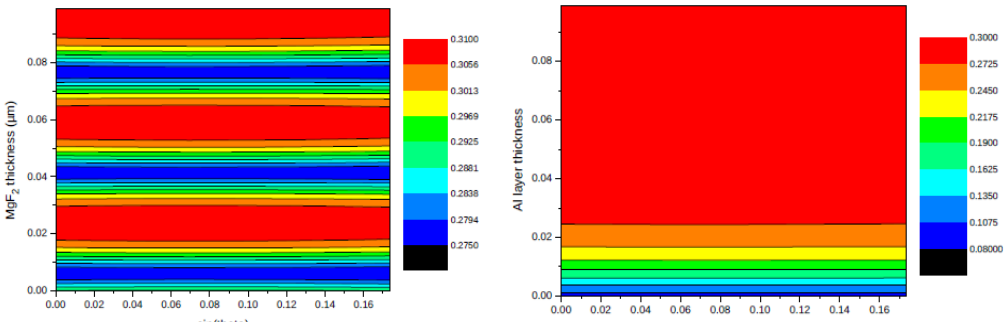

Figure 4.7: Efficiency as a function of incidence angle and layer thickness (Courtesy of Evgeny Popov). *Left:* 80 nm thick layer of Al and a varying thickness of MgF_2. *Right:* Varying thickness of Al and 25 nm thickness of MgF_2.

the projected facet dimensions of the grooves would likewise be similar to the first grating. The lack of an anomaly under these circumstances therefore suggests that the grooves are not primarily responsible and that the source of the anomaly can be tied to the original treatment on the first grating.

Both HJY and GSFC used the same thickness of MgF_2 (25 nm), however differences in the deposition conditions may have affected the refractive index of the dielectric and hence the efficiency. The only difference between the coatings comes from the reflecting layer of Al, which is thinner for GSFC (60 and 45 nm instead of 80) and undercoated with Cr (15 nm) for HJY. The relationship of these differences to the observed characteristics of the anomaly is not clear.

Attempts to use theoretical tools in order to identify a cause were unsuccessful.

4.3 Next steps for HYPE-INSPIRE

4.3.1 Integration

Alignment and shaking tests

The first step of the integration consists of assembling the mechanical structure and aligning the optical components. NASA facilities have shaking tables which allow testing the robustness of the payload against vibrations.

The first shaking test aims to verify that the mechanical structure is solid enough to survive the conditions of a sounding-rocket flight. In that first test, all optical components (telescope, polarimeter, SHS, detector and calibration lamp) are replaced by mass models.

Then one needs to test if the optical alignment will hold during flight. This test is made by another shaking test, previous to which the optical components are aligned to create interference fringes. The success of this test is determined by the apparition or not of interference fringes after the shaking session. To make the

alignment tests easier, the SHS is mounted on a daughter plate that can be attached and detached to a parent plate which belongs to the whole mechanical structure.

The alignment is first tested in visible at the Balmer-β wavelength (486.1 nm). This is made by replacing the 1200 l/mm grating by a 300 l/mm grating, so the product $G\,\lambda$ remains almost constant and the grating equation yields a similar diffraction angle for the first bounce of the incident light on the grating. This trick allows to test the alignment of the optics in the visible without changing the angle between the roof mirror and the flat mirror. Figure 4.8 shows a schematic set-up for aligning the SHS.

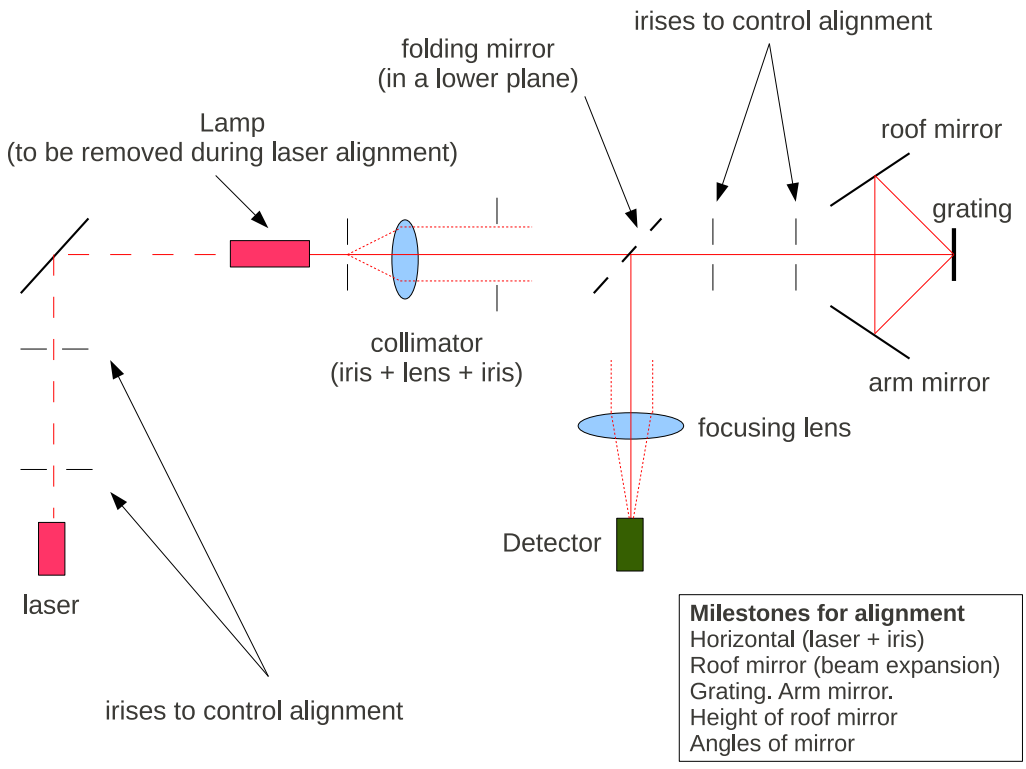

Figure 4.8: Schematic set-up for alignment of the SHS in the visible.

Vacuum tests

The next step consists of actually testing the SHS at Ly-α, which requires operation in a vacuum chamber because of the absorption by the air. Once the alignment is achieved, the payload will have another shaking test that will indicate if it is ready for a flight.

4.3.2 Flight window

The March April time frame is best for the study of the upwind and downwind IPH, because the Doppler shift is maximized and the degree of polarization is largest (Ajello & Thomas, 1985). The downwind IPH direction, which is half as bright and more modified by solar factors, is also observable in a December window with a Doppler effect large enough for minimal separation from the geocorona. One advantage to this look direction is that it will be occupied by Jupiter in 2013, which will allow HYPE to block a portion of the downstream scattering. The primary disadvantage is that there should be only a minimal polarimetric signature during this time, due to the emphasis on pure backscatter.

Current planning for a flight is complicated by a lack of access to a functioning thrust termination system (cutdown) and a primary booster. This limitation began in December 2010 and is expected to continue through all of 2011. A replacement thrust termination system is expected in early 2011, along with a limited delivery of boosters. This may not be enough to support a March 2012 launch, but should allow a January 2013 launch to observe the downwind IPH.

Conclusions

The heliospheric interface: a challenge for modellers and observers

The interaction between the solar wind and the local interstellar medium (LISM) is a complex and challenging problem, which requires a time-dependent and three-dimensional treatment, combining plasma physics and radiative transfer. The solar wind and the plasma component of the LISM can be described with a magneto-hydrodynamic approach, but the modelling of the hydrogen atoms needs the framework of kinetic theory because their mean free path is comparable with the size of the problem. While the ionized components are deflected, the hydrogen neutrals can cross the heliopause and carry the signature of the interface because of charge-exchange reactions.

In the inner heliosphere, the interplanetary hydrogen (IPH) is strongly affected by the Sun and backscatters the solar Ly-α photons that bring precious information to the observer. Although the optically thin approximation can be used for the interpretation, a thorough data analysis would require to take into account the multiple scattering. Observations over the last two decades showed that the IPH velocity has variations which are correlated to the solar activity.

Our study of HST/STIS observations revealed some contamination that has not been taken into account previously. This updated analysis corrected the discrepancy with SOHO/SWAN data at solar maximum, however current models can not explain the higher velocities at solar minimum. We suggested that could be due to an indirect effect of the local interstellar magnetic field, which should be included in future modelling efforts. There may be extra features as the geocoronal deuterium or a possible Fermi effect from the heliospheric interface but the diagnostic is difficult because the resolution of these observations is limited (R$\approx$ 20,000).

Regular Ly-α measurements will be extremely helpful to constrain a problem which requires a multi-observational approach. In this context, the SHS technique represents a wonderful opportunity to obtain new Ly-α measurements with a higher resolution (R$\approx$ 100,000) and obtain observations of the fine structure, including the primary and secondary populations of interstellar hydrogen.

Spatial Heterodyne Spectrometer: a promising technique for space applications

The Spatial Heterodyne Spectrometer is an emerging class of interferometers, which combines both high étendue and high resolving power. The main limitations of this

instrument are a reduced bandpass and multiplexing noise, so it is well suited for observation of emission lines. An all-reflective configuration enables operation under the constraints of the ultraviolet range. Moreover its monolithic design makes it a solid candidate for space applications.

The HYPE-INSPIRE project implements an improved design that provides imaging and anti-aliasing. Moreover it will provide measurements of linear polarization, particularly interesting for observations of Jupiter, with a possible detection of the Hanle effect due to the jovian magnetic field at the surface level. It is currently scheduled for a flight in 2012.

Contrarily to the hydrogen cells used on SOHO/SWAN, the SHS technique does not need an one-year orbit to obtain a complete line profile of the IPH Ly-α emission. This is why the SHS technique could be implemented to measure instantaneously the line profile from a satellite platform. Such an experiment will improve the achievements of SOHO/SWAN by providing a map of the IPH Ly-α pattern with a higher temporal precision, which may bring a new insight on the physics of the heliosphere.

Appendix A

Plasma physics

A.1 Electromagnetism: Maxwell's equations

$$\nabla \cdot \mathbf{E} = \frac{\rho}{\varepsilon_0}$$

$$\nabla \cdot \mathbf{B} = 0$$

$$\nabla \times \mathbf{E} = -\frac{\partial \mathbf{B}}{\partial t}$$

$$\nabla \times \mathbf{B} = \mu_0 \, \mathbf{j} + \mu_0 \, \varepsilon_0 \, \frac{\partial \mathbf{E}}{\partial t}$$

A.2 Kinetic theory of gases: the Boltzmann Equation

The following results have been exposed in several textbooks or review papers that discuss the subject in greater extents and with more mathematical details (e.g., Chapman & Cowling, 1953; Spitzer, 1956).

A.2.1 Statistical description of particles

The kinetic theory of gases involves the density of particles in phase space, f, as a function of position $\mathbf{r}$ and velocity $\mathbf{w}$. One defines $f(\mathbf{r}, \mathbf{w}, t)\, dx\, dy\, dz\, dw_x\, dw_y\, dw_z$ as the number of particles which lie within the spatial volume $dx\, dy\, dz$, centered at $\mathbf{r}$, and whose velocities lie within the intervals dw_x, dw_y and dw_z, centered at $\mathbf{w}$.

For simplicity, we will use the notations $d\mathbf{r} = dx\, dy\, dz$ and $d\mathbf{w} = dw_x\, dw_y\, dw_z$ that represent the volume elements in the physical space and velocity space, respectively.

The quantity $f(\mathbf{r}, \mathbf{w}, t)\, d\mathbf{r}\, d\mathbf{w}$ represents the number of particles averaged in the time interval between t and $t + dt$. Thus the so-called *distribution function* $f(\mathbf{r}, \mathbf{w}, t)$ represents the probable number of particles in the 6D phase space.

A.2.2 Macroscopic quantities

One can define macroscopic quantities that describe the state of the gas. For instance, the integral of the distribution function over the velocity space gives the *number density of particles*:

$$n = n(\mathbf{r}, t) = \int f(\mathbf{r}, \mathbf{w}, t)\, d\mathbf{w}$$

One can generalize. Let us define $Q(\mathbf{w})$ a function of the velocity $\mathbf{w}$, whose value can a scalar, a vector or a tensor. We can define its mean value by:

$$\langle Q \rangle = \frac{1}{n} \int Q(\mathbf{w})\, f(\mathbf{r}, \mathbf{w}, t)\, d\mathbf{w}$$

The quantity $\langle Q \rangle$ may still depend on the distance $\mathbf{r}$ and the time t. With $Q(\mathbf{w}) = 1$, we obtained the number density of particles (moment of order zero). With $Q(\mathbf{w}) = \mathbf{w}$, we obtain the *bulk velocity* (moment of order 1):

$$\mathbf{v} = \langle \mathbf{w} \rangle = \frac{1}{n} \int \mathbf{w}\, f(\mathbf{r}, \mathbf{w}, t)\, d\mathbf{w}$$

With the bulk velocity, one can introduce $\mathbf{u}$ the *random velocity* such that $\mathbf{w} = \mathbf{v} + \mathbf{u}$. One should remark that this component does not depend on the referential velocity and that $\langle \mathbf{u} \rangle = 0$. The notation $\mathbf{a} \otimes \mathbf{b}$ represents the dyadic product (or tensor product) of vectors $\mathbf{a}$ and $\mathbf{b}$, and it forms a second-order tensor that can be represented by a 2-dimensional (2D) matrix. With $Q(\mathbf{w}) = m\, \mathbf{w} \otimes \mathbf{w}$, we can compute the moment of order 2 and define the pressure. It is easy to show that $\langle \mathbf{v} \otimes \mathbf{u} \rangle = \mathbf{v} \otimes \langle \mathbf{u} \rangle = 0$ and that the quantity $\langle \mathbf{u} \otimes \mathbf{v} \rangle$ is also null. So we can write:

$$n\, m \langle \mathbf{w} \otimes \mathbf{w} \rangle = n\, m \langle \mathbf{v} \otimes \mathbf{v} \rangle + n\, m \langle \mathbf{u} \otimes \mathbf{u} \rangle$$

The term $n\, m \langle \mathbf{v} \otimes \mathbf{v} \rangle$ is the dynamic tensor. The other term will be noted $\Psi = n\, m \langle \mathbf{u} \otimes \mathbf{u} \rangle$. This is the *stress tensor* (or tensor of kinetic pressure). As $\mathbf{u}$, the stress tensor does not depend on the referential velocity.

A.2.3 The Boltzmann Equation

The total derivative Df/Dt defines the rate of change of f along the trajectory of a particle. The Boltzmann equation states that Df/Dt is entirely the result of encounters among the particles:

$$\frac{Df}{Dt} = \left(\frac{\partial f}{\partial t} \right)_{coll} = C(f)$$

where $C(f)$ represents the net gain of particles for the phase-space volume $d\mathbf{r}\, d\mathbf{w}$ that follows the particle during the interval dt. Some authors call it the integral of collisions (e.g., Baranov, 2000). In this absence of collisions ($C(f) = 0$), this

equation reduces to Liouville's theorem, which states that for a conservative system, f is constant along a dynamical trajectory. One can express the total derivative as a function of the partial derivatives:

$$\frac{Df}{Df} = \frac{\partial f}{\partial t} + \mathbf{w} \cdot \frac{\partial f}{\partial \mathbf{r}} + \frac{\partial \mathbf{w}}{\partial t} \cdot \frac{\partial f}{\partial \mathbf{w}}$$

where the operators $\partial/\partial\mathbf{r}$ and $\partial/\partial\mathbf{r}$ represent the directional derivatives. According to the second law of motion, the term $\partial\mathbf{w}/\partial t$ is equal to $\mathbf{F}/m$, where $\mathbf{F}$ is the sum of the forces applied to the particle of mass m. Then one obtains one standard version of the *Boltzmann equation*:

$$\frac{\partial f}{\partial t} + \mathbf{w} \cdot \frac{\partial f}{\partial \mathbf{r}} + \frac{\mathbf{F}}{m} \cdot \frac{\partial f}{\partial \mathbf{w}} = C(f) \tag{A.1}$$

In the general case, this equation belongs to the BBGKY hierarchy of equations [1], that consider N equations with N distribution functions.

A.3 The fluid equations

A.3.1 Preliminary

From the Boltzmann equation, one can derive the fluid equations that describe the macroscopic quantities of the distribution function, namely its different orders. First, we are going to multiply the equation (A.1) by $Q = Q(\mathbf{w})$ and integrate over the velocity space. Then, we can re-arrange each term of the left-hand side. We can reasonably assume that the functions are smooth enough so we can swap the temporal derivative and the integral. The third term $(Q\,\mathbf{F}/m \cdot \partial f/\partial \mathbf{w})$ needs an integration by parts. So we obtain:

$$\int Q \frac{\partial f}{\partial t}\, d\mathbf{w} = \frac{\partial}{\partial t}(n\langle Q \rangle) \tag{A.2}$$

$$\int Q\,\mathbf{w} \cdot \frac{\partial f}{\partial \mathbf{r}}\, d\mathbf{w} = \frac{\partial}{\partial \mathbf{r}} \cdot (n\ \langle Q\,\mathbf{w} \rangle) \tag{A.3}$$

$$\int Q\,\mathbf{F} \cdot \frac{\partial f}{\partial \mathbf{w}}\, d\mathbf{w} = -n \left\langle \frac{\partial}{\partial \mathbf{w}} \cdot (\mathbf{F}\,Q) \right\rangle \tag{A.4}$$

At the exception of the magnetic forces, all other forces do not depend on the velocity, so it is obvious that:

$$\frac{\partial}{\partial \mathbf{w}} \cdot (\mathbf{F}\,Q) = \mathbf{F} \cdot \frac{\partial Q}{\mathbf{w}} \tag{A.5}$$

The relation holds for the magnetic forces. For simplicity, we will drop the charge q and write $\mathbf{F} = \mathbf{w} \times \mathbf{B}$. To make a general demonstration, we will consider the

[1] BBGKY stands for the different authors who established this system of equation: Bogoliubov (1946), Born and Green (1949), Kirkwood (1946,1947), Yvon (1935).

function $\mathbf{Q}$ to be a tensor. Using the formula for the divergence of a tensor product, we obtain:

$$\nabla \cdot (\mathbf{F} \otimes \mathbf{Q}) = (\nabla \cdot \mathbf{F})\mathbf{Q} + (\mathbf{F} \cdot \nabla)\mathbf{Q}$$

Where the nabla symbol is the vector differential operator by respect to the velocity (not the distance). Then we develop the first term of the right-hand side:

$$\nabla \cdot \mathbf{F} = \frac{\partial}{\partial \mathbf{w}} \cdot (\mathbf{w} \times \mathbf{B}) = \mathbf{B} \cdot \left(\frac{\partial}{\partial \mathbf{w}} \times \mathbf{w} \right) - \mathbf{w} \cdot \left(\frac{\partial}{\partial \mathbf{w}} \times \mathbf{B} \right)$$

The second term is obviously null because the magnetic field does not depend on the velocity. The first term is null too, because one component of the velocity is independent of the the other ones. So the combination of the Boltzmann equation and the relations (A.2-A.5) gives an integro-differential equation for the distribution function:

$$\frac{\partial}{\partial t}(n\langle Q \rangle) + \frac{\partial}{\partial \mathbf{r}} \cdot (n \langle Q\, \mathbf{w} \rangle) - \frac{n}{m} \left\langle \mathbf{F} \cdot \frac{\partial Q}{\partial \mathbf{w}} \right\rangle = \int Q\, C(f)\, d\mathbf{w} \tag{A.6}$$

A.3.2 The particular case of elastic collisions: the ideal gas

If we restrict our study to elastic collisions, one can consider that the total number density, the momentum and the energy of the gas particles will be conserved. So the right-hand side of the equation (A.6) will vanish for the three following cases: $Q = 1$, $Q = m\,\mathbf{w}$ and $Q = m\,w^2$. The assumption of elastic collisions will be justified later.

Then for $Q = 1$, one obtains the *continuity equation*:

$$\frac{\partial n}{\partial t} + \nabla \cdot (n\mathbf{v}) = 0$$

where the nabla operator is the directional derivative in the direction $\mathbf{r}$ ($\nabla = \partial/\partial\mathbf{r}$).

With $Q = m\,\mathbf{w}$, the right-hand side of the equation (A.6) is null again, so one obtains:

$$\frac{\partial}{\partial t}(n\,m\,\mathbf{v}) + \frac{\partial}{\partial \mathbf{r}} \cdot (n\,m\,\langle \mathbf{w} \otimes \mathbf{w} \rangle) - n\,\mathbf{F} = 0 \tag{A.7}$$

The first term can be developed as the derivative of a product. The second term $(n\,m\,\langle \mathbf{w} \otimes \mathbf{w} \rangle)$ can be decomposed as the sum of the dynamic tensor $(n\,m\,\mathbf{v} \otimes \mathbf{v})$ and the stress tensor (Ψ), as seen previously. Then one can apply the formula $\nabla \cdot (A \otimes B) = (\nabla \cdot A)B + (A \cdot \nabla)B$ to the expression $(n\,m\,\mathbf{v}) \otimes \mathbf{v}$. For this study, the gases are non-relativistic and nuclear reactions will not be a concern, so the forces will be the Lorentz force $(q(\mathbf{E} + \mathbf{v} \times \mathbf{B}))$ and the gravitation $(m\,\mathbf{g})$. Finally, by combining with the continuity equation, the equation (A.7) can be re-arranged into:

$$n\,m \left(\frac{\partial \mathbf{v}}{\partial t} + \mathbf{v} \cdot \nabla \mathbf{v} \right) = n\,q(\mathbf{E} + \mathbf{v} \times \mathbf{B}) - n\,m\,\mathbf{g} - \nabla \cdot \Psi$$

A.3.3 General case

The kinetic theory contains interesting and powerful tools. Unfortunately this goes beyond the scope of this work and will not be detailed. However one can keep in mind some important points. One quantifies the collisions within a plasma with the Knudsen number. This is a dimensionless number, defined by the ratio of the free mean path of a particle (λ) over a length typical of the studied case (L), so:

$$Kn = \frac{\lambda}{L}$$

For a collisional plasma, we have $K \ll 1$. Then the H-theorem shows that, because of collisions, the velocity distribution converges toward a Maxwell-Boltzmann distribution defined by:

$$f(\mathbf{w}) = \frac{n}{\sqrt{2\,\pi}\,V_{th}} \exp\left(-\frac{(\mathbf{w}-\mathbf{v})^2}{v_{th}}\right)$$

Where n, $\mathbf{v}$ and w are the density, the bulk velocity and the thermal velocity. The local thermodynamic equilibrium is characterized by solutions in the vicinity of the Maxwellian distribution. With the Chapman-Enskog method, one can develop in the first order and obtain the classical transport equations, including the Navier-Stokes equations (which are a generalization of the Euler equations) with the viscosity coefficients. The proof of the H-theorem and the details of the Chapman-Enskog method are available in different textbooks (e.g. Chapman & Cowling, 1953).

When the Knudsen number is comparable or greater than the typical length of the problem ($Kn \geq 1$), the Chapman-Enskog method does not apply and the Navier-Stokes are not valid anymore. The fluid approach must be replaced by a kinetic approach and one has to go back to the Boltzmann equation. This case will rise in this study.

A.4 (Magneto)hydrodynamics

A.4.1 The speed of sound

Perturbations of density can propagate within a compressible fluid and form a compression wave. For an isentropic process, one defines the speed of sound as the derivative of the pressure by respect to the density, so:

$$a = \sqrt{\left(\frac{\partial p}{\partial \rho}\right)_S}$$

The speed of sound is the result of the compressibility of the fluid. It is infinite for a fluid assumed to be incompressible. Moreover one can show that:

$$a = \sqrt{\gamma \left(\frac{\partial p}{\partial \rho}\right)_T}$$

Where γ is the ratio of specific heats, or heat capacity ratio, which is equal to 5/3 for a perfect gas.

A.4.2 Shock physics: the Rankine-Hugoniot relations

The Rankine-Hugoniot relations describe the general behaviour of an one-dimensional shock wave for a compressible flow (Ames Staff Research, 1953). To obtain them, one needs first to integrate the Euler equations over a control volume that includes the shock. In the stationary case, the integrals are relatively simple:

$$\rho_1 \, v_1 = \rho_2 \, v_2$$

$$\rho_1 \, v_1^2 + p_1 = \rho_2 \, v_2^2 + p_2$$

$$\rho_1 \, v_1 \, (e_1 + \frac{1}{2} v_1^2 + \frac{p_1}{\rho_1}) = \rho_2 \, v_2 \, (e_2 + \frac{1}{2} v_2^2 + \frac{p_2}{\rho_2})$$

Where the quantity e is the internal energy and p is the thermal pressure (not the total pressure). The subscripts 1 and 2 denote the value just inside (ahead) and outside (beyond) the shock transition.

On one hand, the third equation can be easily simplified with the first one and then combined with the state equation of a polytropic fluid: $p = (\gamma - 1) \, \rho \, e$, where γ is the ratio of specific heats (not necessarily adiabatic). On the other hand, one can express the velocities as functions of pressures and mass densities, from the first two equations. After some calculations, one finally obtains the Rankine-Hugoniot relations:

$$\frac{\rho_2}{\rho_1} = \frac{\frac{p_2}{p_1}(\gamma + 1) + (\gamma - 1)}{(\gamma + 1) + \frac{p_2}{p_1}(\gamma - 1)} = \frac{v_1}{v_2}$$

A.4.3 Frozen magnetic field lines

If we note the electrical conductivity σ, the Ohm's law can be written:

$$\mathbf{E} = \frac{\mathbf{j}}{\sigma} - \mathbf{v} \times \mathbf{B}$$

On the other hand, the Maxwell-Faraday equation for the induction gives:

$$\nabla \times \mathbf{E} = -\frac{\partial \mathbf{B}}{\partial t}$$

If we suppose the conductivity uniform and infinite ($\sigma = \infty$), the induction equation becomes:

$$\frac{\partial \mathbf{B}}{\partial t} = \nabla \times (\mathbf{v} \times \mathbf{B})$$

By considering the magnetic flux passing through a surface bounded by a contour moving with the fluid, one can show that this magnetic flux remains unchanged (e.g. Sturrock, 1994, pp. 186-188). This is why one says that the field lines are "frozen" in the material.

A.5 The kappa distribution

The kappa distribution is a generalized Lorenzian, defined by:

$$f(v) = \frac{n_0}{2\,\pi}\,\frac{A_\kappa}{(\kappa\,w^2)^{3/2}}\left[1+\frac{v^2}{\kappa\,w^2}\right]^{-(\kappa+1)} \text{ with } A_\kappa = \frac{\Gamma(\kappa+1)}{\Gamma(\kappa-1)\,\Gamma(3/2)}$$

where w is the thermal speed, and the Gamma function arises as a result of the normalization. The distribution approaches the Maxwellian, as $\kappa \to \infty$.

Appendix B

Ultraviolet spectrometry with HST

B.1 Description of the instruments

B.1.1 GHRS

The GHRS instrument was launched with HST in 1990. It spatial resolution (0.25″) was initially degraded by the spherical aberration in HST's primary mirror but has been recovered after the installation of the Corrective Optics Space Telescope Axial Replacement (COSTAR) on the first servicing mission in 1993. The GHRS design is described by Brandt et al. (1994).

The instrument has two square entrance slits, located in the focal plane of the telescope 5.34″ from the optical axis. A collimator mirror directs the light to a carousel (Fig. B.1), which holds one ruled and four holographic plane diffraction gratings used in first order, one echelle, and mirrors for four target acquisition modes. The desired optical element is engaged by rotating the carousel to place it in the collimated beam. Specific wavelengths can be selected by commanding the carousel to a particular position within the range available to each grating. The dispersed light is relayed to one of two camera mirrors for the first-order modes, or one of two concave cross-disperser gratings for the echelle. These elements focus the spectrum onto the photocathode of one of two Digicon detectors.

B.1.2 STIS

The Space Telescope Imaging Spectrograph (STIS) was installed on the *Hubble Space Telescope* to replace GHRS during the second servicing mission in 1997 and operated until 2004. It was restored to operations in May 2010, after being repaired during the servicing mission 4. Its design is described by Woodgate et al. (1998).

The STIS optics have been configured into two basic subassemblies. The first is a two-element reflecting corrector, which eliminates the spherical aberration created by the primary mirror manufacturing error and the off-axis aberrations present in

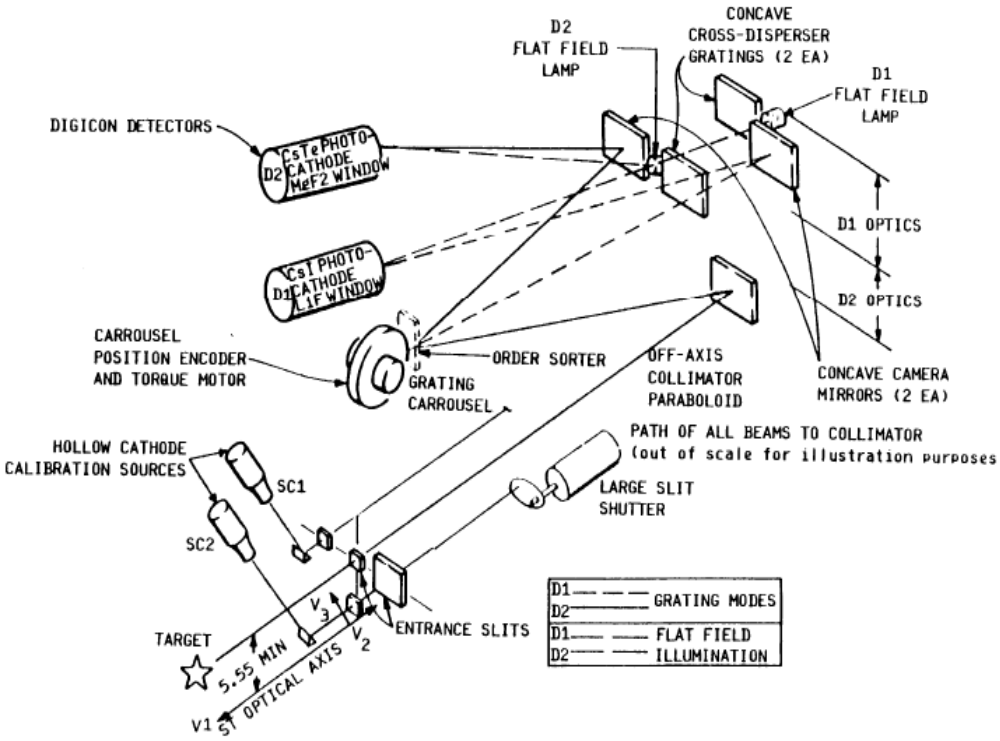

Figure B.1: GHRS design

all Ritchey-Chrétien telescopes [1]. The corrector is followed by the imaging spectrograph: collimator, grating, and camera elements to provide high-resolution and high-efficiency spectroscopy and imaging capability in order to satisfy the science requirements.

Light from the corrected HST image enters the spectrometer through one of the slits on the slit wheel (Fig. B.2). The slits, which are used to set the required field of view for the various modes of operation, range in size from 50″ x 50″ to 0.1″ x 0.025″. After passing through the slit wheel, the light is collimated by an off-axis elliptical mirror. The parallel beam is directed to the grating wheel, which directs the light toward one of the three detectors of interest.

[1] A Cassegrain telescope consists of a primary concave mirror and a secondary convex mirror. The Ritchey-Chrétien telescope is a specialized Cassegrain telescope that has been designed to eliminate the comatic aberration, thus providing a larger field of view compared to a more conventional configuration.

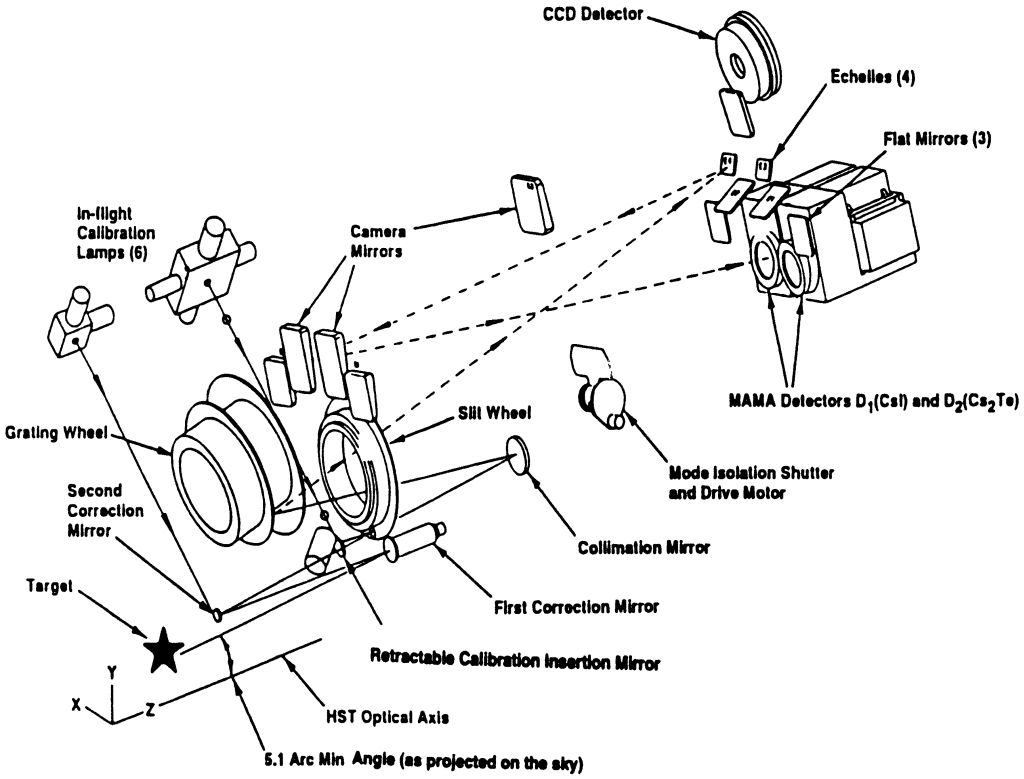

Figure B.2: STIS design

B.2 Sensitivity at Ly-α

B.2.1 Simulation of the throughput

High-resolution observations of the Ly-α line require the use of the Echelle A grating with one Digicon detector for GHRS, and the E140H grating with the FUV-MAMA detector for STIS. The sensitivities of both instruments were compared in two similar ways. First, Bostroem (2011) calculated the throughput of each mode, as shown in Fig. B.3.

B.2.2 Calculation of the sensitivities

Secondly, it is also possible to compare the sensitivity functions given by the instrument handbooks (IHB). GHRS's peak sensitivity for Echelle A is 1.2e11 (counts/s/diode) per incident (ergs/cm^2/s/Å), with a diode being 0.0127 Å, so 9.45e12 (counts/s/Å) per incident (ergs/cm^2/s/Å).

STIS's peak sensitivity is 1.1e11 (cts/s/pixel) per incident (ergs/cm^2/s/Å) with a pixel being 0.00535Å. Then STIS's sensitivity per angstrom is 2.05e13 (counts/s/Å) per incident (ergs/cm^2/s/Å).

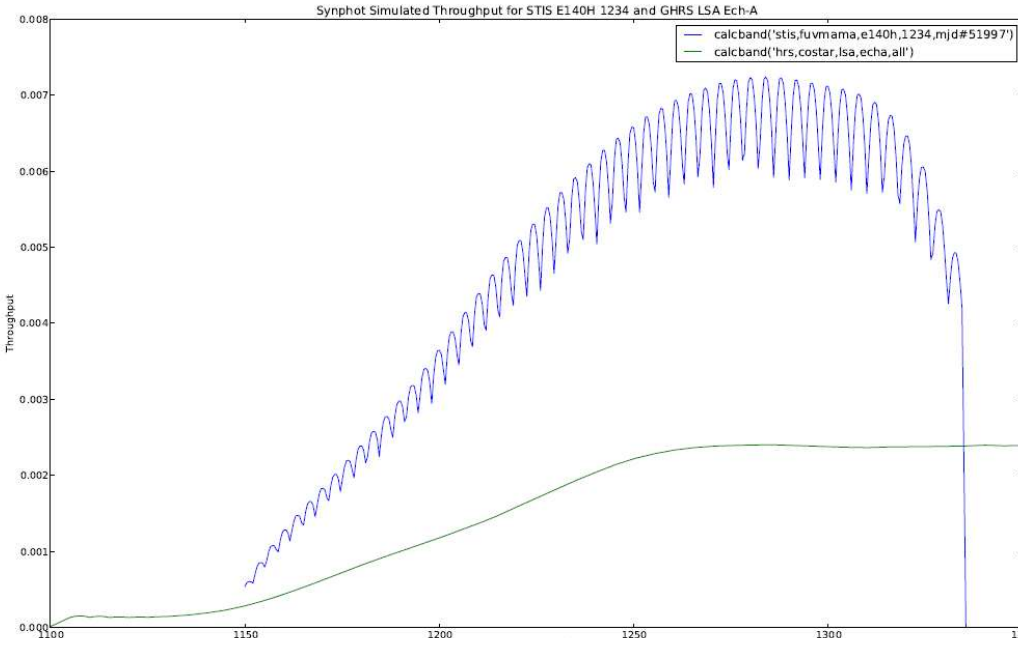

Figure B.3: Throughputs of GHRS and STIS at Ly-α, calculated with Pysynphot. Courtesy of Azalee Bostroem (Space Telescope Science Institute).

Therefore STIS is about 2 times as sensitive as GHRS at Ly-α. This agrees with the calculation of the throughputs (Fig. B.3).

B.3 Exposure times of the IPH observations

Table B.1 shows the details of the different exposures made by GHRS and STIS when they observed the backscattering of solar Ly-*alpha* photons by the interplanetary hydrogen (IPH).

Dataset	Start Time	Stop Time	Exposure Time	Instrument
Z2BY0102T	1994-04-07 08:22:35	1994-04-07 08:33:09	544.000	GHRS
Z2BY0103N	1994-04-07 08:35:46	1994-04-07 09:57:19	544.000	GHRS
Z2BY0104T	1994-04-07 09:58:49	1994-04-07 10:07:01	408.000	GHRS
Z2BY5102T	1995-03-25 17:35:11	1995-03-25 17:45:45	544.000	GHRS
Z2BY5103T	1995-03-25 17:48:06	1995-03-25 17:58:40	544.000	GHRS
Z2BY5104T	1995-03-25 17:59:55	1995-03-25 19:15:24	544.000	GHRS
Z2BY5105T	1995-03-25 19:16:37	1995-03-25 19:27:11	544.000	GHRS
Z2BY5106T	1995-03-25 19:28:26	1995-03-25 19:39:00	544.000	GHRS
Z2BY5107T	1995-03-25 19:40:15	1995-03-25 20:56:29	544.000	GHRS
Z2BY5108T	1995-03-25 20:57:42	1995-03-25 21:08:16	544.000	GHRS
O65F03010	2001-03-29 03:48:45	2001-03-29 04:29:35	2450.117	STIS

Table B.1: Datasets and times of observations by GHRS & STIS

Appendix C

Fundamental constants

- proton mass: $m_p = 1.672621637(83) \times 10^{-27}$ kg
- electron mass : $m_e = 9.10938291(40) \times 10^{31}$ kg
- electric charge : $q = 1.602176565(35) \times 10^{19}$ C
- Boltzmann constant: $k_B = 1.3806488(13) \times 10^{-23}$ J·K^{-1}
- gravitational constant: $G = 6.67384(80) \times 10^{-11}$ N·m^{-2}·kg^{-2}
- Planck constant: $h = 6.62606957(29) \times 10^{-34}$ J·s
- speed of light : $c = 299,792,458$ m·s^{-1}
- vacuum permittivity : $\varepsilon_0 = 8.854187817620 \times 10^{-12}$ F·m^{-1}
- vacuum permeability : $\mu_0 = 4\pi \times 10^{-7}$ H·m^{-1}
- Sun's mass : $M_\odot = 1.9891 \times 10^{30}$ kg

Appendix D

Acronyms

- ISM : Interstellar Medium
- LISM : Local Interstellar Medium
- IPH : Interplanetary Hydrogen
- LIC : Local Interstellar Cloud
- SW : Solar Wind
- TS : Termination Shock
- HP : Heliopause
- BS : Bow Shock
- SHS : Spatial Heterodyne Spectrometer/Spectroscopy

Bibliography

Adams, W.: *The Gaseous Clouds of Interstellar Space*, PASP, 60, 174-189 (1948)

Adams, T.F., Frisch, P.: *High-resolution observations of Lyman Alpha sky background*, Astrophys. J., 212, 300-308 (1977)

Ajello, J.M.: *An Interpretation of Mariner 10 Helium (584 Å) and Hydrogen (1216 Å) Interplanetary Emission Observations*, Astrophys. J., 222, 1068-1079 (1978)

Ajello, J.M., Thomas, G.E.: *Predicted Interplanetary Distribution of Lyman-α Intensity and Polarization*, Icarus, 61, 163-170 (1985)

Ajello, J.M, et al.: *Solar cycle study interplanetary Lyaman-Alpha variations: PIONEER VENUS orbiter sky background results*, Astrophys. J., 317, 964-986 (1987)

Akhmanov, S.A., Nikitin, S.Yu.: *Physical Optics*, Oxford University Press (1997)

Alexander, S.: *On the origin of the forms and the present condition of some of the clusters of stars, and several of the nebulae*, AJ, 2, 37, 97-103 (1852)

Alfven, H.: *Existence of Electromagnetic-Hydrodynamic Waves*, Nature, 3805, 405-406 (1942)

Ames Staff Research: *Equations, Tables and Charts for Compressible Flow*, Ames Aeronautical Laboratory, Report 1135 (1953)

Axford, W.I., Dessler, A.J., Gottlieb, B.: *Termination of solar wind and solar magnetic field*, ApJ, 137, 1268-1278 (1963)

Axford, W. I.: The interaction of the solar wind with the interstellar medium, in Solar Wind, ed. C. P. Sonett, P. J. Coleman, Jr., & J. M. Wilcox (NASA SP-308), 609-660 (1972)

Baranov, V.B., Krasnobaev, K.V., Kulikovsky, A.G.: *A Model of the Interaction of the Solar Wind with the Interstellar Medium*, Soviet Phys. Doklady, 15, 791 (1971)

Baranov, V.B., Krasnobaev, K.V., Ruderman, M.S.: *On the model of the solar wind-interstellar medium interaction with two shock waves*, Astrophys. Space Sci., 481-490 (1976)

Baranov, V.B., Lebedev, M.G., Ruderman, M.S.: *Structure of the region of solar wind-interstellar medium interaction and its influence on H atoms penetrating the solar wind*, Astrophys. Space Sci., 66, 441-451 (1979)

Baranov, V.B., Ermakov, V.B., Lebedev, M.G.: *A three-component model of solar wind-interstellar medium interaction: some numerical results*, Sov. Astron. Lett., 7, 206-208 (1981)

Baranov, V. B.: *On the problem of fluid dynamics foundation for application in the space physics*, Astrophysics and Space Science, 274, 3-16 (2000)

Baranov, V. B., Malama, Y. G.: *Model of the Solar Wind Interaction With the Local Interstellar Medium: Numerical Solution of Self-Consistent Problem*, J. Geophys. R., 98, 15157-15163 (1993)

Baranov, V.B.: *Early Concepts of the Heliospheric Interface: Plasma*, in *The Physics of the Heliospheric Boundaries*, V. Izmodenov and R. Kallenbach (eds.), ISSI Scientific Report No. 5, pp. 27-43, ESA-ESTEC (2006b)

Baranov, V.B.: *Kinetic-Hydrodynamic Models of the Solar Wind Interaction with the Partially Ionized Supersonic Flow of the Local Interstellar Gas: Predictions and Interpretations of the Experimental Data*, Space Sci. Rev., 142, 23-72 (2009)

Barth, C.A.: *Mariner 6 Measurements of the Lyman-Alpha Sky Background*, ApJ, 161, L181-L184 (1970)

Baum, S.A. et al.: *Hubble Space Telescope STIS spectroscopy of the Ly-α emission line in the central dominant galaxies in A426, A1795, and A2597: constraints on clouds in the intracluster medium*, Astrophys. J., 632, 122-136 (2005)

Beals, C.S.: *On the interpretation of interstellar lines*, MNRAS, 96, 661-678 (1936)

Belmont, G., Rezeau, L.: *Introduction la physique des plasmas*, CNRS-UVSQ-IPSL/CETP (2003)

Bétrémieux, Y., Corliss, J., Vincent, M.B., Vincent, F.E., Roesler, F.L., Harris, W.M.: *Description and ray-tracing simulations of HYPE, a far-ultraviolet polarimetric spatial-heterodyne spectrometer*, Proc. SPIE, 7732, 77322C-1 (2010)

Ben-Jaffel, L., Puyoo, O., Ratkiewicz, R.: *Far-ultraviolet echoes from the frontier between the solar wind and the local interstellar cloud*, Astrophys. J., 533, 924-930 (2000)

Ben-Jaffel, L., Harris, W., Bommier, V., Roesler, F., Ballester, G.E., Jossang, J.: *Predictions on the application of the Hanle effect to map the surface magnetic field of Jupiter*, Icarus, 178, 297-311 (2005)

Ben-Jaffel, L., Kim, Y.J., Clarke, J.: *The H Lyman- emission line from the upper atmosphere of Jupiter: Parametric radiative transfer study and comparison with data*, Icarus, 190, 504527 (2007)

Ben-Jaffel, L., Ballester, G., Clarke, J.T., Vincent, F.: *High Resolution Lyman-Mapping of the Jovian Upper Atmopshere and Corona*, DPS meeting # 42, # 11.13 (2010)

Berghöfer, T.W., Breitschwerdt, D.: *The origin of the young stellar population in the solar neighborhood - a link to the formation of the Local Bubble?*, A& A, 390, 299-306 (2002)

Bertaux, J.L., Blamont, J.E.: *Evidence for a Source of an Extraterrestrial Hydrogen Lyman-Alpha Emission: the Interstellar Wind*, Astron. Astrophys., 11, 200-217 (1971)

Bertaux, J.L., et al.: Interstellar Medium in the Vicinity of the Sun: A Temperature Measurement Obtained with Mars-7 Interplanetary Prove, Astron. Astrophys., 46, 19-29, 1976

Bertaux, J.L., et al.: *Characteristics of the Local Interstellar Hydrogen determined from PROGNOZ 5 and 6 interplanetary Lyman α line profile measurements with a hydrogen absorption cell*, Astron. Astrophys., 150, 1-20 (1985)

Bertaux, J.L., et al.: *SWAN: a study of solar wind anisotropies on SOHO with Lyman Alpha sky mapping*, Sol. Phys., 162, 403-439 (1995)

Bertin, P., et al.: *Detection of the Local Interstellar Cloud From High-Resolution Spectroscopy of Nearby Stars: Inferences on the Heliospheric Interface*, J. Geophys. R., 98, 15193-15197 (1993)

Bétrémieux, Y., Corliss, J., Vincent, M.B. et al.: *Description and ray-tracing simulations of HYPE, a far-ultraviolet polarimetric spatial-heterodyne spectrometer*, SPIE Proc., 7732, 77322C-77322C-12 (2010)

Bevington, P.R., Robinson, D.K.: *Data Reduction and Error Analysis*, McGraw-Hill, 3rd edition (2003)

Biermann, L.: *Solar corpuscular radiation and the interplanetary gas*, Observatory, 77, 109-110 (1957)

Billings, D.E.: *Distribution of matter with temperature in the emission corona*, ApJ, 130, 961-971 (1959)

Blackwell, D.E.: *A study of the outer corona from a high altitude aircraft at the eclipse of 1954 June 30. II. Electron densities in the outer corona and zodiacal light regions*, MNRAS, 116, 56-68 (1956)

Blamont, J.E., Cazes, S., Emerich, C.: *Direct Measurements of Hydrogen Density at Exobase Level and Exospheric Temperatures From Lyman α Line Shape and Polarization 1. Physical Background and First Results on Day Side*, J. Geophys. Res., 80, 2247-2265 (1975)

Blum, P.W., Fahr, H.J.: *Solar Wind Tail and the Anisotropic Production of Fast Hydrogen Atoms*, Nature, 223, 936-937 (1969)

Blum, P.W., Fahr, H.J.: *Interaction between Interstellar Hydrogen and the Solar Wind*, A& A, 4, 280-290 (1970)

Bostroem, A.: private communication (2011)

Bottlinger, K.F., Schneller, H.: *Uber die interstellare Absorption innerhalb der Milchstrasse*, Z. Astrophys., 1, 339 (1930)

Bowyer, C.S., Field, G.B., Mack, J.E.: *Detection of an Anisotropic Soft X-ray Background Flux*, Nature, 217, 3 (1968)

Brandt, J.C., Chamberlain, J.W.: *Interplanetary Gas. I. Hydrogen Radiation in the Night Sky*, Astrophys. J., 130, 670-682 (1959)

Brandt, J.C., et al.: *The Goddard High Resolution Spectrograph: Instrument, Goals, and Science Results*, PASP, 106, 890-908 (1994)

Bregman, J.N.: *The Galactic Fountain of High-Velocity Clouds*, ApJ, 236, 577 (1980)

Breitschwerdt, D., Schmutzler, T.: *Delayed recombination as a major source of the soft X-ray background*, Nature, 371, 774-777 (1994)

Breitschwerdt, B.: *The Local Bubble and Beyond*, Lecture Notes in Physics, Springer (1998)

Breitschwerdt, D., Freyberg, M.J., Egger, R.: *Origin of H I clouds in the Local Bubble. I. A hydromagnetic Raileygh-Taylor instability caused by the interaction between the Loop I and the Local Bubble*, Astronom. Astrophys., 361, 303-320 (2000)

Breitschwerdt, D.: *Blown away by cosmic rays*, Nature, 452, 826-827 (2008)

Bzowski, M., Fahr, H.J., Rucinski, D. , Scherer, H.: *Variation of bulk velocity and temperature anisotropy of neutral heliospheric hydrogen during the solar cycle*, Astron. Astrophys., 326, 396-411 (1997)

Castor, J., McCray, R., Weaver, R.: *Interstellar Bubbles*, ApJ, 200, L107 (1975)

Cazes, S., Emerich, C.: *Interstellar Medium Ly α Emission: Line Profile, Temperature and Polarization Measurements Deduced from Its Geocoronal Absorption*, Astron. Astrophys., 59, 59-69 (1977)

Chakrabarti, S., Cotton, M.C., Vickers, J.S., Bush, B.C.: *Self-compensating, all-reflection interferometer*, Ap. Opt., 33, 2596-2607 (1994)

Chambers, W.H., Felhau, P.E., Fuller, J.C., Kunz, W.E.: *Anisotropic Atomic Hydrogen Distribution in Interplanetary Space*, Nature, 225, 713-714 (1970)

Chandezon, J., Maystre, D., Raoult, G.: *A new theoretical method for diffraction gratings and its numerical application*, J. Opt., 11, 235-241 (1980)

Chandrasekhar, S., Fermi, E.: *Magnetic Fields in Spiral Arms*, ApJ, 118, 113-115 (1953)

Chapman, S., Cowling, T.G.: *The Mathematical Theory of Non-Uniform Gases*, Cambridge University Press (1953)

Clarke, J.T., Bowyer, S., Fahr, H.J., Lay, G.: *IUE high resolution spectrophotometry of H Ly α emission from the local interstellar medium*, Astron. Astrophys., 139, 389-393 (1984)

Clarke, J.T., et al.: *HST/GHRS observations of the interplanetary medium downwind and in the inner solar system*, ApJ, 448, 893-904 (1995)

Clarke, J.T., et al.: *HST/GHRS observations of the velocity structure of interplanetary hydrogen*, Astrophys. J., 499, 482-488 (1998)

Clarke, J.T.: private communication (2010)

Connes, P.: *Spectromètre interférentiel à selection par l'amplitude de modulation*, J. Phys. Radium, 19, 215-222 (1958)

Cox, D.P., Smith, B.W.: *Large-Scale Effects of Supernova Remnants on the Galaxy: Generation and Maintenance of a Hot Network of Tunnels*, ApJ, 189, L105 (1974)

Cox, D.P., Snowden, S.L.: *Perspective on the Local Interstellar Medium*, Adv. Space Res., 6, 97-107 (1986)

Cox, D.P., Reynolds, R.J.: *The Local Interstellar Medium*, Ann. Rev. Astron. Astrophys., 25, 303-344 (1987)

Cravens, T.E.: *Heliospheric X-Ray emission associated with charge transfer of the solar wind with interstellar neutrals*, Astrophys. J., 532, L153-L156 (2000)

Damiani, C., Drossart, P., Sémery, A., Réess, J.M., Maillard, J.P.: *An Imaging Heterodyne Transform Spectrometer for Planetary Exploration*, Proceedings of International Conference on Space Optics, Toulouse, France (2008)

Danby, J.M.A., Camm, G.L.: *Statistical dynamics and accretion*, M.N.R.A.S., 117, 50-71 (1957)

Davis, L. Jr.: *Interplanetary Magnetic Fields and Cosmic Rays*, Phys. Rev., 100, 1440-1444 (1955)

Dawson, O.R., Harris, W.M.: *Tunable, all-reflective spatial heterodyne spectrometer for broadband spectral line studies in the visible and near-ultraviolet*, Applied Optics, 48, 4227-4238 (2009)

Dessler, A.J.: *Solar Wind and Interplanetary Magnetic Field*, Rev. Geophys., 5, 1-41 (1967)

Dickey, J.M., Lockman, F.J.: *H I in the Galaxy*, Annu. Rev. Astron. Astrophys., 28, 215-261 (1990)

Dimeo, R. et al.: *PAN: Peak Analysis. A general-purpose curve fitting utility with a graphical user interface*, http://www.ncnr.nist.gov/staff/dimeo/panweb/pan.html (2005)

Dohi, T., Suzuki, T.: *Attainment of High Resolution Holographic Fourier Transform Spectroscopy*, Applied Optics, 10, 1137-1140 (1971)

Eddington, A.S.: *Diffuse Matter in Interstellar Space*, P. R. Soc. A, 111, 759, 424-456 (1926)

Emerich, C., Cazes, S., Blamont, J.E.: *Exobase Hydrogen Density Temperature From Ly α Absorption and Polarization Measurements 2. Dayside and Nightside Results During April 1971*, J. Geophys. Res., 81, 6103-6114 (1976)

Englert, C.R., Babcock, D.D., Harlander, J.M.: *Spatial heterodyne spectroscopy for long-wave infrared: first measurements of broadband spectra*, Optical Engineering, 48, 105602 (2009)

Everett, J.E., Zweibel, E.G., Benjamin, R.A., McCammon, D., Rocks, L., Gallagher III, J.S.: *The Milky Way's kiloparsec-scale wind: a hybrid cosmic-ray and thermally driven outflow*, Astrophys. J., 674, 258-270 (2008)

Fahr, H.J.: *Interstellar Hydrogen Subject to a Net Repulsive Solar Force Field*, Astron. Astrophys., 77, 101-109 (1979)

Fahr, H.J., Ratkiewicz-Landowska, R., Grzedzielski, S.:*The heliopause as a pressure equilibrium surface separating two counterflowing magnetized plasmas*, Adv. Space Res., 6, 389-392 (1986)

Fahr, H.J., Grzedzielski, S., Ratkiewicz-Landowska, R.:*Magnetohydrodynamic modeling of the 3-dimensional heliopause using the Newtonian approximation*, An. Geophys., 6, 337-354 (1988)

Fahr, H.J., Rucinski, D., Judge, D.L.: *Time- and space-variable structures of interstellar gas passing over the heliosphere: consequences for the interplanetary UV resonance glow*, Astron. Astrophys., 268, 792-804 (1993)

Fahr, H.J.: *Global structure of the heliosphere and interaction with the local interstellar medium: three decades of growing knowledge* Adv. Space Res., 34, 3 (2004)

Fano, J.: *The Theory of Anomalous Diffraction Gratings and of Quasi-Stationary Waves on Metallic Surfaces (Sommerfeld's Waves)*, J. Opt. Soc. Am., 42, 213-222 (1941)

Fermi, E.: *On the Origin of the Cosmic Radiation*, Physical Review, 8, 1169-1174 (1949)

Field, G.B., Goldsmith, D.W., Habbing, H.J.: *Cosmic-ray heating of the interstellar gas*, ApJ, 155, L149-L154 (1969)

Frisch, P.C.: *Is the Sun embedded in a Typical Interstellar Cloud? Connecting Interstellar Gas in and out of the Heliospere*, Space Sci. Rev., 143, 191-204 (2009)

Frisch, P.C. et al.: *The Galactic Environment of the Interstellar Material Inside and Outside of the Heliosphere*, Space Sc. Rev., 146, 235-273 (2009)

Hall, D.T., Shemansky, D.E., Judge, D.L., Gangopadhyay, P., Gruntman, M.A.: *Heliospheric Hydrogen Beyond 15 AU: Evidence for a Termination Shock*, JGR, 98, 15185-15192 (1993)

Hall, D.T.: *Ultraviolet resonance radiation and the structure of the heliosphere*, Ph.D. thesis, University of Arizona (1992)

Harlander, J.: *Spatial heterodyne spectroscopy: interferometric performance at any wavelength without scanning*, Ph.D. dissertation (University of Wisconsin, Madison, 1991)

Harlander, J., Reynolds, R.J., Roesler, F.L.: *Spatial heterodyne spectroscopy for the exploration of diffuse interstellar emission lines at far-ultraviolet wavelengths*, Astrophys. J., 396, 730-740 (1992)

Harlander, J., Roesler, F.L., Cardon, J.G., Englert, C.R., Conway, R.R.: *SHIMMER: a spatial heterodyne spectrometer for remote sensing of Earths middle atmosphere*, Applied Optics, 41, 1343-1352 (2002)

Harlander, J., Roesler, F.L., Englert, C.R., Cardon, J.G., Conway, R.R., Brown, C.M., Wimperis, J.: *Robust monolithic ultraviolet interferometer for the SHIMMER instrument on STPSat-1*, Applied Optics, 42, 2829-2834 (2003)

Harris, W.M., Roesler, F.L., Harlander, J., Ben-Jaffel, L., Mierkiewicz, E., Corliss, J., Oliversen, R.J.: *Applications of reflective spatial heterodyne spectroscopy to UV exploration in the Solar System*, Proc. SPIE, 5488, 886-897 (2004)

Harris, W., Roesler, F., Ben-Jaffel, L. et al., HYPE: *A Sub-Orbital Spatial Heterodyne Spectro-Polarimeter for Study of Ly-α Sources in the Solar System*, OSA Proc., paper FWC5 (2009)

Hartmann, J.: *Investigations on the spectrum and orbit of δ Orionis*, ApJ, 19, 268-286 (1904)

Hass, G., Tousey, R.: *Reflecting Coatings for the Extreme Ultraviolet*, J. Opt. Soc. Am., 49, 593-602 (1959)

Heerikhuisen, J., et al.: Pick-up ions in the outer heliosheath: a possible mechanism for the Interstellar Boundary EXplorer ribbon, Astrophys. J. Lett., 708, 126-130 (2010)

Heiles, C.: *Is the Intercloud Medium Pervasive ?*, ApJ, 235, 833 (1980)

Herschel, W.: *On the Proper Motion of the Sun and Solar SystemSystem; With an Account of Several Changes That Have Happened among the Fixed Stars since the Time of Mr. Flamstead*, Philos. T. R. Soc. Lond., 73, 247-283 (1783)

Holzer, T.E. : *Neutral Hydrogen in Interplanetary Space*, Rev. Geophys., 15, 4, 467-490 (1977)

Hosseini, S.S., Gong, A., Ruth, D., Baldis, H.A., Harris, W.M.: *Tunable spatial heterodyne spectroscopy(TSHS): a new technique for broadband visible interferometry*, Proc. SPIE, 7734, 77343J (2010)

Hubble, E.: *NGC 6822, a remote stellar system*, ApJ, 62, 409-433 (1925)

Hummer, D.G.: *Non-coherent Scattering I. The Redistribution Functions with Doppler Broadening*, MNRAS, 125, 21-37 (1962)

Hunter, W.R., Osantowski, J.F., Hass. G.: *Reflectance of Aluminum Overcoated with MgF, and LiF in the Wavelength, Region from 1600 Å to 300 Å at Various Angles of Incidence* Appl. Opt., 10, 510-544 (1971)

Hutcheson, E.T., Hass, G., Cox, J.T.: *Effect of Deposition Rate and Substrate Temperature on the Vacuum Ultraviolet Reflectance of MgF2- and LiF-Overcoated Aluminum Mirrors*, Appl. Opt., 11, 2245-2248 (1972)

Ignace, R., Cassinelli, J.P., Nordsieck, K.H.: *The Hanle effect as a diagnostic of magnetic fields in stellar envelopes. II. Some theoretical results for resolved line profiles*, Astrophys. J., 520, 335-346 (1999)

Ivanov, V.V.: *Transfer of radiation in spectral lines*, N.B.S. special publication 385 (1973)

Izmodenov, V.V.: *The Heliospheric Interface: Models and Observations*, in *The Sun and the Heliosphere as an Integrated System*, Poletto, G., Suess, S.T., ASSL (2004)

Izmodenov, V.V., Malama, Y.: *Variations of interstellar H atom parameters in the outer heliosphere: solar cycle effects*, Adv. Space Res., 34, 74-78 (2004)

Izmodenov, V., Malama, Y., Ruderman, M.S.: *Solar cycle influence on the interaction of the solar wind with Local Interstellar Cloud*, Astron. Astrophys., 429, 1068-1080 (2005a)

Izmodenov, V., Alexashov, D., Myasnikov, A.: *Direction of the interstellar H atom flow in the heliosphere: Role of the interstellar magnetic field*, Astron. Astrophys., 437, L35-L38 (2005b)

Izmodenov, V., Malama, Y.G., Ruderman, M.S.: *Modeling of the outer heliosphere with the realistic solar cycle*, Adv. Space Res., 41, 318-324 (2008)

Jenkins, E.B., Meloy, D.A.: *A Survey with Copernicus of Interstellar O VI Absorption*, ApJ, 193, L12 (1974)

Kivelson, M.G., Russell, C.T.: *Introduction to Space Physics*, Cambridge University Press (1995)

Krasnopolsky, V.A., Mumma, M.J., Gladstone, G.R.: *Detection of Atomic Deuterium in the Upper Atmosphere of Mars*, Science, 280, 1576-1580 (1998)

Kupperian, J.E., Byram, E.T.,Chubb, T.A., Friedman, H.: *Far Ultraviolet Radiation in the Night Sky*, Planet. Space Sci., 1, 3-6 (1959)

Kurt, V.G., Syunyaev, R.A.: *Observations and Interpretation of the Ultraviolet Radiation of the Galaxy*, Soviet Physics, 11, 928-931 (1967)

Kurt, V.G., Dostovalov, S.B.: *Far Ultraviolet Radiation from the Milky Way*, Nature, 218, 258 (1968)

Kurt, V.G., Mironova, E.N., Fadeev, E.N.: *Ultraviolet Studies of the Interplanetary and Local Interstellar Medium*, Cos. Res., 47, 1-13 (2009)

Lallement, R., Bertaux, J.L., Dalaudier, F.: *Interplanetary Lyman α spectral profiles and intensities for both repulsive and attractive solar force fields: predicted absorption pattern by a hydrogen cell*, Astron. Astrophys.,150, 21-32 (1985)

Lallement, R., Bertin, P.: *Northern-hemisphere observations of nearby interstellar gas: Possible detection of the local cloud*, Astron. Astrophys. 266, 479-485 (1992)

Lallement, R., Quémerais, E., Bertaux, J.L., Ferron, S., Koutroumpa, D., Pellinen, R.: *Deflection of the Interstellar Neutral Hydrogen Flow Across the Heliospheric Interface*, Science, 307, 1447-1449 (2005)

Lallement, R., Quémerais, E., Koutroumpa, D., Bertaux, J.L., Ferron, S., Schmidt, W., Lamy, P.: *The Interstellar H Flow: Updated Analysis of SOHO/SWAN Data*, AIP Conf. Proc., 1216, 555-558 (2010)

Linsky, J.L., Wood, B.E.: *The α Centauri line of sight: D/H ratio, physical properties of local interstellar gas, and measurement of heated hydrogen (the"Hydrogen Wall") near the heliopause*, Astrophys. J., 463, 254-270 (1996)

Linsky, J.L.: *Understanding physical processes in the diffuse ISM using high-resolution spectroscopy*, Astrophys Space Sci, DOI 10.1007/s10509-011-0657-2

Loewen, E.G., Nevière, M.: *Dielectric coated gratings: a curious property*, Appl. Opt., 16, 3009-3011 (1977)

Loewen, E.G., Nevière, M.: *Simple selection rules for VUV and XUV diffraction gratings*, Appl. Opt., 17, 1087-1092 (1978)

Loewen, E.G., Popov, E.: *Diffraction Gratings and Applications*, Marcel Dekker (1997)

Maíz-Apellániz, J.: *The Origin of the Local Bubble*, ApJ, 560, L83-L86 (2001)

Mange, P., Meier, P.P.: *OGO 3 Observations of the Lyman Alpha intensity and the Hydrogen Concentration beyond 5 R_E*, JGR, 75, 1837-1847 (1970)

Markwardt, C. B.: *Non-linear Least Squares Fitting in IDL with MPFIT*, ASP Conference Series, 411, 251-254 (2008)

Marquardt, D.W.: *An Algorithm for Least-Squares Estimation of Non-Linear Parameters*, J. Soc. Indust. Appl. Math., II, 431-441 (1963)

Marsch, E.: *Solar Wind*, in: *Space Solar Physics*, Lecture Notes in Physics, Vial, J-C, Bocchialini, K. Boumier, P. (1997)

Mashev, L.B., Popov, E.K., Loewen, E.G.: *Asymmetrical trapezoidal grating efficiency*, Appl. Opt., 26, 2864-2866 (1987)

Maystre, D.: *Rigorous Vector Theories of Diffraction Gratings*, Progress in Optics, XXI, 3-67 (1984)

McCandliss, S.R., Burgh, E.B., Feldman, P.D.: *Ultraviolet groove efficiency of a holographic grating: implications for a dual-order spectrograph*, Appl. Opt. 40, 2626-2631 (2001)

McComas, D.J. et al.: *Global Observations of the Interstellar Interaction from the Interstellar Boundary Explorer (IBEX)*, Science, 326, 959-962 (2009)

McKee, C.F., Ostriker, J.P.: *A Theory of the Interstellar Medium: Three Components Regulated by Supernova Explosions in an Inhomogeneous Substrate*, ApJ, 218, 148 (1977)

McLean, I.S.: *Electronic Imaging in Astronomy*, Springer-Praxis, 2nd edition (2008)

McPhedran, R.C.: *Anomalous physics pulled apart*, Nat. Phys., 2, 225-226 (2006)

Meyer-Vernet, N.: *How does the solar wind blow? A simple kinetic model*, Eur. J. Phys., 20, 167-176 (1999)

Mihalas, D.: *Stellar atmospheres*, W.H. Freeman and Company (1978)

Moebius, E. et al.: *Coordinated observation of local interstellar helium in the Heliosphere*, Astron. Astrophys., 426, 897-907 (2004)

Morton, D.C., Purcell, J.D.: *Observations of the Extreme Ultraviolet Radiation in the Night Sky Using an Atomic Hydrogen Filter*, Planet. Space Sc., 9, 455-458 (1962)

Norman, C.A., Ikeuchi, S.: *The Disk-Halo Interaction: Superbubles and the Structure of the Interstellar Medium*, ApJ, 345, 372 (1989)

Neugebauer, M., Snyder, *Solar Plasma Experiment, Science*, 138, 1095-1097 (1962)

Nevière, M., Maystre, D., Vincent, P.: *Determination of the leaky modes of a corrugated waveguide: application to the study of anomalies of dielectric coated gratings*, J. Opt. Paris, 8, 231-242 (1977)

Nordsieck, K.H., Harris, W.M.: *Ultraviolet astronomical polarimetry: some results and prospects*, Proc. SPIE, 3764, 124-133 (1999)

Nordsieck, K.H., Jaehnig, K.P., Burgh, E.B., Kobulnicky, H.A., Percival, J.W., Smith, M.P.: *Instrumentation for high-resolution spectropolarimetry in the visible and far-ultraviolet*, Proc. SPIE, 4843, 170-179 (2003)

Opher, M., Richardson, J.D., Toth, G., Gombosi, T.I: *Confronting Observations and Modeling: The Role of the Interstellar Magnetic Field in Voyager 1 and 2 Asymmetries*, SSR, 143, 4355 (2009)

Opher, M., Drake, J.F., Swisdak, M., Schoeffler, K.M., Richardson, J.D., Decker, R.B., Toth, G.: *Is the Magnetic Field in the Heliosheath Laminar or a Turbulent Sea of Bubbles*, ApJ , 734, 71 (2011)

Osterbart, R., Fahr, H.J.: *A Boltzmann-kinetic approach to describe the entrance of neutral interstellar hydrogen into the heliosphere*, Astron. Astrophys., 264, 260-269 (1992)

Palmer, C.H.: *Parallel Diffraction Grating Anomalies*, J. Opt. Soc. Am., 42, 269-276 (1952)

Parker, E.N.: *Dynamics of the interplanetary gas and magnetic fields*, ApJ, 128, 644-676 (1958)

Parker, E.N.: *The Stellar-Wind Regions*, ApJ, 134, 20-27 (1961)

Parker, E.N.: *Interplanetary Dynamical Processes*, Interscience Publishers (1963)

Patterson, T.N.L., Johnson, F.S., Hanson, W.B.:*The distribution of interplanetary hydrogen*, Planet. Space Sci., 11, 767-778 (1963)

Petit, R.: *Electromagnetic grating theories: Limitations and successes*, Nouv. Rev. Optique, 6, 129-135 (1975)

Petit, R.: *Electromagnetic Theory of Gratings*, Springler-Verlag (1980)

Pikel'Ner, S.B.: *Ionization and Heating of Interstellar Gas by Suprathermal Particles*, ApL, 1, 43 (1967)

Plaskett, J.S.: *The H and K Lines of Calcium in O-type stars*, MNRAS, 84, 80-93 (1923)

Plaskett, J.S., Pearce, J.A., *The Motion and Distribution of Interstellar Matter*, MNRAS, 90, 243-268 (1930)

Pogorelov, N.V., et al.: *Heliospheric asymmetries due to the action of the interstellar magnetic field*, Adv. Space Res., 44, 1337-1344 (2009)

Pogorelov, N.V., et al.: *Heliospheric asymmetries and 2-3 kHz radio emission under strong interstellar magnetic field conditions*, Astrophys. J., 695, L31-L34 (2009)

Pogorelov, N.V., et al.: *Modeling Heliospheric Phenomena with the Multi-scale Fluid-Kinetic Simulation Suite*, ASPC, 429, 266-273 (2010)

Popov, E., Bonod, N., Enoch, S.: *Comparison of plasmon surface waves on shallow and deep metallic 1D and 2D gratings*, 15, 4224-4237 (2007)

Popov, E., private communication (2011)

Proffitt, C., et al.: *STIS Instrument Handbook*, Version 9.0, Baltimore: STScI (2010)

Pryor, W., Ajello, J., McComas, D.J., Witte, M., Tobiska, W.K.: *Hydrogen atom lifetimes in the three-dimensional heliosphere over the solar cycle*, JGR, 108, 8034 (2003)

Pryor, W., et al.: *Radiation transport of heliospheric Lyman-α from combined Cassini and Voyager data sets*, A & A, 491, 21-28 (2008)

Puyoo, O., Ben-Jaffel, L., Emerich, C.: *The Neutral Hydrogen Abundance and Ionization in the Inner Heliosphere*, Astrophys. J., 480, 262-271 (1997)

Puyoo, O., Ben-Jaffel, L.: *The Intrinsic Properties of the Local Interstellar Medium*, Proceeding of the IAU Colloquium No.166 (1997)

Puyoo, O.: *H and He in the Solar System*, Ph.D. Thesis, Université Pierre et Marie Curie (1998)

Quémerais, E., Sandel, B.R., Lallement, R., Bertaux, J.L.: *A new source of Ly-α emission detected by Voyager UVS: heliospheric or galactic origin?*, Astron. Astrophys., 299, 249-257 (1995)

Quémerais, E., Malama, Y.G., Sandel, B.R., Lallement, R., Bertaux, J.-L., Baranov, V.B.: *Outer heliosphere Lyman α background derived from two-shock model hydrogen distributions: application to the Voyager UVS data*, Astron. Astrophys., 308, 279-289 (1996a)

Quémerais, E., Sandel, B.R., De Toma, G.: *26 day modulation of the sky background Lyα brightness: estimating the interplanetary hydrogen density*, Astrophys. J., 463, 349-358 (1996b)

Quémerais, E. et al.: *Interplanetary Lyman α line profiles derived from SWAN/SOHO hydrogen cell measurements: Full-Sky Velocity Field*, J. Geophys. R., 104, 12585-12603 (1999)

Quémerais, E.: *Angle dependent partial frequency redistribution in the interplanetary medium at Lyman α*, Astron. Astrophys., 358, 353-367 (2000)

Quémerais, E., Izmodenov, V.: *Effects of the heliospheric interface on the interplanetary Lyman α glow seen at 1 AU from the Sun*, Astron. Astrophys., 396, 269-281 (2002)

Quémerais, E., Bertaux, J.-L., Lallement, R., Sandel, B.R., Izmodenov, V.: *Voyager 1/UVS Lyman α glow data from 1993 to 2003: Hydrogen distribution in the upwind outer heliosphere*, J. Geophys. Res., 108, 8029 (2003)

Quémerais, E., et al.: *Interplanetary Lyman α line profiles: variations with solar activity cycle*, Astron. Astrophys., 455, 1135-1142 (2006)

Quémerais, E.: *The Interplanetary Lyman-α background*, in *The Physics of the Heliospheric Boundaries*, V. Izmodenov and R. Kallenbach (eds.), ISSI Scientific Report No. 5, pp. 283 - 310, ESA-ESTEC, Paris (2006)

Quémerais, E., et al.: *Time dependent model of the interplanetary Lyman α glow: applications to the SWAN data*, Astron. Astrophys., 488, 351-359 (2008)

Quémerais, E., Lallement, R., Bertaux, J.L., Sandel, B.R., Izmodenov, V., Malama, Y.: *Ultraviolet glow from the hydrogen wall*, Astrophys. J., 711, 1257-1262 (2010)

Ratkiewicz, R., Barnes, A., Molvik, G.A., Spreiter, J.R., Stahara, S.S., Vinokur, M., Venkateswaran, S.: *Effects of varying strength and orientation of local interstellar magnetic field on configuration of exterior heliosphere: 3D MHD simulations*, Astron. Astrophys., 335, 363-369 (1998)

Ratkiewicz, R., Ben-Jaffel, L.: *Effects of interstellar magnetic field B and constant flux of neutral H on the heliosphere*, J. Geophys. R., 107, 1007 (2002)

Ratkiewicz, R., Ben-Jaffel, L., Grygorczuk, J.: *What do we know about the orientation of the local interstellar magnetic field ?*, ASPC, 385, 189-194 (2007)

Ratkiewicz, R., Grygorczuk, J.: *Orientation of the local interstellar magnetic field inferred from Voyagers' positions*, GRL, 35, L23105 (2008)

Rayleigh, Lord: *On the Dynamical Theory of Gratings*, Proc. Phys. Soc. London, 79, 399-417 (1907)

Rebull, L., et al.: *Limits on the boron isotopic ratio in HD 76932*, Astrophys. J., 507, 387-397 (1998)

Ripken, H.W., Fahr, H.J.: *Modification of the local interstellar gas properties in the heliospheric interface*, Astron. Astrophys. 122, 181-192 (1983)

Roesler, F.L., et al.: *Spatial Heterodyne Spectroscopy: An Emerging Technology for Interference Spectroscopy*, ASP Conf. Series, 291, 395-398 (2003)

Rosse, E.: *Observations on the Nebulae*, Philos. T. R. Soc. Lond.,140, 499-514 (1850)

Ruciński, D., Bzowski, M.: *Modulation of interplanetary hydrogen density distribution during the solar cycle*, Astron. Astrophys., 296, 248-263 (1995)

Russell, C.T.: *Solar Wind and Interplanetary Field: A tutorial*, AGU, Geophysical monograph 125 (2001)

Rybicki, G.B., Lightman, A.P.: *Radiative Processes in Astrophysics*, Wisley-Interscience (1979)

Sanders, W.T., Kraushaar, W.L., Nousek, J.A., Fried, P.M.: *Soft Diffuse X-Rays in the Southern Galactic Hemisphere*, ApJ, 217, L87 (1977)

Scherer, H., Fahr, H.J.: *H Lyman alpha transport in the heliosphere based on an expansion into scattering hierarchies*, Astron. Astrophys., 309, 957-969 (1996)

Scherer, H., Fahr, H.J., Clarke, J.T.: *Refined analysis of interplanetary H-Lyα spectra obtained with the Hubble-Space Telescope GHRS spectrometer*, Astron. Astrophys., 325, 745-754 (1997)

Scherer, H., Bzowski, Fahr H.J., M., Ruciński, D.: *Improved analysis of interplanetary HST-$H_{Ly\alpha}$ spectra using timedependent modelings*, Astron. Astrophys., 342, 601-609 (1999)

Schroeder, D.J.: *Astronomical Optics*, Academic Press, 2nd edition (2000)

Scott, J.S., Jensen, E.B., & Roberts, W.W. Jr.: *The missing intercloud medium and spiral galaxies*, Nature, 265, 123 (1977)

Shapiro, P.R., Field, G.B.: *Consequences of a New Hot Component of the Interstellar Medium*, ApJ, 205, 762 (1976)

Shemansky, D.E., Judge, D.L., Jessen, J.M.: *Pioneer 10 and Voyager observations of the interstellar medium in scattered emission of the He 584 Å and H Lyα 1216 Å lines*, NASCP, 2345, 24-27 (1984)

Shu, F.H.: *Hot Gas in the Galaxy: How Extensive is it ?*, IAUS, 77, 139 (1978)

Siegmund, O.R.H. et al.: *High-resolution cross delay line detectors for the GALEX mission*, SPIE proc., 3765, 429-440 (1999)

Snowden, D.P. and 8 co-authors: *First Maps of the Soft X-Ray Diffuse Background from the ROSAT XRT/PSPC All-Sky Survey*, Astrophys. J., 454, 643-653 (1995)

Spitzer, L. Jr.: *Behavior of matter in space*, Astrophys. J., 120, 1-18 (1954)

Spitzer, L. Jr.: *Physics of fully ionized gas*, Dover Publications, second revised edition (1956)

Spitzer, L. Jr.: *Diffuse Matter in Space*, Interscience Publishers (1968)

Stenflo, J.O., Biverot, H., Stenmark, L.: *Ultraviolet polarimeter to record resonance-line polarization in the solar spectrum around 130-150 nm*, Applied Optics, 15, 1188-1198 (1976)

Stenflo, J.O., Cravins, D., Wihlborg, N., Bruns, A., Prokof'ev, V.K., Zhitnik, I.A., Biverot, H., Stenmark, L.: *Search for spectral line polarization in the solar vacuum ultraviolet*, Solar Physics, 66, 13-19 (1980)

Stenflo, J.O.: *Stokes polarimetry of the Zeeman and Hanle effects*, ISSI Scientific Reports Series, 9, 543-557 (2010)

Stephan, S.G., Chakrabarti, S., Vickers, J., Cook, T., Cotton, D.: *Interplanetary H Lyα observations from a sounding rocket*, Astrophys. J., 559, 491-500 (2001)

Stone, E.C., Cummings, A.C., McDonald, F.B., Heikkila, B.C., Lal, N., Webber, W.R.: *Voyager 1 Explores the Termination Shock Region and the Heliosheath Beyond*, Science, 309, 2017-2020 (2005)

Stone, E.C., Cummings, A.C., McDonald, F.B., Heikkila, B.C., Lal, N., Webber, W.R.: *An asymmetric solar wind termination shock*, 454, 71-74 (2008)

Strömgren, B.: *The Physical State of Interstellar Hydrogen*, ApJ, 89, 526 (1939)

Struve, O.: *Further work on interstellar calcium*, ApJ, 67, 353-390 (1928)

Struve, F.G.W.: *Etudes d'astronomie stellaire*, Académie Impériale des Sciences, St. Petersburg (1847)

Sturrock, P.A.: *Plasma Physics*, Cambridge University Press (1994)

Teng, Y.Y., Stern, E.A.: *Plasma radiation from metal grating surfaces*, Phys. Rev. Lett., 9, 511-514 (1967)

Thomas, G.E., Krassa, R.F.: *OGO 5 Measurements of the Lyman Alpha Sky Background*, Astron. Astrophys., 11, 218-233 (1971)

Thomas, G.E.: *The interstellar wind and its influence on the interplanetary environment*, Ann. Rev. Earth Planet. Sci., 6, 173-204 (1978)

Thorndike, S.L.: *Interstellar Matter*, PASP, 42, 99-104 (1930)

Trumpler, R.J.: *Preliminary Results on the Distances, Dimensions and Space Distribution of Open Stars Clusters*, Lick Obs. Bull., 14, 154 (1930)

van de Kamp, P.: *On The Absorption of Light in the Galactic System*, Astronom. J., 42, 97 (1932)

Vincent, F.E., Ben-Jaffel, L., Harris, W.M.: *Exploration of variability in the line shape and Doppler shift of scattered solar Lyman-α radiation from interplanetary hydrogen*, American Geophysical Union, Fall Meeting 2009, abstract # SH21A-1494 (2009)

Vincent, F.E., Ben-Jaffel, L., Harris, W.M.: *Updated analysis of the upwind interplanetary hydrogen velocity as observed by the Hubble Space Telescope during solar cycle 23*, Astrophys. J., 738, 135 (2011a)

Vincent, F.E., Harris, W.M., Beasley, M., Corliss, J., Bétrémieux, Y., Ben-Jaffel, L., Roesler, F.L.: *Identification and treatment of an efficiency anomaly in a symmetrically ruled grating illuminated at normal incidence*, J. Electron. Spectrosc., doi:10.1016/j.elspec.2010.12.033 (2011b)

Wallis, M.: *Local interstellar medium*, Nature, 254, 202-203 (1975)

Walsh, J.R., Goudfrooij, P., Malamuth, E.: *STIS Geometric Distortion - SMOV3A tests for CCD, NUV-MAMA and FUV-MAMA*, Instrument Science Report STIS 2001-02 (2001)

Watchorn, S., Roesler, F.L., Harlander, J., Jaehnig, K.P., Reynolds, R.J., Sanders, W.T.: *Development of the Spatial Heterodyne Spectrometer for VUV remote sensing of the interstellar medium*, Proc. SPIE, 4498, 284-295 (2001)

Weaver, R., McCray, R., Castor, J., Shapiro, P., Moore, R.: *Interstellar Bubbles. II. Structure and Evolution* ApJ, 218, 377 (1977)

Welsh, B.Y., Shelton, R.L.: *The trouble with the Local Bubble*, Astrophys. Space Sci., 323, 1-16 (2009)

Welsh, B.Y., Lallement, R., Vergely, J.-L., Raimond, S.: *New 3D gas density maps of NaI and CaII interstellar absorption within 300pc*, Astron. Astrophys., 510, 1-23 (2010)

Witte, M., Rosenbauer, H., Banaszkiewicz, M., Fahr, H.: *The Ulysses neutral gas experiment: determination of the velocity and temperature of the interstellar neutral helium*, Adv. Space Res., 13, (6)121-(6)130 (1993)

Witte, M.: *Review of results obtained during one solar cycle with the Ulysses/GAS-instrument*, Astron. Astrophys., 426, 835-844 (2004)

Wiza, J.L.: *Microchannel plate detectors*, Nuclear Instruments and Methods, 162, 587-601 (1979)

Wood, R.W.: *On a remarkable case of uneven distribution of light in a diffraction of light in a diffraction grating spectrum*, Proc. Phys. Soc. London, 18, 269-275 (1902)

Wood, O.R., Craighead, H.G., Sweeney, J.E., Maloney, P.J.: *Vacuum ultraviolet loss in magnesium fluoride films*, Appl. Opt., 23, 3644-3649 (1984)

Woodgate, B.E. and 14 co-authors: *The ultraviolet spectrometer and polarimeter on the solar maximum mission*, Solar Physics, 65, 73-90 (1980)

Woodgate, B.E. et al.: *The Space Telescope Imaging Spectrograph Design*, PASP, 110, 1183-1204 (1998)

Wu, F.M., Judge, D.L.: *Temperature and flow velocity of the interplanetary gases along solar radii*, Astrophys. J., 231, 594-605 (1979)

Wu, F.M., Judge, D.L.: *A reanalysis of the observed interplanetary hydrogen Lα emission profiles and the derived local interstellar gas temperature and velocity*, Astrophys. J., 239, 389-394 (1980)

York, D.G.: *Highly Ionized Atoms observed with Copernicus* ApJ, 193, L127 (1974)

Zank, G.P.: *Interaction of the Solar Wind with the Local Interstellar Medium: a Theoretical Perspective*, Space Science Reviews, 89, 413-688 (1999)